1992

Spectroscopy of tetravalent chromium in different hosts in search for new, tunable, broad band lasers in the 1.2 um band

Chiranjit Deka
University of Central Florida, cdeka@hotmail.com

SPECTROSCOPY OF TETRAVALENT CHROMIUM IN DIFFERENT HOSTS IN SEARCH FOR NEW, TUNABLE, BROAD BAND LASERS IN THE 1.2 μm BAND

BY

CHIRANJIT DEKA
B.Sc. Gauhati University, 1981
M.Sc. University of Windsor, 1989

DISSERTATION

Submitted in partial fulfillment of the requirements
for the degree of Doctor of Philosophy
in the Department of Physics
in the graduate studies program
of the College of Arts and Sciences
University of Central Florida
Orlando, Florida

Fall Term
1992

Major Professor: Michael Bass

ABSTRACT

Spectroscopic studies are presented for Cr^{4+} ions in different hosts. The crystals investigated in this work are divided into two categories. In the first category are included crystals containing chromium in the tetravalent state only. These are purely Cr^{4+} doped crystals. The second category crystals are more complex, containing chromium in both tetravalent and trivalent states. Detailed investigations of the absorption and luminescence characteristics of Cr^{4+} in Cr^{4+}:Y_2SiO_5, which is a purely Cr^{4+} doped crystal, allowed a better understanding to be achieved for the spectroscopic behavior of Cr^{4+} in tetrahedral sites. Based upon these studies theoretical model has been developed for the near infrared fluorescence dynamics of the Cr^{4+} ion. This model now explains many of the inconsistencies and uncertainties that existed in earlier work on Cr^{4+} ion in the more complex crystals such as Cr:Mg_2SiO_4 and can serve as a standard model for future studies of Cr^{4+} in other materials. Also, laser action in the near infrared was demonstrated for the first time in a purely Cr^{4+} doped material, Cr^{4+}:Y_2SiO_5. This confirms the identification of Cr^{4+} as the lasing center responsible for the near infrared laser action in Cr^{4+} doped crystals. The effects of site symmetry and charge compensation on the spectroscopic behavior of Cr^{4+} ions in tetrahedral sites have been taken into account in the present work. This has enabled a new systematic approach to be developed for the crystal field engineering of improved Cr^{4+} laser materials.

Dedicated to the memory of my brother Abhijit Deka

ACKNOWLEDGEMENTS

I would like to thank Dr. Michael Bass for giving me the opportunity to conduct this research and for his guidance throughout this work. I would also like to gratefully acknowledge the moral support of my family during this work. Special thanks are due to Dr. David J. Hagan for his continuous encouragement and help. I thank Drs. Eric VanStryland and David J. Hagan for the use of the Helix cryogenic system, fellow student Paul Buck for his assistance in setting up the system, and Drs. Alan Miller and Patrick Li Kamwa for the use of the Argon-ion and Ti-sapphire lasers. Grateful thanks are due to Dr. Martin Stalder for his able guidance in the initial part of this work and for his help in my transition from areas of theoretical physics to experimental laser physics. I would like to thank Dr. Bruce H.T.Chai for providing all the crystal samples used in this work. The cooperation from Mark Silvers and George Lutts of the crystal growth laboratory are also acknowledged with thanks. I would like to acknowledge the outstanding support from the Department of Physics in general, and particularly thank Drs. Subir Bose, Hari P. Saha, C. Denise Caldwell, Michael Johnson and Ralph A. Llewellynn, and Mrs.Teresa E. Brown and Lynne Giancotti. I also thank Egberto Munin and Sergey A. Usmanov for their understanding and cooperation. Finally I would like to acknowledge the finacial support from the Center for Research in Electro Optics and Lasers (CREOL) during this work.

This research was supported with grants from the Florida High Technology and Industry Council (FHTIC) and Defense Advanced Research Projects Agency (DARPA).

TABLE OF CONTENTS

LIST OF TABLES

LIST OF FIGURES

CHAPTER 1

INTRODUCTION

The objective of this research is to search for alternative hosts for Cr^{4+} ions which can serve as broad band, tunable, near infrared lasers in the 1.2 μm band. The research is based upon detailed spectroscopic studies of Cr^{4+} in different hosts. In this work laser action was demonstrated for the first time in a purely Cr^{4+} doped material, Cr^{4+}:Y_2SiO_5. A systematic study of the spectroscopic and lasing properties of the Cr^{4+} ion in this host enabled a better understanding of the mechanisms involved in the near infrared luminescence of the Cr^{4+} ions in tetrahedral sites to be achieved. The theoretical model developed in the present work for the fluorescence dynamics of this ion explains many of the uncertainties that existed until recently and can serve as a standard for future studies. The result of this work also provides a new guide for a systematic approach to the problem of developing improved Cr^{4+} laser materials.

Chromium has proven to be one of the most widely exploited active laser ions in solid state lasers. Since the discovery of laser action in ruby (Cr^{3+}:Al_2O_3) [1.1], many other the chromium doped solid state lasers based on Cr^{3+} as the active ion have been developed over the past few decades. Examples are Cr:Alexandrite[1.2] and Cr:LiXAF (X=Ca or Sr or the combination of both)[1.3, 1.4]. Cr^{3+} in these crystals occupy substitutional sites having octahedral symmetry. While the ruby laser has sharp line emission at 694 nm Cr:Alexandrite and Cr:LiXAF lasers are all tunable over a wide range of wavelengths. The tuning range of the Cr^{3+} doped laser materials is from 780 nm to about 1 μm [**Table 1.1**]. The tunability of these lasers is the result of the electron- phonon coupling of the excited state to ground state transition[1.5, 1.6]. Above

TABLE 1.1

TUNING RANGES OF COMMON TUNABLE SOLID STATE LASER MATERIALS

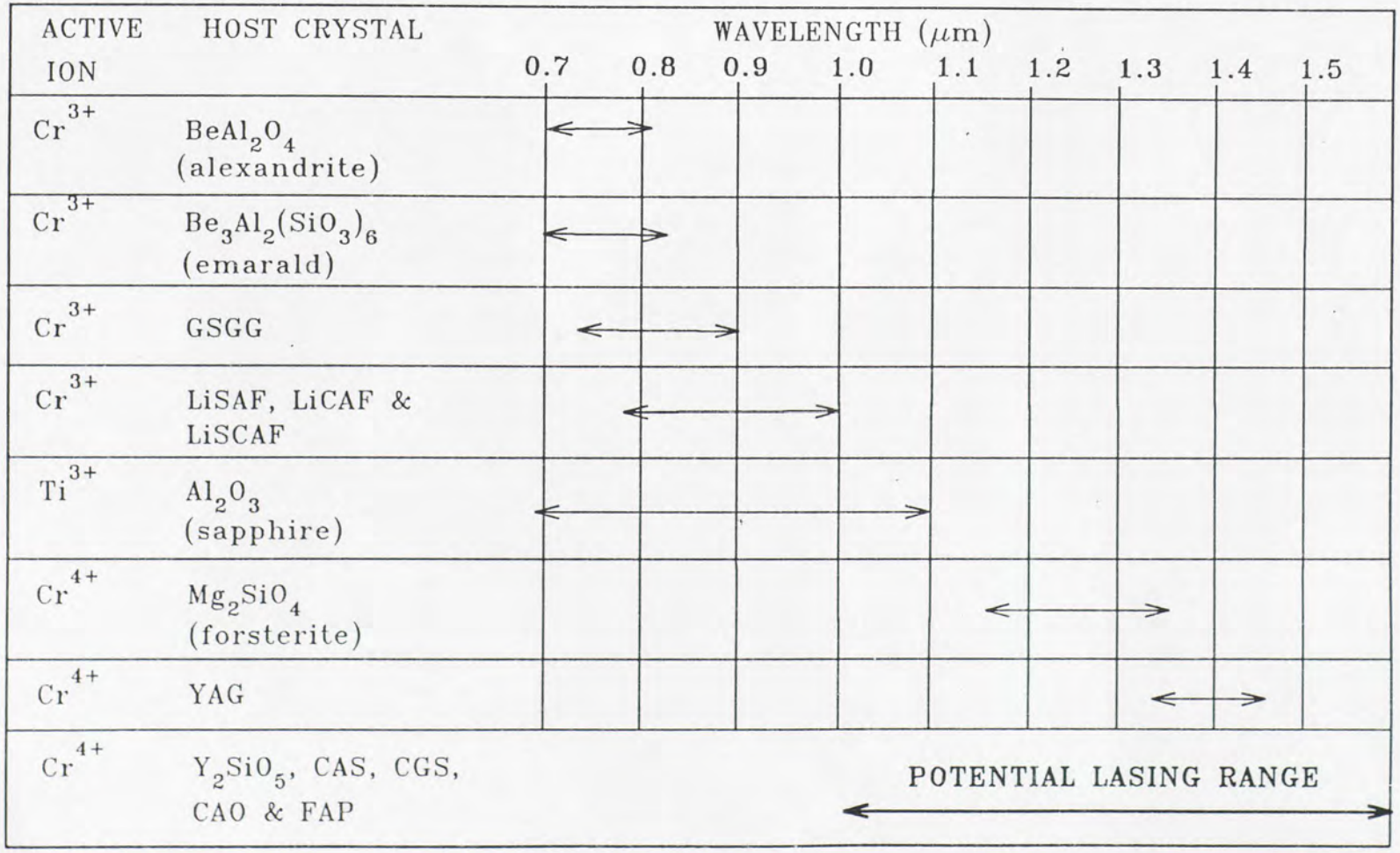

1 μm there is no solid state tunable laser having efficiencies comparable to the commercial Cr^{3+} lasers such as Cr:LiSAF and Cr:LiCAF.

There has been a long felt need for solid state materials that can be efficiently pumped by conventional pumping sources to obtain tunable laser radiation from 1 μm to 1.5 μm. Optical communications systems using fused silica fibers require amplified short pulse laser at around 1.3 μm. There are other sources such as semiconductors but they are only slightly tunable. There are also color center lasers (*e.g.* KCl:Thallium) emitting laser radiation in the 1.3 μm band but the centers in these materials are not very stable and laser operation is possible only at very low temperatures. This is a major drawback of such systems for commercial and industrial applications. Another area in which there is a spectral void as far as solid state lasers are concerned is in providing light for photodynamic therapy (PDT). New drugs are being developed for use in PDT which require tunable laser radiation around 630 nm. A high power tunable solid state laser in the 1.2 μm to 1.4 μm range can provide an all solid state system for that range through efficient second harmonic generation. At present only dye lasers can provide tunable laser radiation in that range but because of the difficulty in the maintenance and the extremely toxic nature of some of the dyes they are not very practical for use in a medical environment. A solid state system could solve those problems.

Demonstration of laser action in Cr:Mg_2SiO_4 (Cr doped forsterite)[1.7] and Ca,Cr:$Y_3Al_5O_{12}$ (Ca,Cr:YAG) in the near infrared (1.2 μm band) has shown[1.8] that Cr^{4+} doped crystals can serve as broad tunable lasers in a wavelength range previously inaccessible by solid state materials. The efficiencies of these two Cr^{4+} lasers are however rather low and in general requires pumping by another laser. The flashlamp pumped laser performance of both of these crystals are quite poor. Besides, the actual mechanisms involved in the near infrared luminescence of Cr^{4+} and the role played by

this ion in the laser action is still not clearly understood. It is important that better solid state materials for doping with Cr^{4+} are soon developed for efficient lasing over a broad tunable range above 1 μm.

Section 1.1: Research Strategy

The project involved three basic areas: (1) crystal growth, (2) spectroscopy and (3) laser studies of Cr^{4+} in different hosts. High quality single crystals were grown by Dr. Bruce H.T. Chai at the Center for Research in Electro-optics and Lasers (CREOL), University of Central Florida (UCF) by the Czochralski technique. The present work concentrates on the spectroscopy and laser studies. It was conducted in close collaboration with the crystal growth laboratory by providing necessary feedback on the characteristics of the grown crystals until high quality samples were obtained for precision spectroscopy and laser experiments. The general plan for the research was as follows:

- Detailed spectroscopic studies of Cr^{4+} ions in different hosts to evaluate the potential laser performance and to understand the physics of ion-ion and ion -lattice interactions of Cr^{4+} in different crystal environments and investigate the effects of site symmetry and charge compensation on the spectroscopic properties of the Cr^{4+} ions.
- Development of theoretical models to describe the properties of some of the crystals for a better understanding of the physics of laser media.
- Correlating high precision spectroscopy and crystallography in order to predict new host materials for d^2 -class of ions (Cr^{4+}, V^{3+}) with better optical properties for efficient lasing.
- Test laser performance of new crystals.
- Optimize pump source, pump cavity and laser resonator.

- Improve crystal growth, post growth treatment and crystal quality.

To understand the spectroscopic behavior of the Cr^{4+} ion in the tetrahedral site in a crystalline host detailed investigations of the absorption and fluorescence spectra, fluorescence intensity and lifetime, the temperature dependence of the lifetime and intensity are necessary. A proper interpretation of such experimental data requires taking into consideration the various factors which can influence the optical properties of the active ion in different hosts, such as the effects of site symmetry, charge compensation, ion-lattice interactions and also possible energy transfer processes resulting from ion-ion interactions. In order to be able to clearly understand the possible mechanisms involved in the luminescence of the Cr^{4+} ions in tetrahedral sites, the near infrared emission from chromium doped crystals of two general types were investigated.

(i) The first type has only tetrahedral sites where Cr^{4+} can enter and there is no charge compensation requirement in the doping process (Cr^{4+}:Y_2SiO_5, Cr^{4+}:$Ca_2Al_2SiO_7$, Cr^{4+}:$Ca_2Ga_2SiO_7$). These are purely Cr^{4+} doped systems.

(ii) The second type (Cr:Mg_2SiO_4 and Ca:Cr:$Y_3Al_5O_{12}$) of crystals are more complex, the complexities arising from (a) the presence of Cr^{3+} in octahedral sites and (b) requirement for charge compensation in the doping process (Cr^{3+} substitutes for Mg^{2+} in Cr:Mg_2SiO_4 and Cr^{4+} substitutes for Al^{3+} in $Y_3Al_5O_{12}$).

The study of the crystals of the first category enabled the optical properties of the Cr^{4+} ions to be investigated without the inherent complexities encountered in the crystals of the second category. For example, one of the major points of controversy in forsterite concerns the Cr^{3+} ions which enter two types of inequivalent Mg^{2+} sites. The presence of these ions together with Cr^{4+} makes a definitive interpretation of the observed spectroscopic data quite difficult. The effect of these ions on the emission properties of the Cr^{4+} ions has not been studied in detail until now. The same comments

hold for the effect of charge compensation, required when there is a charge mismatch between the impurity ion and the ion it substitutes in the host, on the spectroscopic properties of the system. For example in chromium doped forsterite trivalent chromium ions substitute for divalent magnesium ions and Cr^{4+} substitutes for Al^{3+} in Ca,Cr:YAG. Whereas Ca^{2+} serve as the charge compensating ion in Ca, Cr:YAG no additional charge compensating element is added in forsterite and the actual charge compensation mechanism is not known in this crystal. These problems are not present in the crystals mentioned in the first category and therefore the strategy for the present work was to first acquire a better understanding of the Cr^{4+} ion spectroscopy in the tetrahedral site in these crystals and then conduct comparative studies of the spectroscopy with the more complex crystals such as $Cr:Mg_2SiO_4$. This has helped clear up many of the uncertainties in elucidating the mechanisms involved in the near infrared luminescence of the Cr^{4+} ion in the tetrahedral site. Such information is important for the development of other efficient new Cr^{4+} doped laser crystals.

Section 1.2: Outline of the dissertation:

The general outline of the dissertation is as follows. In Chapter 2 a brief survey of previous work on Cr^{4+} doped materials is presented. The experimental data on the spectroscopy are presented in Chapter 3. Chapter 4 outlines the general theory of the spectroscopy of transition metal ions in crystals with special emphasis on the d^2 ions in tetrahedral sites. Theoretical analyses of the spectroscopic results are presented in Chapter 5 and in Chapter 6 the lasing properties of the first pure Cr^{4+} doped material $Cr^{4+}:Y_2SiO_5$ are discussed. The general discussion and conclusion of the present work are included in the last chapter.

CHAPTER 2

PREVIOUS WORK ON Cr^{4+}

Earlier mention of Cr^{4+} is found only in reference to its negative influence on the laser performance of other ions in the near infrared due to its near infrared absorption at around 1.0 μm [2.1]. Until recently, therefore, in crystals in which Cr^{3+} was desired much care was taken to grow the crystals in environments which inhibits inclusion of chromium in its tetravalent state. However, in 1988 Petricevic *et. al.* demonstrated laser action of the chromium doped Mg_2SiO_4 (Cr:Forsterite) in the near infrared (NIR) @ 1235 nm [2.2]. The free running laser spectrum, excited by 532 nm radiation from a frequency doubled Nd:YAG laser, had a band width of 22 nm and showed potential for tunability in a broader wavelength range. The laser action was initially interpreted as due to the transition of the Cr^{3+} ion from the $^4T_2$ first excited state to the $^4A_2$ ground state. Cr:Forsterite also showed a relatively weak but broad absorption band from 850 nm to 1200 nm. This band could not be attributed to the Cr^{3+} ion and was presumed to be due to some impurity. A similar absorption band was observed earlier in Cr,Nd:GSGG (gadolinium scandium gallium garnet) [2.3, 2.4, 2.5] where it was found to decrease the efficiency of the Nd^{3+} emissions and effort was made to get rid of the absorbing "center" by improving the crystal growth technique, or annealing the crystal in reducing atmosphere[2.6 (Ref 11. in Ref. 2.8)]. It was suggested that by lowering the 'parasitic' absorption in this band the spectral range of the observed near infrared laser action in Cr:Forsterite could probably be extended from 850 nm to 1300 nm[2.2]. Later in the same year, however, the authors reported that laser action was obtained in the same NIR band also by pumping directly into the near infrared

absorption band with 1064 nm radiation from a Nd:YAG laser[2.7]. This indicated that the reported NIR laser action may not be due to the Cr^{3+} ion and could in fact be due to the "center" that also has the broad near infrared absorption. It was suggested that this center could actually be a Cr^{4+} ion which substitutes for the Si^{4+} ion in the tetrahedral site[2.8] and not due to any other impurity as was suspected earlier. This triggered off extensive efforts to develop and improve crystal growth techniques whereby the Cr^{4+} ion could be more efficiently doped and Cr^{3+} eliminated as much as possible so that efficient Cr^{4+} laser action may be obtained in the NIR. At the same time considerable efforts were employed to confirm the suggestion that the lasing center is indeed Cr^{4+} in a tetrahedral site as had been suggested. As a result, extensive spectroscopic investigations were undertaken between 1988 and 1991 to analyze the absorption and emission properties of chromium doped forsterite grown in a wide variety of atmospheres. In this effort the articles by Verdun *et. al.* [2.9] and Moncorge *et. al.* [2.10, 2.11] deserves special mention because of their detailed experimental work on the absorption and emission of the chromium ion in forsterite. For the work described in Ref.[2.9] the chromium-aluminum doped forsterite crystal was grown in oxidizing atmosphere to obtain a predominantly Cr^{4+} doping. The low temperature absorption spectrum in the near infrared was characterized by sharp line structures accompanying a zero phonon line. These structures were interpreted in terms of lattice vibration and tetrahedral vibration modes of different frequencies. The symmetry of the Cr^{4+} site was suggested to be C_S and theoretical values of the different energy levels of the Cr^{4+} ion were predicted using the Tanabe-Sugano diagram[2.12]. The NIR absorption and fluorescence was attributed to the radiative transitions of the Cr^{4+} ion between the $^3A_2$ ground state and the crystal field components of the $^3T_2$ parentage. Further, the symmetry selection rule forbids radiative electric dipole transition between $^3T_2$ and $^3A_2$ in the ideal tetrahedral symmetry. As a result it was

suggested that the electric dipole radiative transition probabilities could be expected to be small for transitions involving the crystal field components of $^3T_2$ parentage in low symmetry fields and therefore explain the observed weak absorption and fluorescence in the NIR. However in that case the lifetime of the upper states should have been long whereas experiments showed that the low temperature lifetime of the NIR fluorescence was only ~30 μs. No attempt was made to explain this discrepancy. The laser action of Cr:Forsterite in the NIR reported by Verdun *et. al.* had an efficiency of 10 % with an outcoupler of 94 % reflectivity. This was rather low for a laser pumped laser and was attributed to a possibly low quantum efficiency of the Cr^{4+} for the NIR emission. However, again, no attempt was made to explain such low quantum efficiencies. In references [2.10, 2.11] by Moncorge *et. al.* fluorescence analyses were presented for the visible as well as the NIR emissions of the chromium ions in forsterite. Time resolved spectroscopy indicated the presence of three luminescent centers; two were identified as Cr^{3+} which were responsible for the fluorescence in the visible and the near infrared band around 900 nm. The NIR fluorescence in the 1150 nm - 1300 nm band was attributed to the Cr^{4+} ions substituted in Si^{4+} sites. Important points to note in that report were: (1) only single exponential decays (τ=2.7 μs) in the 1150 nm - 1300 nm band were observed for excitation by 575 nm, 640 nm and 1092 nm pump radiation; (2) non-exponential decays were observed below 1150 nm and the transients were observed to be sum of two exponential components, the lifetimes corresponding to these components depending upon both the excitation and the emission wavelengths; (3) the zero phonon line of the Cr^{4+} fluorescence observed at around 1092 nm was resolved into three fine structure components but because of the non-Boltzmann distribution of the intensities of the three components they could not be interpreted as the spin-orbit split components of the $^3T_2$ state. The possibility of emission from the ^1E state, besides the $^3T_2$ state, was considered but later discounted because of the failure to prove the

thermalization of these two states that would be expected in a strong crystal field environment. In 1991 W. Jia *et. al.*[2.13], working on chromium doped single crystal fibers, also reported resolution of the three components in the zero phonon line. For reasons not explained in the article, the Cr^{4+} site symmetry was not taken as C_S as was correctly suggested earlier by Verdun *et. al.*[2.9]. The crystal field components of the $^3T_2$ and $^3T_1$ states were suggested to be $^3A_1$, $^3B_1$, $^3B_2$ and $^3A_2$ $^3B_1$, $^3B_2$. Such assignments would suggest that the symmetry of the Cr^{4+} site assumed in this work was C_{2V}. The NIR spectrum (**E** || **b**) was attributed to the $^3A_1(^3T_2) - {}^3A_2$ transition. However this assignment seems rather arbitrary in view of the fact that in C_{2V} the $^3A_1(^3T_2) - {}^3A_2$ transition is symmetry forbidden for all polarizations. Interestingly the same symmetry assignments were used also by Baryshevski *et. al.*[2.14]. The extent of arbitrariness in such symmetry assignments are obvious from the fact that in Ref.2.14 the authors claim, in the introduction, to have proved by direct EPR experiments the hypothesis that the Cr^{4+} site has a C_S symmetry but in the rest of the article they assume a C_{2V} symmetry to interpret their spectroscopic data. In the same article it was suggested that energy transfer takes place from Cr^{4+} to Cr^{3+}. This conclusion was based upon the observation of EPR signals from Cr^{3+} ions following 0.53 μm and 0.62 μm excitation and the absence of any such signals following 1.06 μm excitation *and* the hypothesis that there was no direct excitation of Cr^{3+} ions in any case. Such a hypothesis, however, is not supported by any of the other works in the spectroscopy of the chromium doped forsterite.

While the uncertainty concerning the spectroscopy of chromium ions in forsterite persisted, much progress was made in the area of laser action of Cr^{4+} in that host. Room temperature flashlamp pumped tunable laser operation of Cr^{4+}:Forsterite was first reported by Sugimoto *et. al.*[2.15] in 1989 with a tuning range of 1206 nm – 1250 nm and slope efficiency of ~0.0024 % using an outcoupler of 95 %

reflectivity. Maximum output energy reported was 4.95 mJ with an input of 283.0 J of electrical energy. Baryshevski *et. al.*[2.14] showed tunability of the flashlamp pumped laser operation from 1170 nm to 1330 nm obtaining a maximum energy of more than 50.0 mJ and a maximum slope efficiency of 0.0067 % at 1235 nm. In laser pumped laser operation they reported more than 2.0 J output energy in the pulsed free running mode for an input of about 16.0 J from a free running Nd-Glass laser. Segawa *et. al.*[2.16] reported Q-switched operation of flashlamp pumped Cr^{4+}:Forsterite laser from 1206 nm to 1264 nm obtaining pulses of 60 ns – 80 ns duration. The laser output at the peak wavelength of 1230 nm was 13 mJ for an input electrical energy of 283 J. The room temperature laser pumped laser operation in the free running cw-mode was first reported by Petricevic *et. al.*[2.17]. The maximum reported slope efficiency was 6.8 % and the free running spectrum peaked at 1244 nm. The slope efficiency was latter improved to 37.85 % for an outcoupler reflectivity of 89 % for output wavelength of 1242 nm[2.18]. CW active mode-locked operation of Cr:Forsterite was demonstrated by Seas *et. al.* obtaining pulses as short as 20 ps tunable between 1204 nm and 1277 nm[2.19]. Synchronously pumped mode locking was also reported in the tunable range of 1195 nm-1295 nm producing pulses of the order of 260 ps. Recently Pollock *et. al.*[2.20] reported self mode-locked operation of the Cr:Forsterite laser using a Nd:YAG laser as the pump source.

Besides Cr:Forsterite the only other Cr^{4+} doped crystal that was observed to lase in 1989 was Ca,Cr:YAG. Zverev *et. al.*[2.21] demonstrated the laser action of the tetravalent chromium ion in Ca,Cr:YAG with a tuning range of 1.35 μm–1.50 μm and obtained efficiencies of 7-8 % for quasi-cw Nd:YAG pumping at room temperature. The laser action in this crystal was attributed to the $^3T_2 - {}^3A_2$ transition of the Cr^{4+} ion substituting for Al^{3+} in a distorted tetrahedral site (S_4)[2.21, 2.22]. Allik *et. al.*[2.23] conducted preliminary spectroscopic investigations on Cr^{4+} doped $Ca_2Al_2SiO_7$ and

$Ca_2Ga_2SiO_7$ but neither crystals could be lased even at low temperature (15 °K). Cr^{4+} ions doped into Akermanite hosts $Ba_2MgGe_2O_7$ and $Ca_2MgSi_2O_7$ were investigated by Garrett *et. al.*[2.24] but no luminescence was observed from these crystals either at room temperature or at 10 °K. Thus, until recently, among all the Cr^{4+} doped crystals only Cr^{4+}:Forsterite has proved to be a fairly efficient laser in the near infrared and significant spectroscopic work has been conducted for this crystal. However, in spite of the large volume of experimental data generated within a very short period of time following the first report on the successful laser operation of the Cr^{4+} ion in Mg_2SiO_4 a clear understanding of the behavior of this ion in the tetrahedral site and the actual role it played in the near infrared laser action was not available.

CHAPTER 3

EXPERIMENTS

This chapter is concerned with the experimental part of the spectroscopy. It includes the aim and the strategy of the experiment, experimental procedures and experimental results. A brief discussion is presented also for the growth of Cr^{4+} doped materials investigated in this work.

Section 3.1: Crystal Growth

Single crystals of $Ca_2Al_2SiO_7$ (CAS), $Ca_2Ga_2SiO_7$ (CGS), Y_2SiO_5 (YSO), Mg_2SiO_4 (Forsterite), $Y_3Al_5O_{12}$ (YAG), $CaAl_4O_7$ (CAO) and $Ca_5(PO_4)_3F$ (FAP) were grown by the Czochralski technique. The hot zone of the growth station was constructed with stabilized zirconia tubing and zirconia bubbles to maintain the high temperatures required to grow these crystals. The hot zone was surrounded by the fused silica tube to provide control of ambient atmosphere. The iridium crucibles used to hold the melt during the growth was 76 mm in diameter and 76 mm high. The crystals were pulled at rates between 1-3 mm/hr and rotated 15-40 rpm. For the first growth runs of each of the above crystals an iridium wire was used to initiate spontaneous nucleation to obtain the seed crystals. Table 3.1 gives the salient features for the growth of the crystals mentioned above. Details of the crystals growth of the different Cr^{4+} doped crystals investigated in this work are given in Refs. 3.1 and 3.2.

TABLE 3.1

SUMMARY OF GROWTH PARAMETERS FOR Cr^{4+} DOPED CRYSTALS*

Crystal	Base Compounds	Melting point (°C)	Atmosphere	Pull Rate
$Cr^{4+}:Y_2SiO_5$	Y_2O_3, SiO_2, Cr_2O_3	2070	N_2	1-1.5 mm/hr @ 20-40 rpm
$Cr^{4+}:Ca_2Al_2SiO_7$	Al_2O_3, SiO_2, Cr_2O_3	1565	N_2	1-1.5 mm/hr @ 20-40 rpm
$Cr^{4+}:Ca_2Ga_2SiO_7$	Ga_2O_3, SiO_2, Cr_2O_3	1465	N_2	1-3 mm/hr @ 15-30 rpm
$Cr:Mg_2SiO_4$	MgO, SiO_2, Cr_2O_3	1890	Both N_2 and $N_2 + O_2$	1-3 mm/hr @ 20-30 rpm
$Ca,Cr:Y_3Al_5O_{12}$	Y_2O_3,Al_2O_3, Cr_2O_3,$CaCO_3$	1940	Both N_2 and $N_2 + O_2$	1 mm/hr @ 15 rpm
$Be,Cr:Ca_2Al_4O_7$	Al_2O_3,Cr_2O_3, $CaCO_3$	1762	N_2	1 mm/hr @ 20 -30 rpm
$Cr^{4+}:Ca_5(PO_4)_3F$	$CaCO_3$,$CaH(PO_4)$, CaF_2, Cr_2O_3	1762	N_2	1-2 mm/hr @ 33-15 rpm

***Refs. [3.1, 3.2].**

Section 3.2: Experimental Procedures for Spectroscopy

Measurements of the absorption spectra from the ultraviolet to the infrared were performed with a Perkin Elmer Spectrophotometer (Model 330) interfaced with a computer for direct data acquisition. For the low temperature absorption measurements a liquid nitrogen dewar (Kadel Engineering) with sapphire windows was used. The mounts in the spectrophotometer were modified to accommodate the dewar. Care was taken to shield the system from outside stray light.

The luminescence measurements were conducted by exciting the crystal samples with a pulsed Nd:YAG Q-switched laser (Advanced Laser Systems Inc.) having pulse duration of about 15 ns. Both the fundamental 1064 nm and second harmonic 532 nm were used as pump wavelengths. The schematics for the luminescence experiments are shown in **Fig. 1**. The sample under investigation was mounted on the cold finger of a closed loop compressed helium cooled cryostat (Helix Technology Corp . Model 8300 helium compressor, Model 8001 controller, LakeShore Model DRC 91C temperature controller). The excitation laser beam was introduced through a quartz window of the cryostat and the fluorescence measured in the perpendicular direction through a second quartz window. The fluorescence light was transmitted through a scanning monochromator (Jarrel Ash) and detected by a fast InGaAs photodiode. A fast digital storage scope (Tektronix Model 2340) in combination with a computer served to average and measure the signal from the photodiode. The response time of the detection system was 10 ns. The input signal into the photodiode was pre-amplified (Analog Module Inc. Model 312-A) before being fed into the digital oscilloscope. The gain of the amplifier was set at 560 kV/amp.

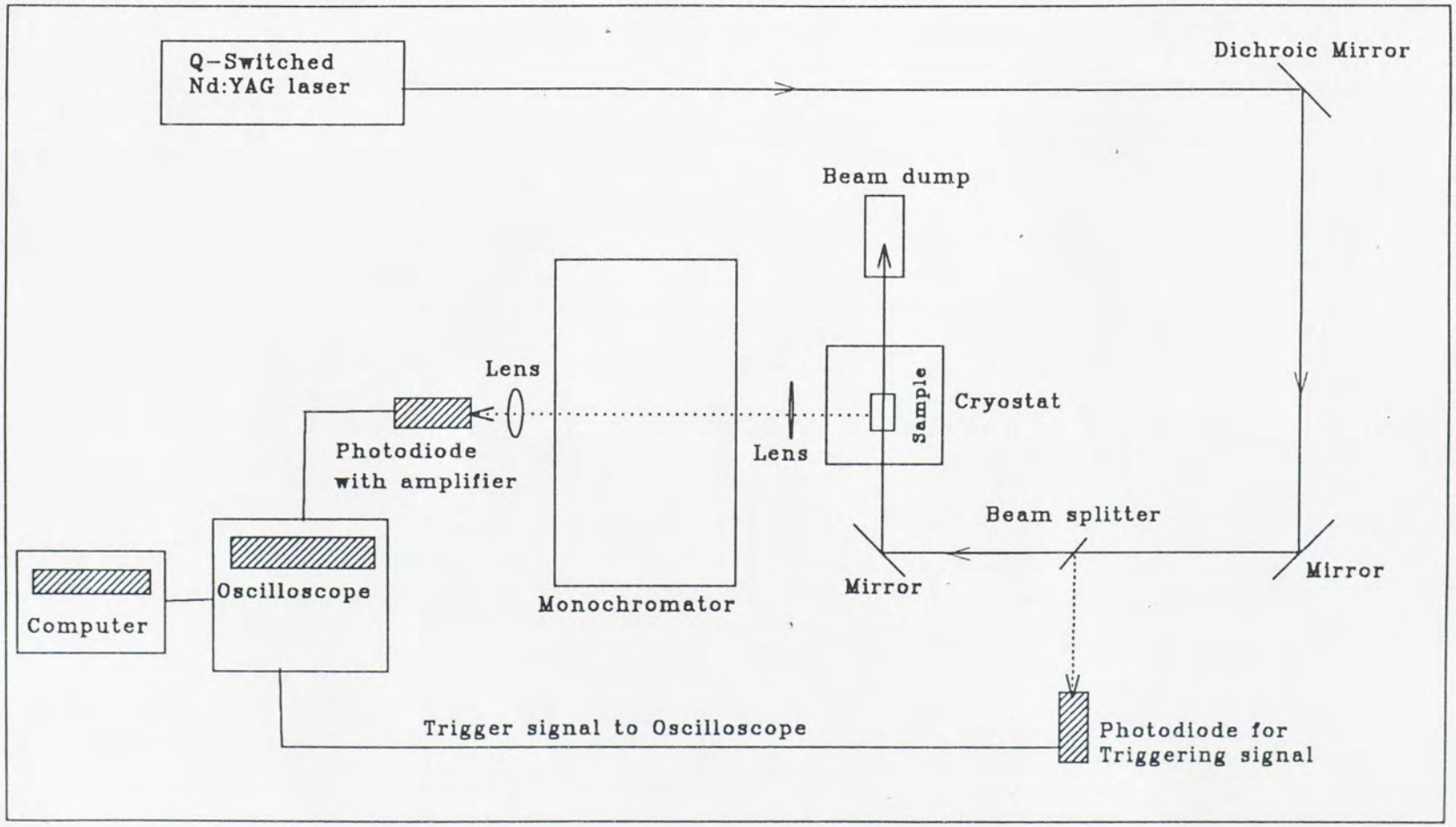

Figure 1. Schematic diagram of the fluorescence spectroscopy experiment.

Section 3.3: Experimental strategy

The aim of the spectroscopic investigations of the Cr^{4+} ion in the tetrahedral site in different types of hosts was

(i) to characterize the Cr^{4+} doped crystals to evaluate their potential laser performance,

(ii) to obtain a better understanding of the optical properties and the near infrared fluorescence dynamics of the Cr^{4+} ion in a tetrahedral site in a purely Cr^{4+} doped system and use this system as a *standard* reference material in the study of the optical properties of the Cr^{4+} ion in more complex crystals such as $Cr:Mg_2SiO_4$. In this effort the present work was guided by the conditions that the desired *standard crystal* host must not allow Cr^{3+} in the lattice, the Cr^{4+} must have a strong fluorescence in the crystal and show Cr^{4+} broad band laser action in the near infrared.

Table 3.2 and Table 3.3 show the qualitative comparison of different Cr^{4+} doped crystals. Because of its favorable characteristics $Cr^{4+}:Y_2SiO_5$ was selected as the standard crystal on which to base a theoretical model for the fluorescence dynamics of the Cr^{4+} ion in the tetrahedral site. The crystallographic parameters of the different samples are presented in Table 3.4.

Section 3.4: Spectroscopic data.

The polarized absorption spectra of $Cr^{4+}:Y_2SiO_5$ at room and liquid nitrogen temperatures are shown on Figure-2(a) and 2(b) respectively. Figure-3 shows the fluorescence spectra.

$Cr:Mg_2SiO_4$ is a complex system. Its spectroscopic properties depend upon the growth environment of the samples as well as pump wavelengths because of the presence of chromium in both trivalent (Cr^{3+}) and tetravalent (Cr^{4+}) states. Figs. (4) and Figs.(5) show the spectroscopic properties of Cr-doped forsterite samples grown in

pure nitrogen atmosphere and partial oxygen atmosphere respectively. The implications of the observed differences and/or similarities in the two sets of data will be discussed in Chapter 5.

The luminescence of Cr^{4+}:$Ca_2Ga_2SiO_7$ is extremely weak and requires the use of lock-in amplifier for detection[3.4]. Because of its similarity to Cr^{4+}:$Ca_2Al_2SiO_7$ as far as crystal structure and crystal field strength are concerned no new measurements of thefluorescence from Cr^{4+}:$Ca_2Ga_2SiO_7$ was taken for this crystal. Fig. (6) shows the polarized absorption spectra of Cr^{4+}:$Ca_2Ga_2SiO_7$ and Cr^{4+}:$Ca_2Al_2SiO_7$ reproduced from Ref. 3.4. The results of detailed fluorescence lifetime measurements in Cr^{4+}:$Ca_2Al_2SiO_7$ showed some interesting new features. The fluorescence spectra of Cr^{4+}:$Ca_2Al_2SiO_7$ due to different pumping are shown in Fig.(7) and the fluorescence decay curves at different temperatures and wavelengths due to different excitations are shown in Fig. (8). For comparison the fluorescence spectra of Cr^{4+}:$Ca_2Al_2SiO_7$ measured earlier by Allik et. al. are also shown in Fig. (9).

Be,Cr^{4+}:$CaAl_4O_7$ showed no luminescence. The room temperature polarized absorption spectra are shown in Fig. (10).

Cr^{4+}:$Ca_5(PO_4)_3F$ absorption spectrum is shown in Fig.(11). At room temperature the crystal has a broad fluorescence band from 1075 nm to 1680 nm (Fig.12) and a fluorescence lifetime of about 100 μs.

Figs. (13) to (15) shows the absorption and the near infrared emission spectra of Ca,Cr:$Y_3Al_5O_{12}$. The fluorescence decay curves essentially follow single exponential forms with a small initial curvature. The present measurements verify the results on this crystal already published in the literature [3.8]. Similar to Cr:Mg_2SiO_4, Ca,Cr:$Y_3Al_5O_{12}$ also contains both Cr^{3+} and Cr^{4+}.

TABLE 3.2

FLUORESCENCE INTENSITY OF Cr^{4+} IN DIFFERENT HOSTS IN THE 1.1 - 1.5 μm BAND

Crystal	Intensity at room temperature	Intensity at liquid nitrogen temperature
$Cr^{4+}:Y_2SiO_5$	Moderate	Strong
$Cr^{4+}:Ca_2Al_2SiO_7$	Weak	Weak
$Cr^{4+}:Ca_2Ga_2SiO_7$	Very weak	Very weak
$Cr:Mg_2SiO_4$	Strong	Strong
$Ca,Cr:Y_3Al_5O_{12}$	Weak	Weak
$Be,Cr:Ca_2Al_4O_7$	No Fluorescence	No Fluorescence
$Cr^{4+}:Ca_5(PO_4)_3F$	Weak	Weak

TABLE 3.3

TRIVALENT CHROMIUM SITES AND CHARGE COMPENSATION REQUIREMENTS IN DIFFERENT HOSTS

Crystal	Acceptable Octahedral Sites for Cr^{3+} ?	Charge Compensation Requirements
$Cr^{4+}:Y_2SiO_5$	No	No
$Cr^{4+}:Ca_2Al_2SiO_7$	No	No
$Cr^{4+}:Ca_2Ga_2SiO_7$	No	No
$Cr:Mg_2SiO_4$	Yes	Yes
$Ca,Cr:Y_3Al_5O_{12}$	Yes	Yes
$Be,Cr:Ca_2Al_4O_7$	No	Yes
$Cr^{4+}:Ca_5(PO_4)_3F$	No	Yes

TABLE 3.4

CRYSTALLOGRAPHIC CHARACTERISTICS OF THE SAMPLES STUDIED

Host	Space group	Crystallographic parameters (°A) [3.1]	Cr^{4+} site symmetry	Average Cr^{4+} – ligand distance (°A)
Y_2SiO_5	C2/c	a= 10.4987 b= 6.7658 c= 12.577	C_{3v}	1.63 [3.3]
$Ca_2Al_2SiO_7$	P42m	a= 7.6884 b= 7.6884 c= 5.0701	C_{3v}	1.684 [3.4, 3.5]
$Ca_2Ga_2SiO_7$	P42m	a= 7.8078 b= 7.8078 c= 5.1400	C_{3v}	1.723 [3.4, 3.6]
Mg_2SiO_4	Pnmb	a= 4.7805 b= 10.2633 c= 6.002	C_s	1.635 [3.4, 3.7]
$Y_3Al_5O_{12}$	Ia3d	a= 12.024 b= 12.024 c= 12.024	S_4	_____
$Ca_2Al_4O_7$	C2/c	a= 12.922 b= 8.967 c= 5.462	_____	_____
$Ca_5(PO_4)_3F$	$P6_3/m$	a= 9.4222 b= 9.4222 c= 6.9152	_____	_____

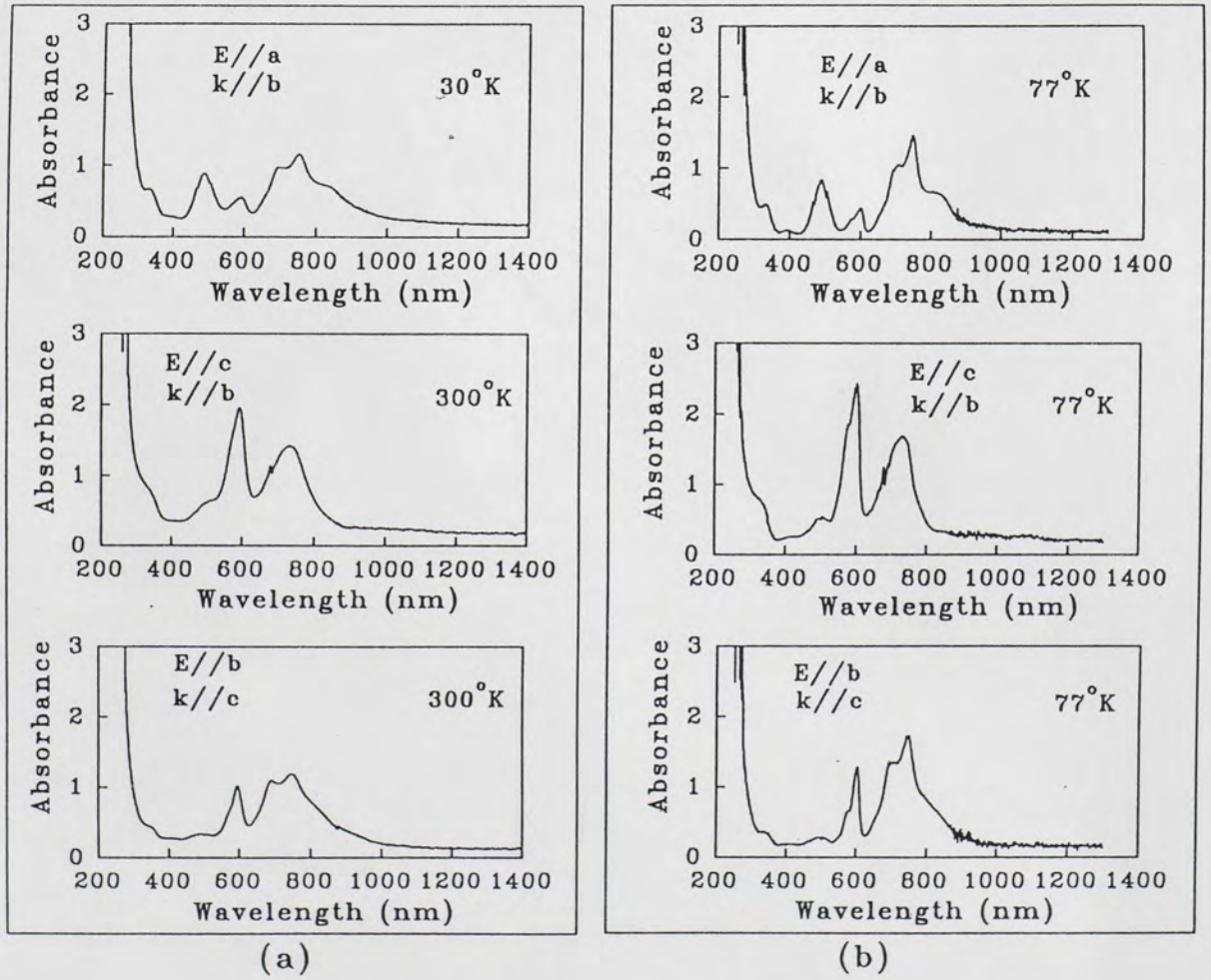

Figure 2. Polarized absorption spectra of Cr^{4+}:Y_2SiO_5 at (a) room temperature and (b) 77 ^{o}K.

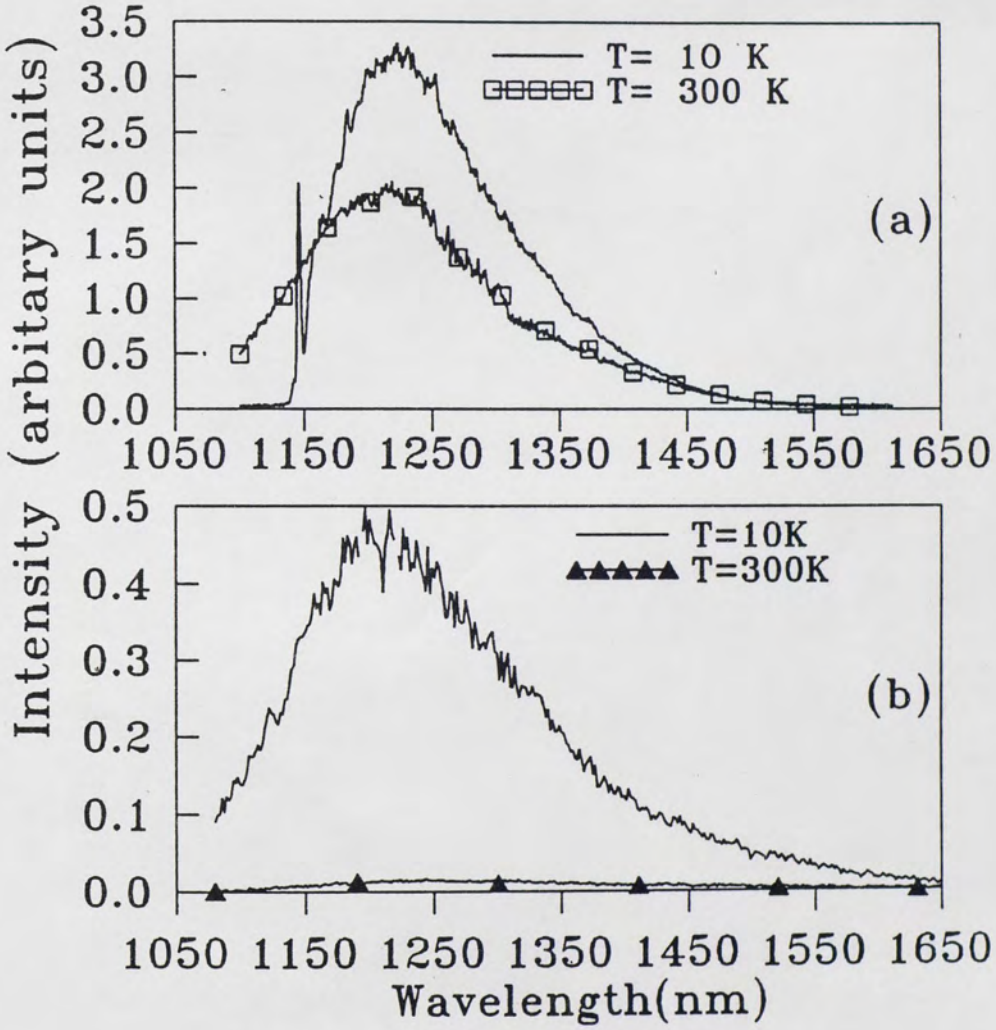

Figure 3. Fluorescence spectra of Cr^{4+}:Y_2SiO_5 at different temperatures due to excitation at (a) 1064 nm and (b) 532 nm.

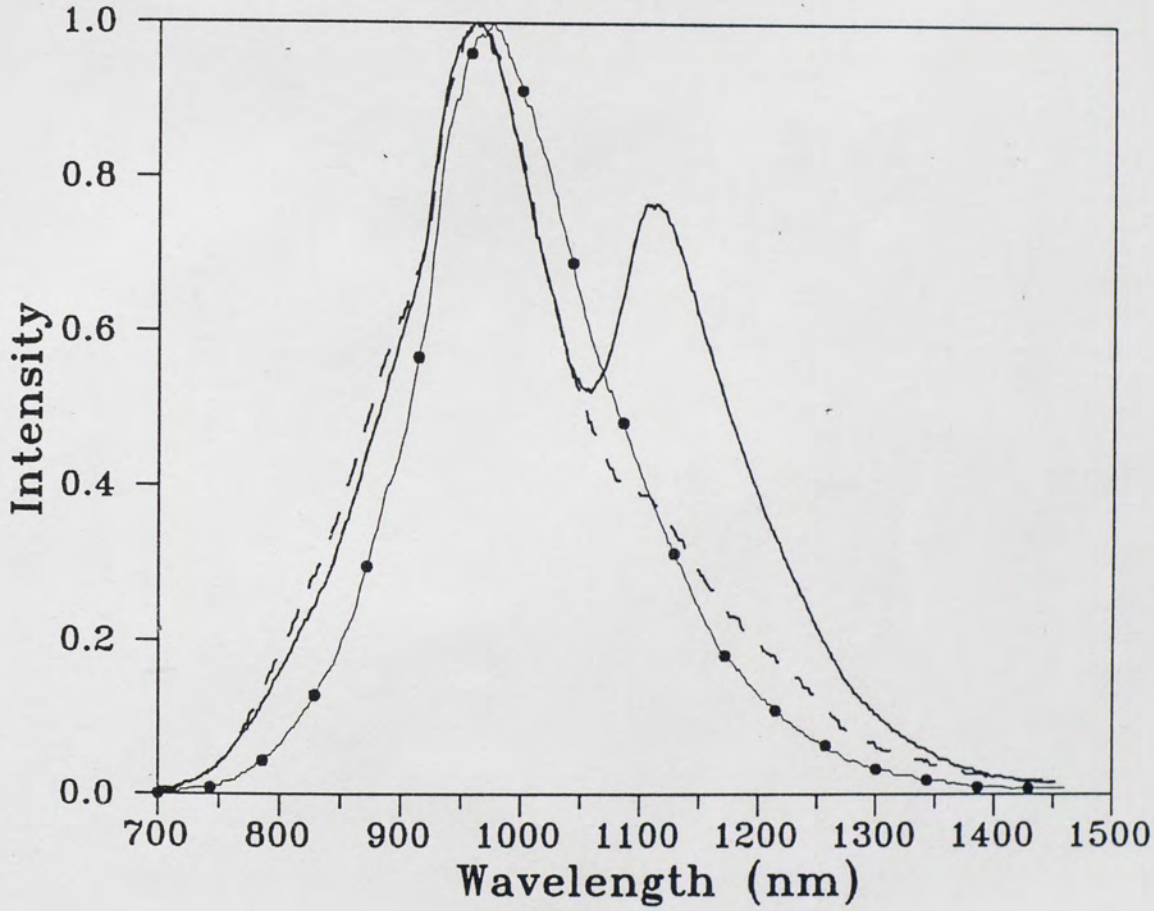

Figure 4(a). Polarized fluorescence spectra of Cr:Mg_2SiO_4 (sample #2, growth atmosphere: pure nitrogen) at room temperature. The pump wavelength was 532 nm.

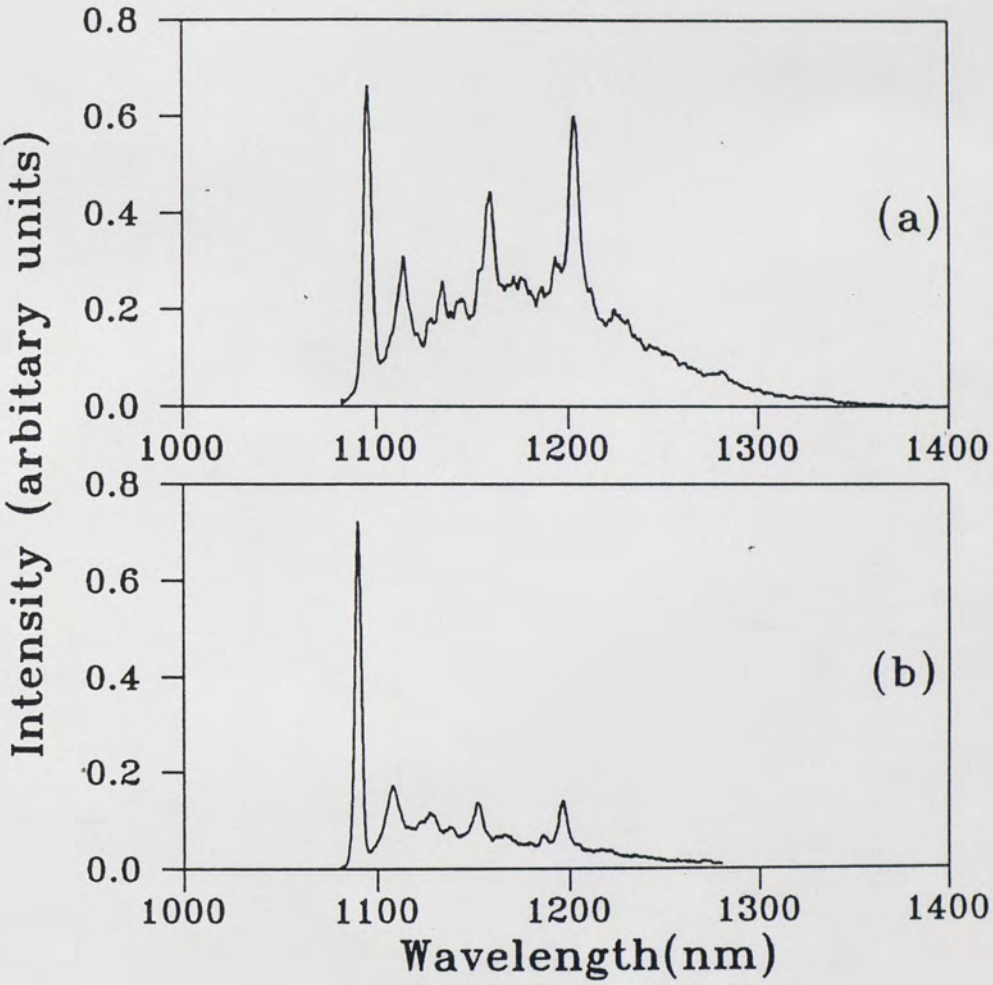

Figure 4(b). Fluorescence spectrum of Cr:Mg_2SiO_4 grown under pure nitrogen atmosphere (sample #2) at 9.5 ^{o}K after prolonged exposure of the sample to laser radiation at (a) 532 nm, and (b) 1064 nm. The pump wavelength in both cases was 1064 nm.

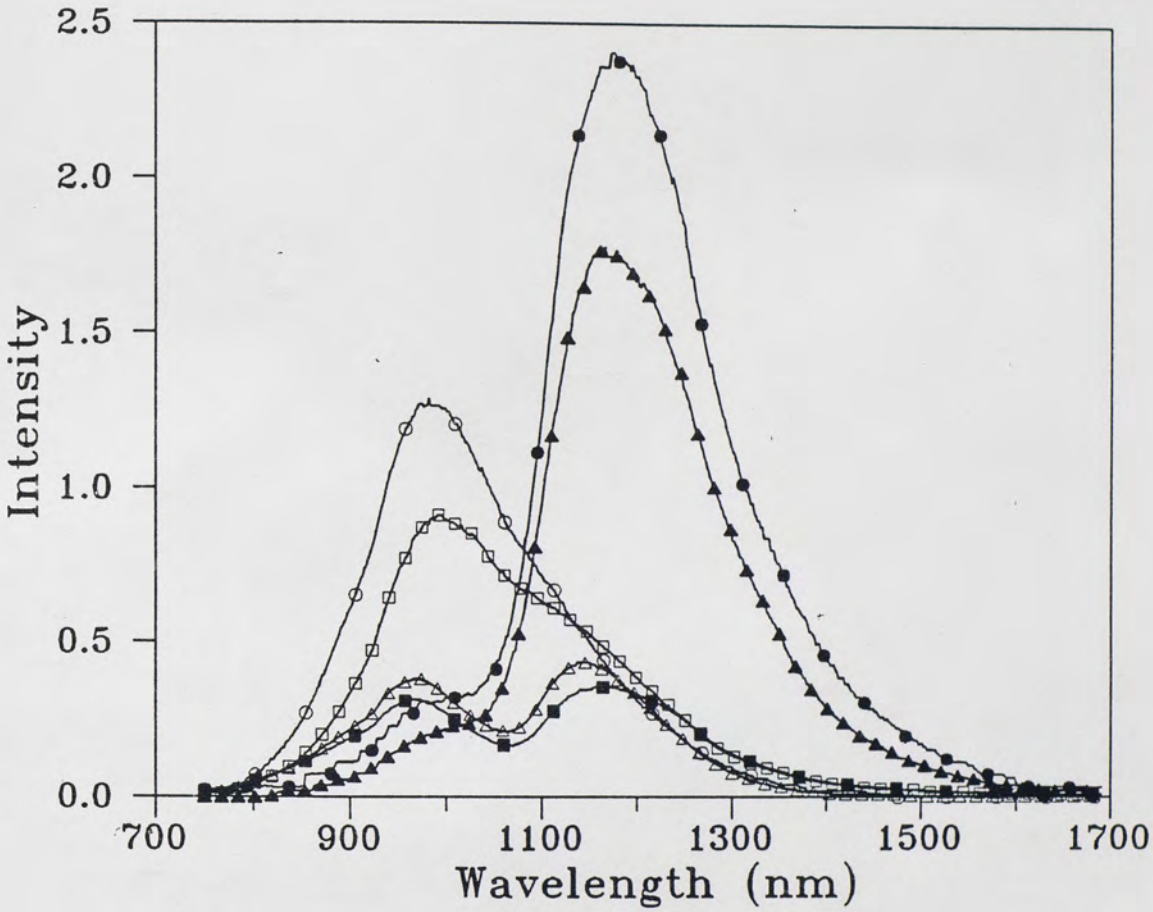

Figure 5(a). Polarized fluorescence spectra of Cr:Mg_2SiO_4 (sample#1, growth atmosphere: partial oxygen) at room temperature. The pump wavelength was 532 nm.

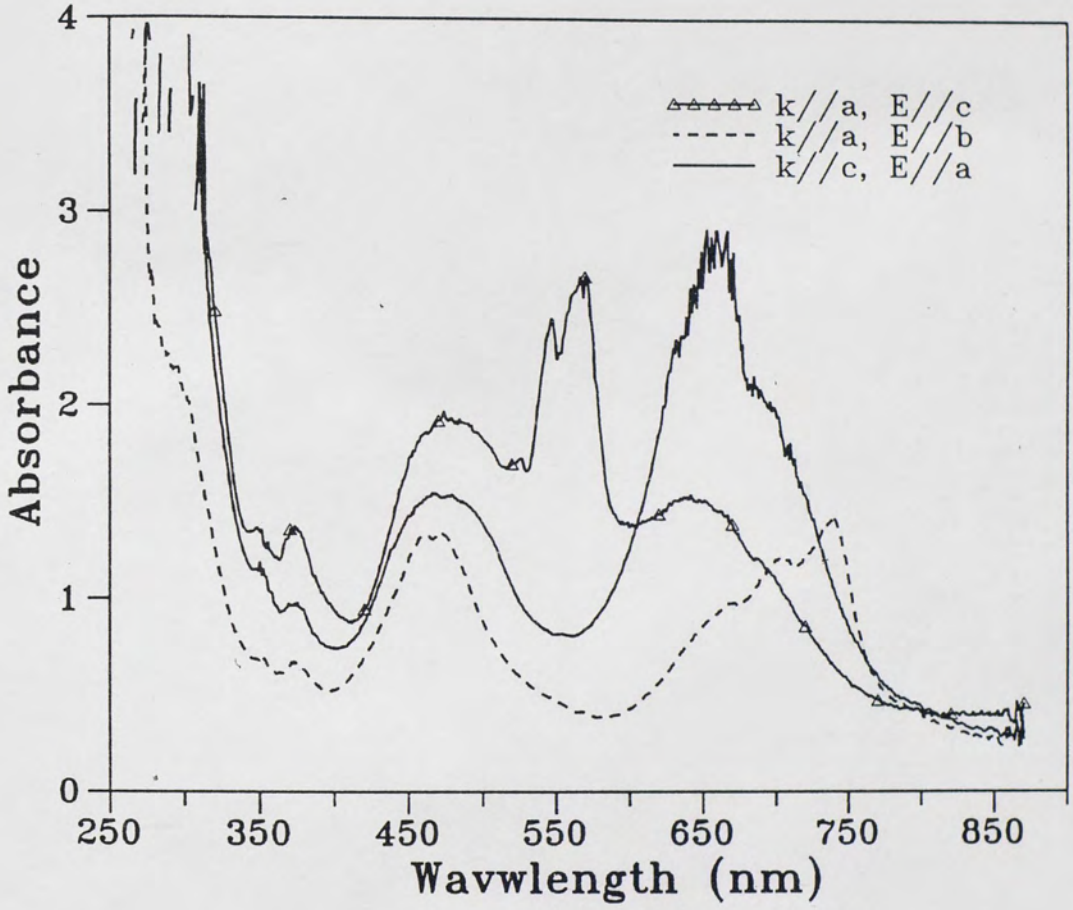

Figure 5(b). Polarized absorption spectra of Cr:Mg_2SiO_4 (sample #1).

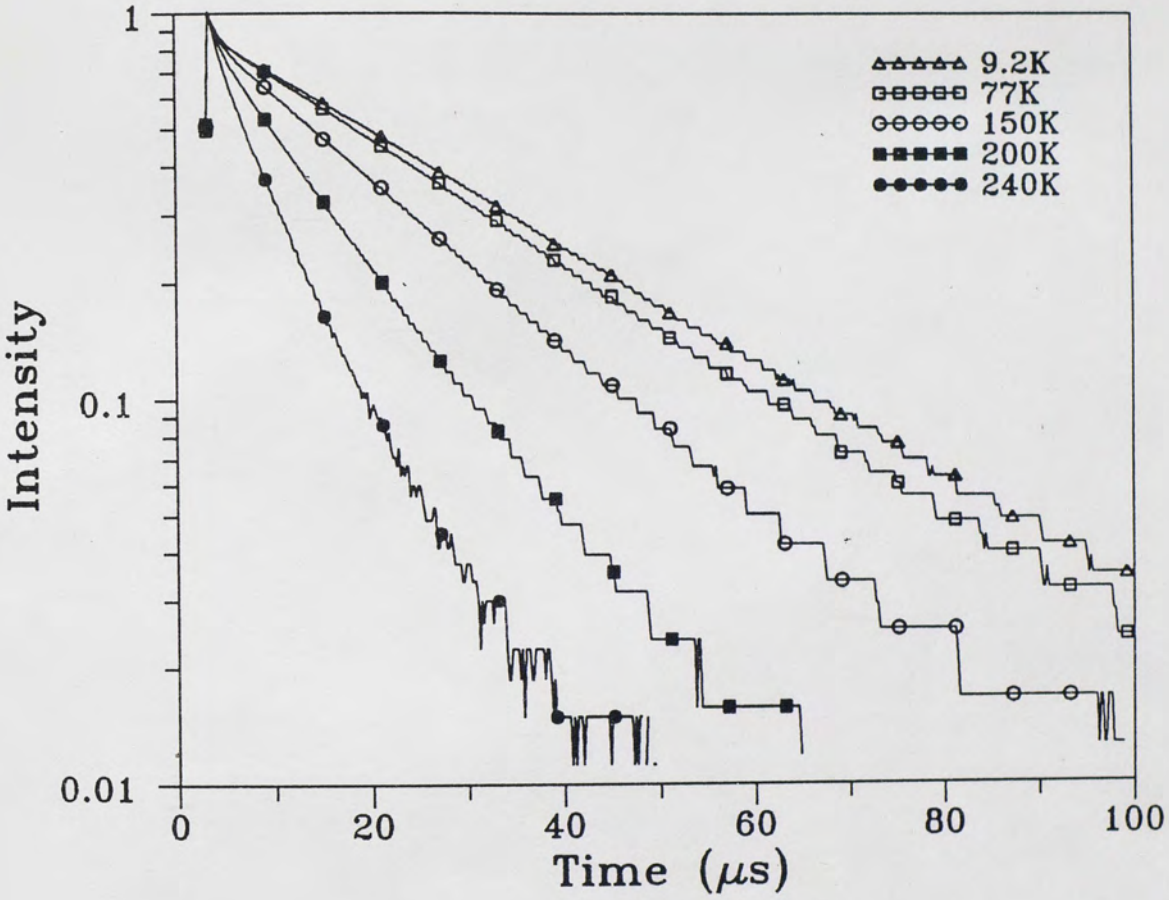

Figure 5(c). Temporal profile of the fluorescence decay of Cr:Mg_2SiO_4 (sample #1) at different temperatures due to 532 nm pumping. The fluorescence was measured at 1200 nm.

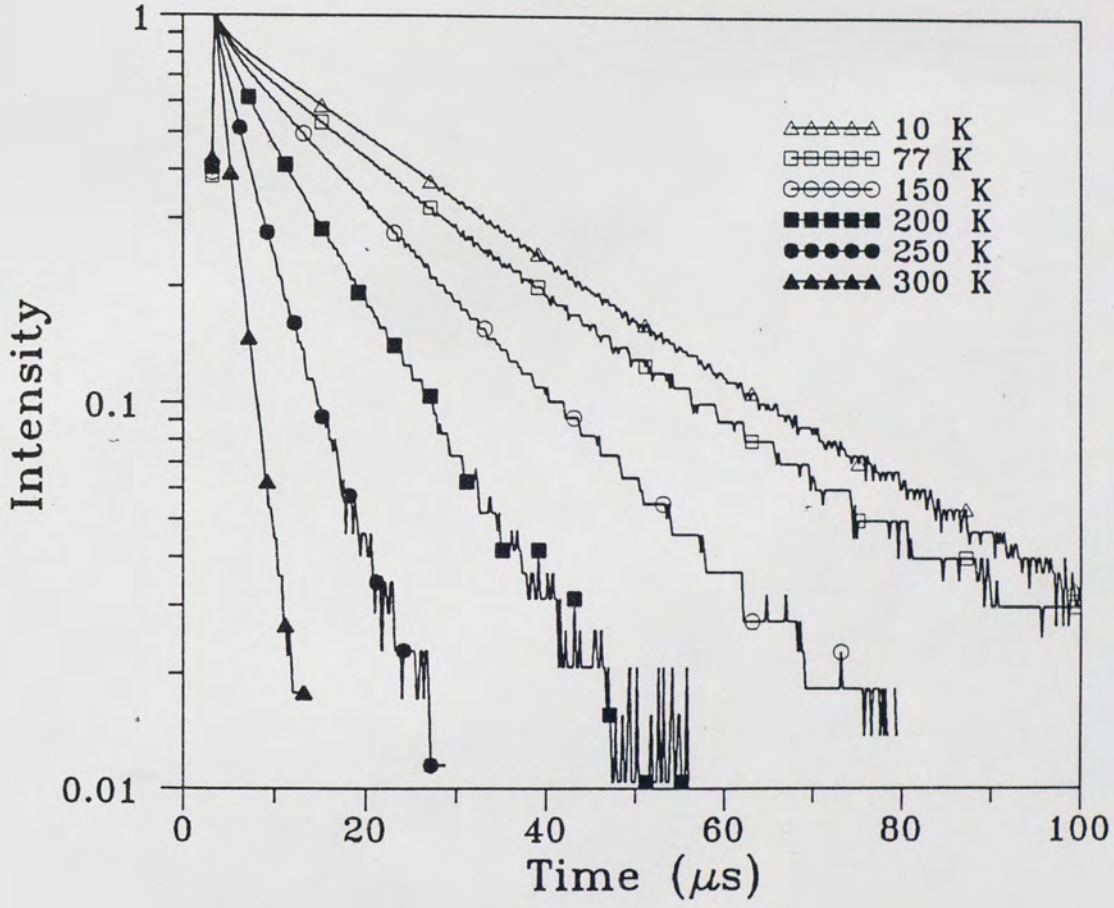

Figure 5(d). Temporal profile of the fluorescence decay of Cr:Mg_2SiO_4 (sample #1) at different temperatures due to 1064 nm pumping. The fluorescence was measured at 1200 nm.

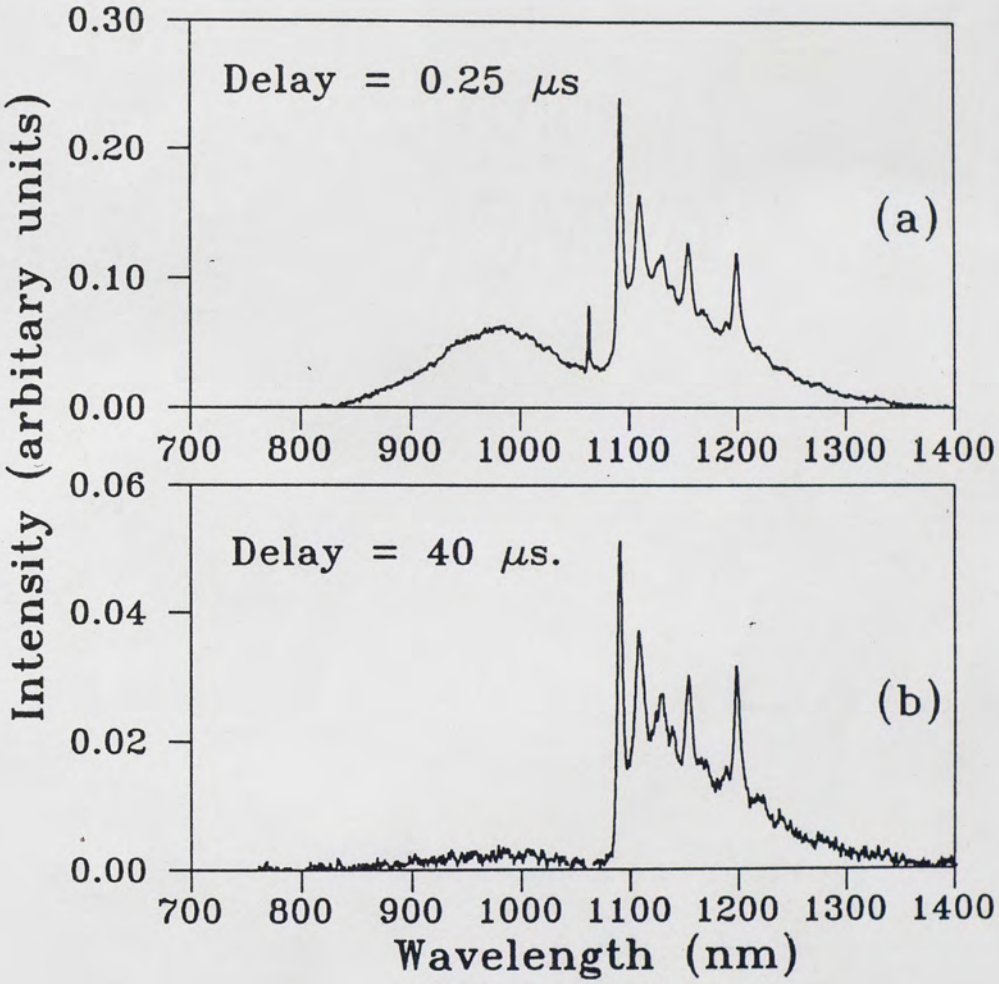

Figure 5(e). Fluorescence spectrum of Cr:Mg_2SiO_4 (sample #1) at 9.76 ^{o}K after a delay of (a) 0.25 μs, and (b) 40 μs from the excitation pulse. The pump wavelength was 532 nm.

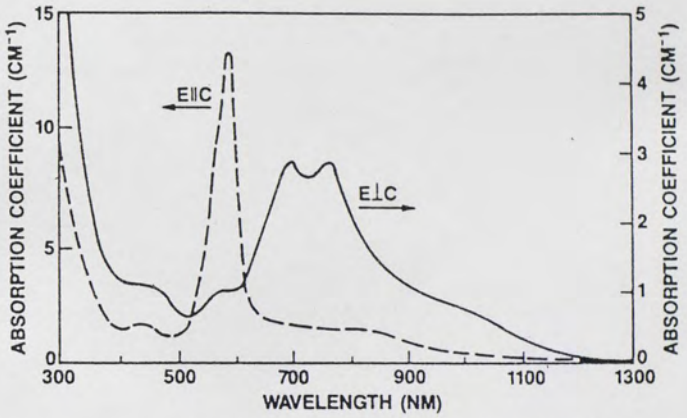

Polarized absorption spectra of 0.5% Cr:CGS. The Cr concentration is 8.9 x 10^{18} cm^{-3}.

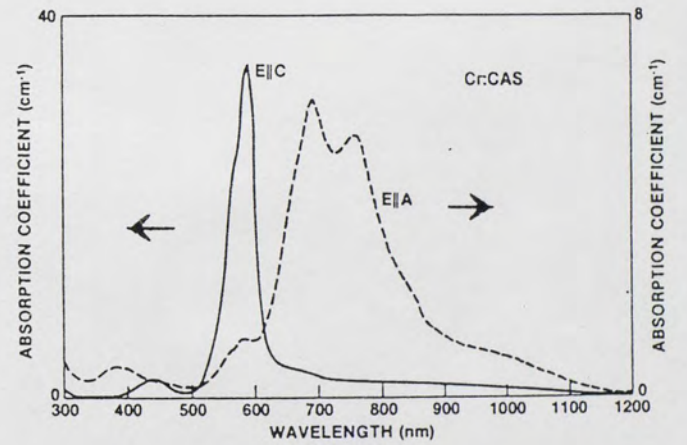

Polarized absorption spectra of 0.2% Cr:CAS. The Cr concentration is approximately 3.7 x 10^{18} cm^{-3}.

Figure 6. Polarized absorption spectra of Cr^{4+}:$Ca_2Ga_2SiO_7$ (upper figure) and Cr^{4+}:$Ca_2Al_2SiO_7$ (lower figure) [Reproduced from Ref. 3.4].

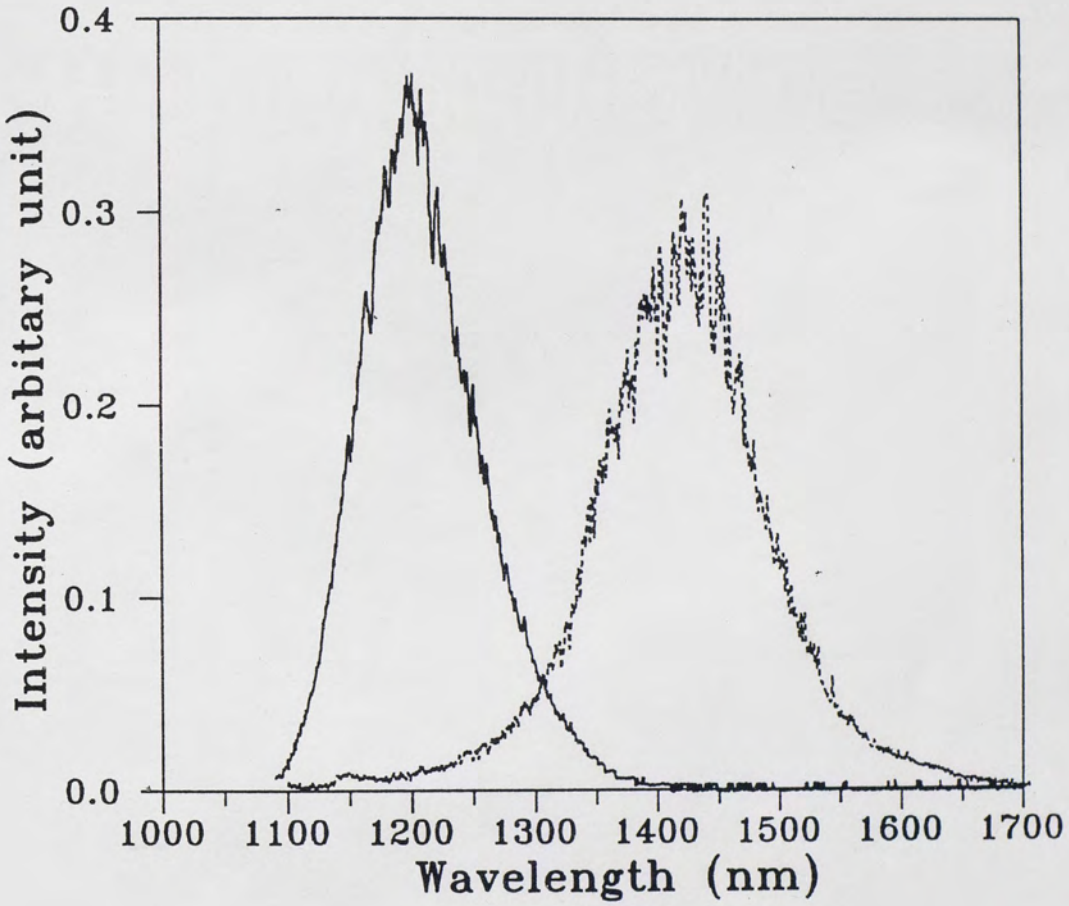

Figure 7. Low temperature fluorescence spectra of Cr^{4+}:$Ca_2Al_2SiO_7$. The band with peak at 1450 nm is due to an unstable center which is annealed after prolonged irradiation with 1064 nm laser radiation.

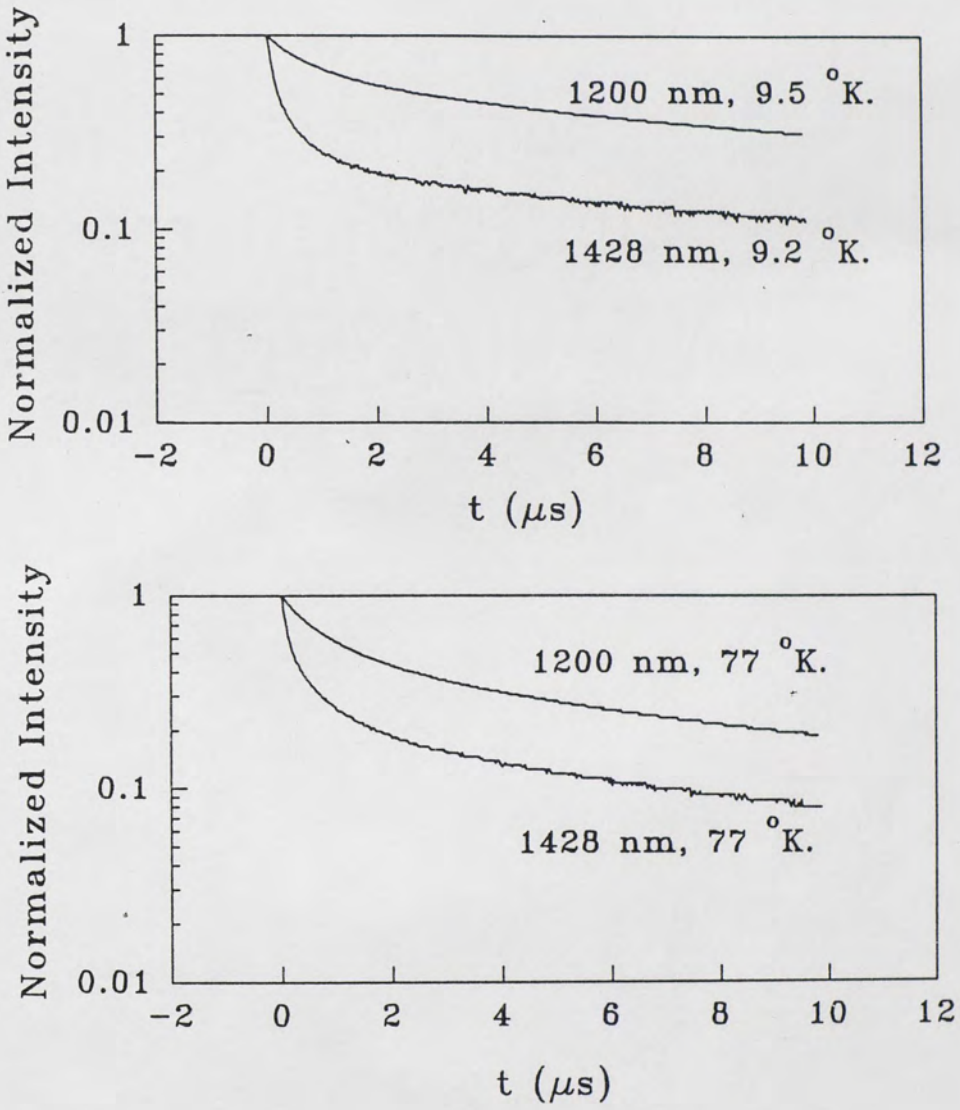

Figure 8(a). Comparison of the temporal profiles of the fluorescence decay of Cr^{4+}:$Ca_2Al_2SiO_7$ at 1200 nm and 1428 nm.

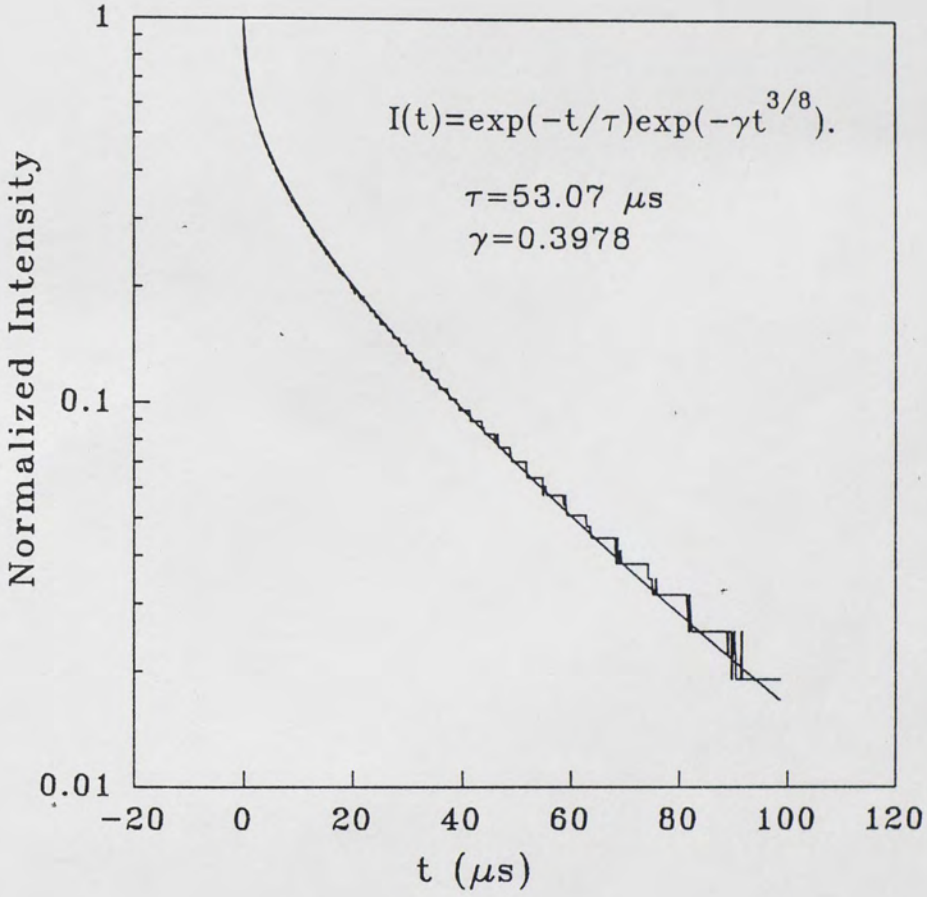

Figure 8(b). Temporal profile of the fluorescence decay of Cr^{4+}:$Ca_2Al_2SiO_7$ measured at 10 °K. The pump wavelength was 1064 nm and fluorescence was measured at 1200 nm. The smooth line is the theoretical fit using Forster-Dexter formula for dipole-quadrupole donor-acceptor energy transfer.

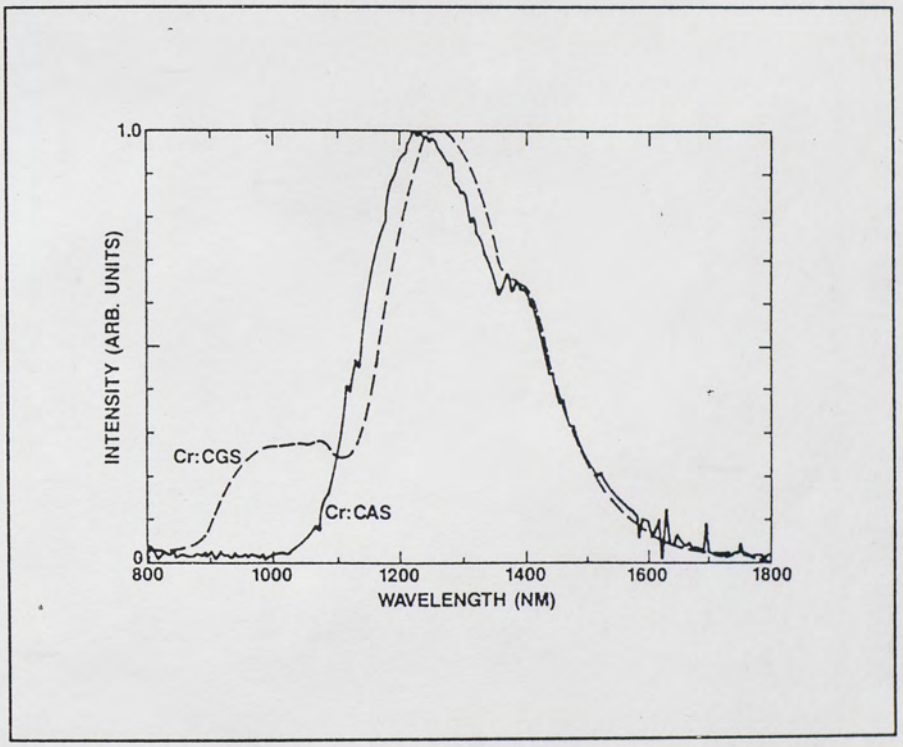

Figure 9. Fluorescence spectrum of Cr^{4+}:$Ca_2Al_2SiO_7$ (Cr:CAS) reproduced from Ref.[3.4] for comparison with Fig. 7.

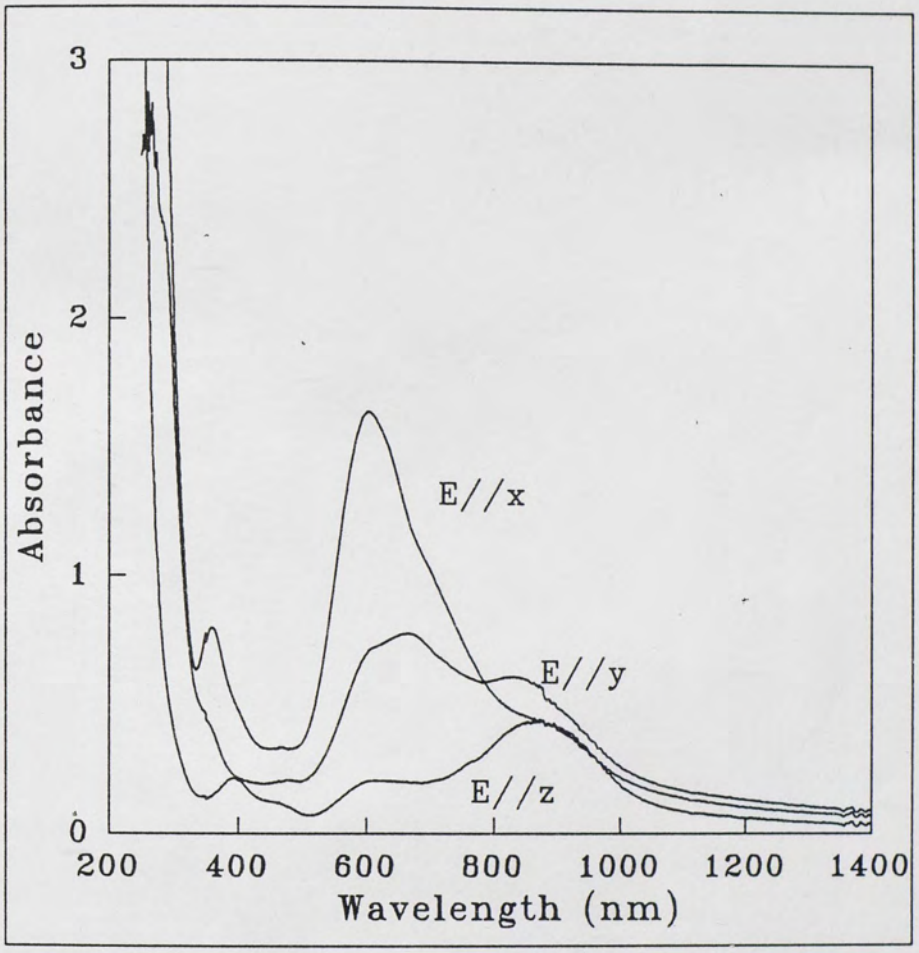

Figure 10. Polarized absorption spectra of Be,Cr:$CaAl_4O_7$ at room temperature.

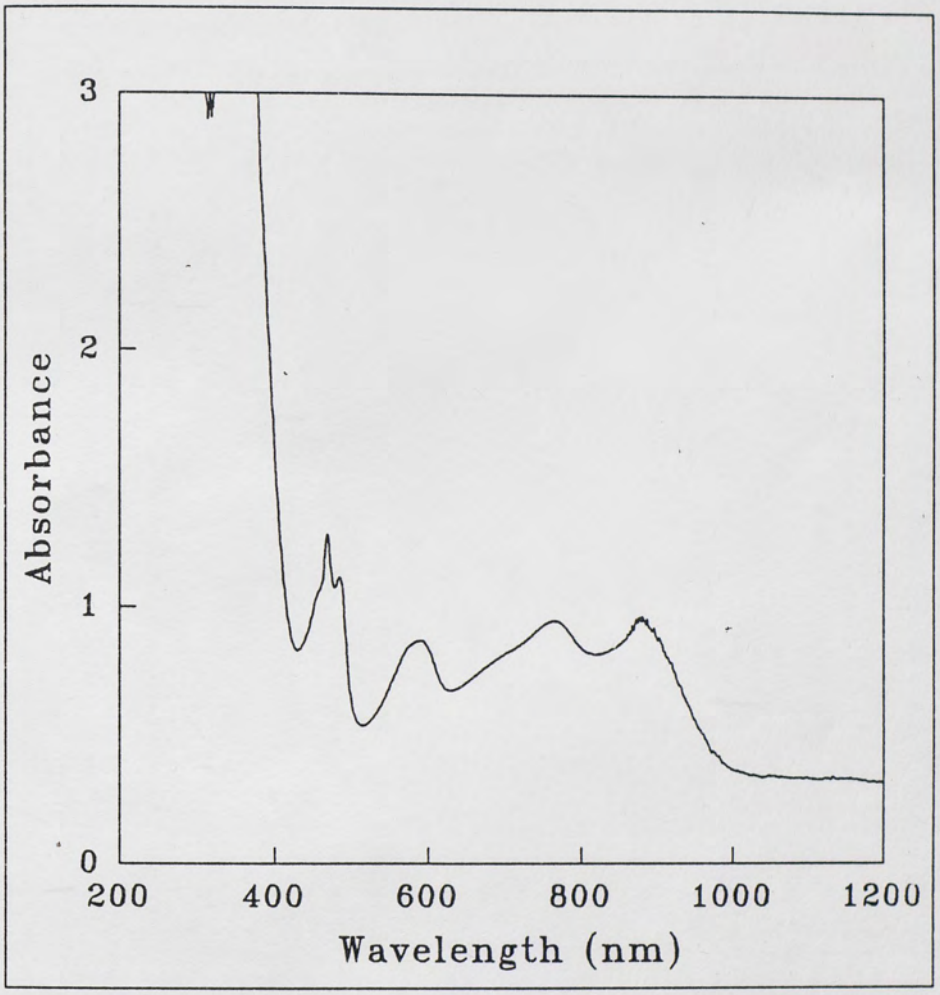

Figure 11. Absorption spectrum of Cr^{4+}:FAP at room temperature.

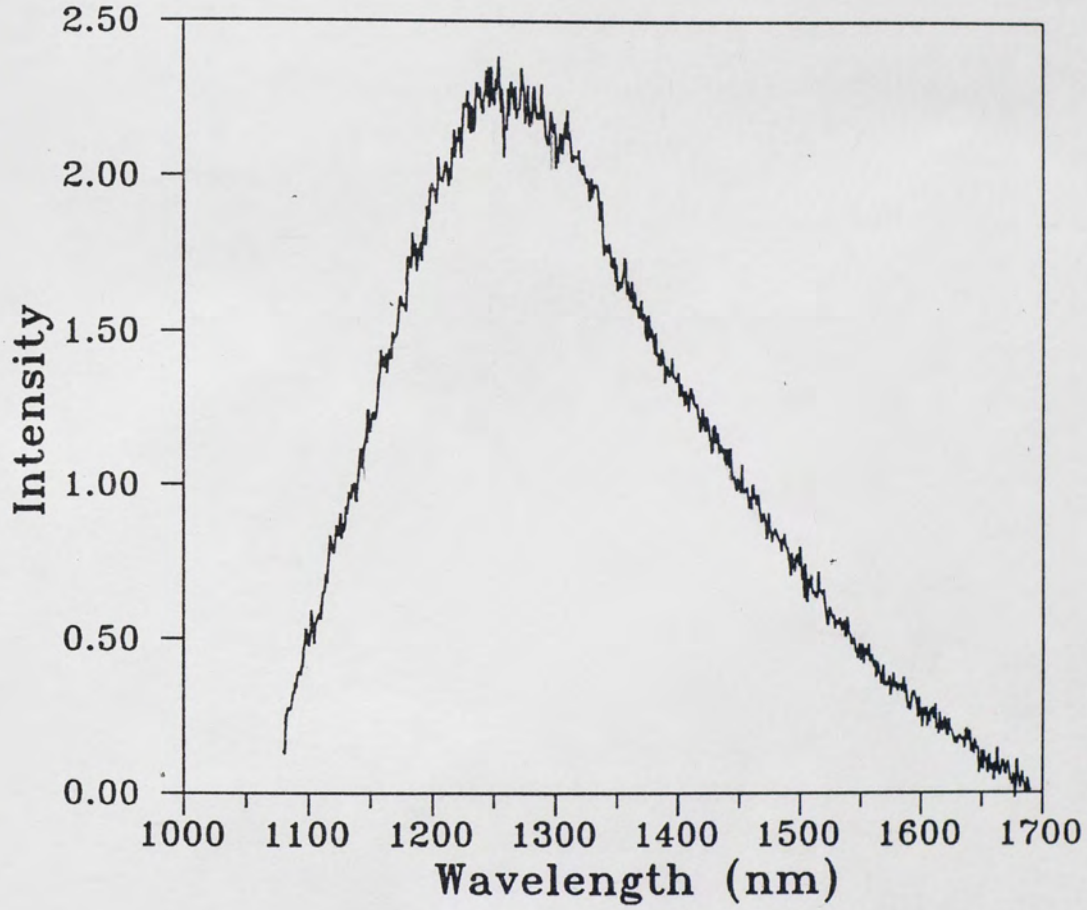

Figure 12. Fluorescence spectrum of Cr^{4+}:FAP at 300 °K; (pump wavelength was 1064 nm).

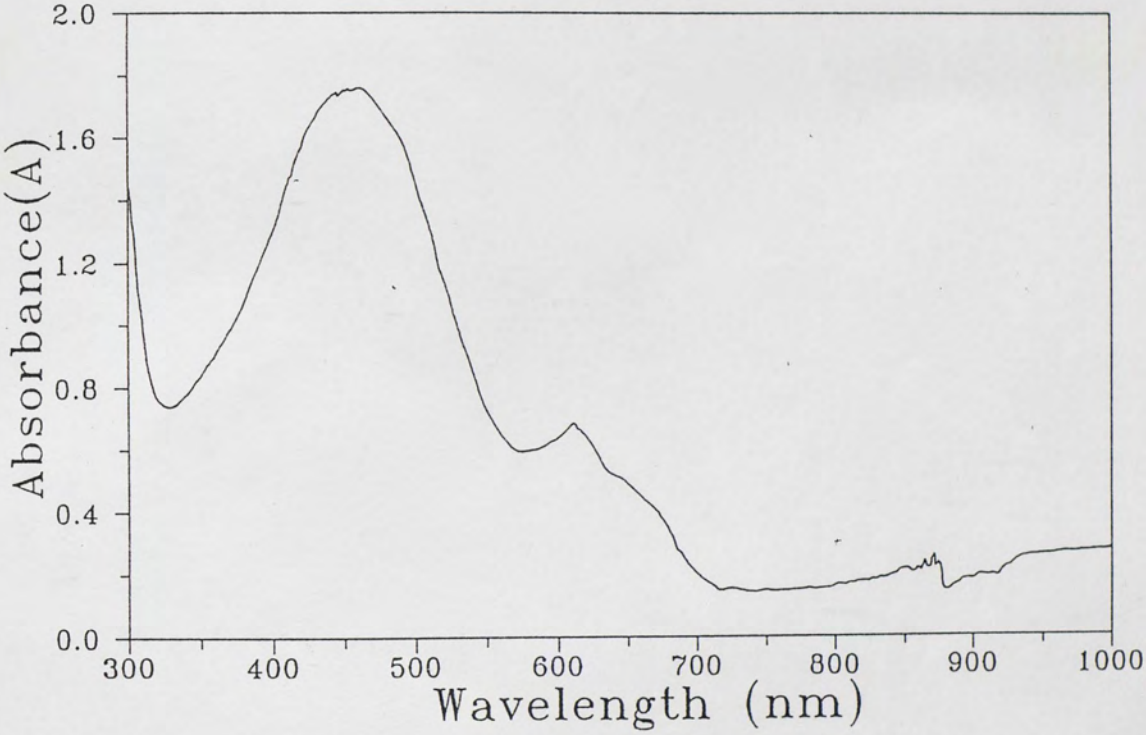

Figure 13. Absorption spectrum of Ca,Cr:YAG at room temperature.

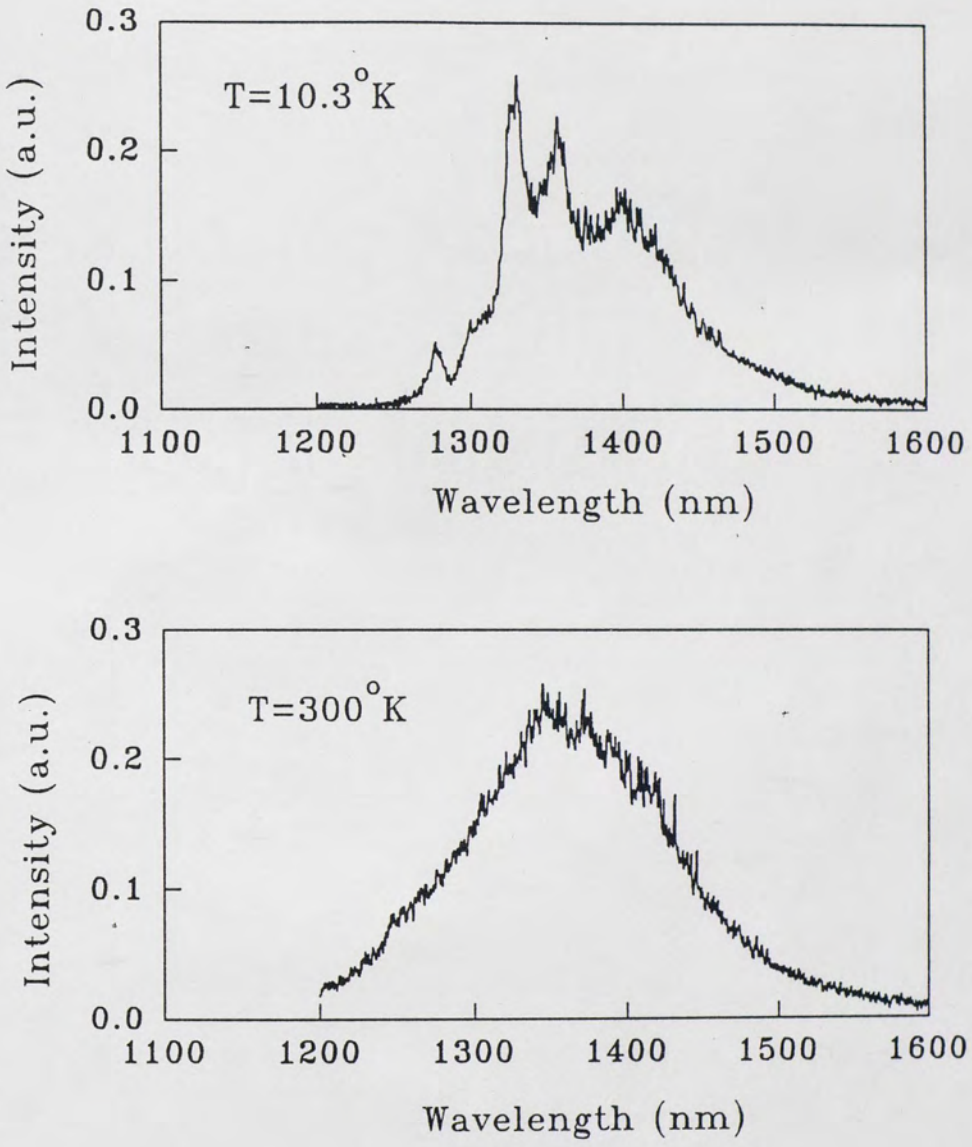

Figure 14. Fluorescence spectrum of Ca,Cr:YAG at 10.3 °K (upper figure) and 300 °K (lower figure).

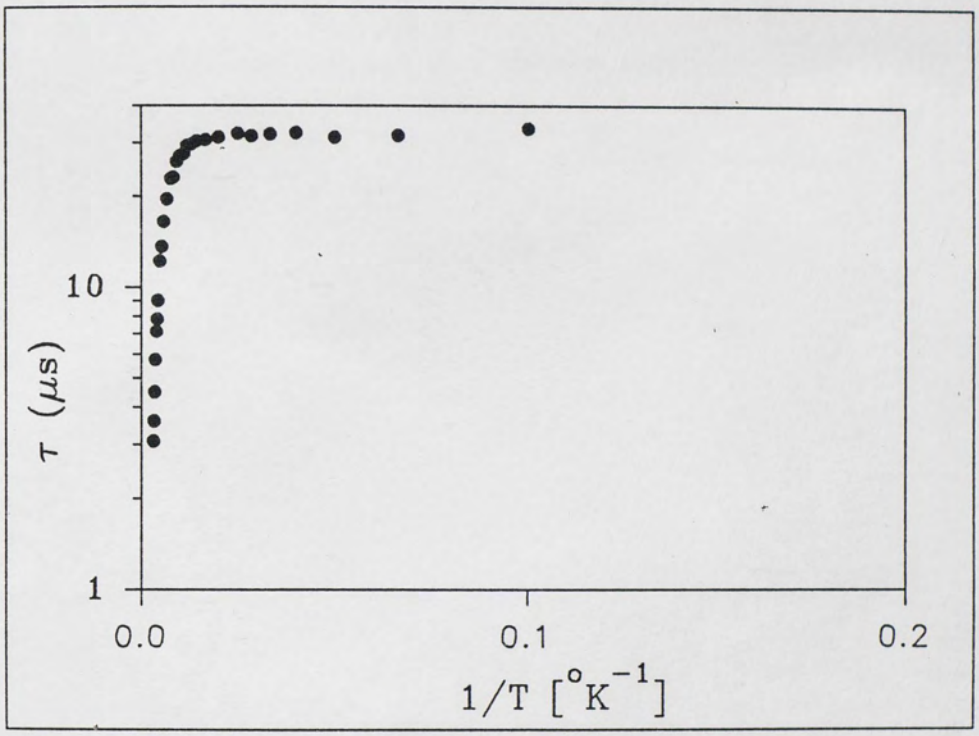

Figure 15. Temperature dependence of fluorescence lifetime of Ca,Cr:YAG.

CHAPTER 4

THEORETICAL SPECTROSCOPY OF INORGANIC CRYSTALS

The study of the optical properties of impurity ions in inorganic crystals requires an understanding of the crystallography of the host, the symmetry of the site occupied by the active ion, the energy levels of the ion in the given host, and the interaction of the active ions amongst themselves, with other centers as well as with the lattice. The symmetry of the site occupied by the active ion determines its energy level structures which can be calculated by the Tanabe-Sugano formalism of crystal field theory. Once the energy levels are known for a given symmetry, the allowed radiative transitions can be identified by using group theoretical techniques. Conversely, it is possible to identify the site symmetry of the active ion by studying the polarization dependence of the absorption and emission spectra in conjunction with the Tanabe-Sugano diagram[4.1] **(Fig.16)** and the symmetry selection rules. In using crystal field analyses to engineer new laser materials efforts are made to control the symmetry of the site occupied by the active ion by proper selection of the host material and introduction of other suitable optically inactive ions into the lattice. Similarly, a proper understanding of the ion-ion and ion-lattice interactions is important because they determine, to a great extent, the potential laser performance of the active ions. Information about these interactions can be extracted from the temporal profile of the fluorescence decay and the absorption and emission band shape characteristics.

It is well known that electron-phonon coupling of transition metal ions in crystals gives rise to broad fluorescence bands, thereby making it possible for the lasers from such systems to be tuned over wide range of wavelengths. But, a very strong

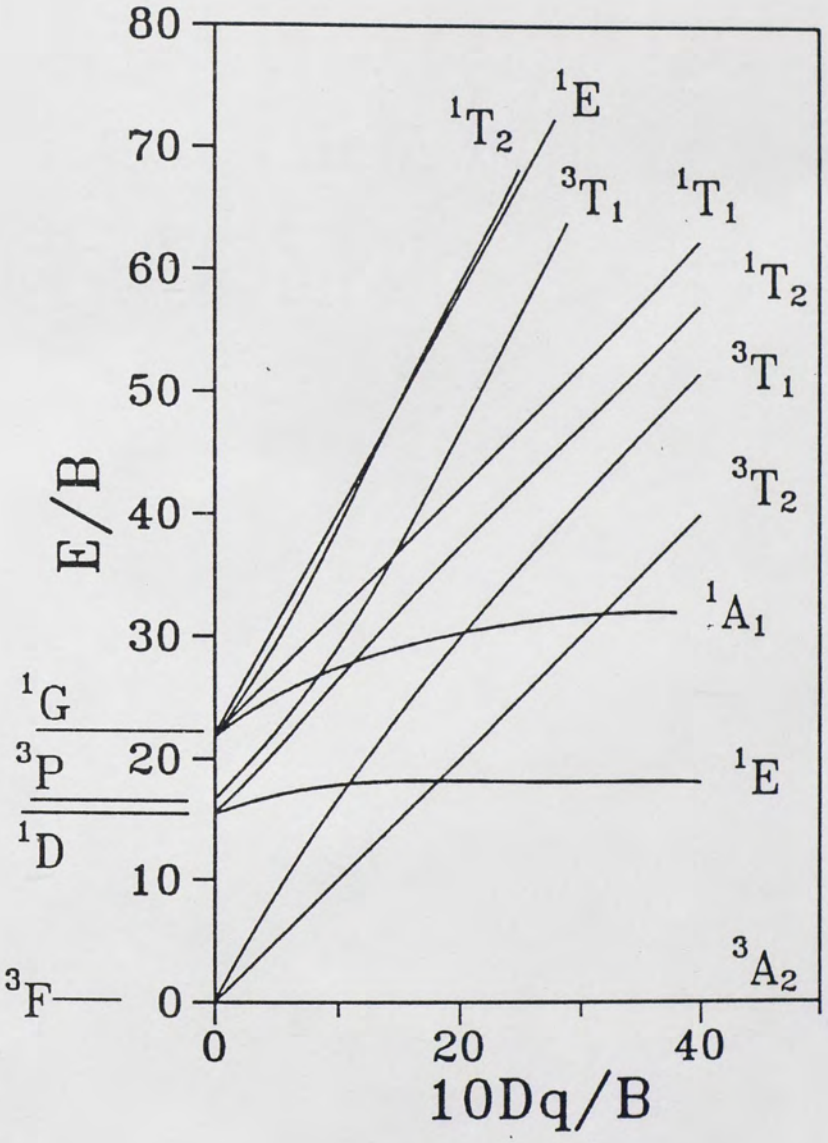

Figure 16. Tanabe-Sugano diagram for Cr^{4+} (d^2) in tetrahedral symmetry.

electron-phonon coupling of the excited state also significantly increases the temperature dependent non-radiative transition rate, thereby quenching the fluorescence intensity at room temperature. This is undesirable from the point of view of laser operation. On the other hand, ion-ion interactions leading to energy transfer between ions, in general, play a negative role in the laser performance of transition mental ions by decreasing the lifetime and intensity of the fluorescence of the active ions. However the same processes may be used to one's advantage in many co-doped systems where efficient energy transfer from one type of ions (sensitizer) to ions of another type (activator) makes it possible to obtain laser action from the activator ions without having to pump them directly. Such systems already exists [4.2]. Ion-ion energy transfer between ions of the same type may also help in upconversion processes by cross-relaxation and has been found to be a very useful mechanism for rare-earth doped systems [4.3].

Brief discussions of each of the above topics are given below in the context of their relevance to the Cr^{4+} ion in the tetrahedral site.

Section 4.1: Symmetry in molecules and crystals

Symmetry of a molecule is characterized by the set of symmetry elements (and the symmetry operations generated by them) it possesses. There are five basic symmetry elements[4.4, 4.5], viz.,

(1) proper rotation axis denoted by C_n which represents an n-fold rotational symmetry about a line (principal axis of rotation);

(2) mirror plane denoted by σ_v, σ_d, and σ_h. σ_v represents a reflection through a mirror plane passing through a principal axis of rotation while σ_h represents a reflection through a mirror plane perpendicular to a principal axis of rotation. Besides, if there are pairs of two-fold proper rotation axes C_2 perpendicular to an n-fold principal rotation

axis, any mirror plane passing through the principal rotation axis and bisecting the angle between pairs of C_2 axes is denoted by σ_d;

(3) improper rotation axis denoted by S_n. It represents an n-fold rotation followed by a reflection through a mirror plane perpendicular to the axis of rotation and passing through the center of the molecule.

(4) inversion center denoted by *i*. It represents the spatial inversion about the center;

(5) identity element denoted by E. It represents the operation that would do nothing to the initial geometrical configuration of the molecule.

Whereas the first four symmetry operations connect *equivalent* configurations of the molecule, the identity operation connects *identical* configurations.

For an individual molecule the set of symmetry elements which completely specify the symmetry associated with it is called the *point group* of that molecule. The elements of this set obey the rules of group theory. In contrast to a molecule, which can be viewed as a closed unit of a finite number of atoms/ions arranged in a definite configuration with respect to an arbitary point (the origin), in a crystal a large number of molecular units are arranged in regular 3-dimensional periodic lattice structures and hence shows both local and extended symmetries. While the local symmetries are described by the various point groups, to describe the extended symmetry of the whole crystal in space one is required to consider also the translational symmetries associated with the lattice in three different directions. Superposition of such translational symmetries in three-dimensions on the point group symmetries defines what is known as the space-group. A space group characterizes the complete structural symmetry of a crystal and hence, from the crystallographic point of view, it is considered the most explicit description of a crystalline structure. However, when one is concerned only with the spectroscopic properties of any given ion in a crystal, it is sufficient to consider

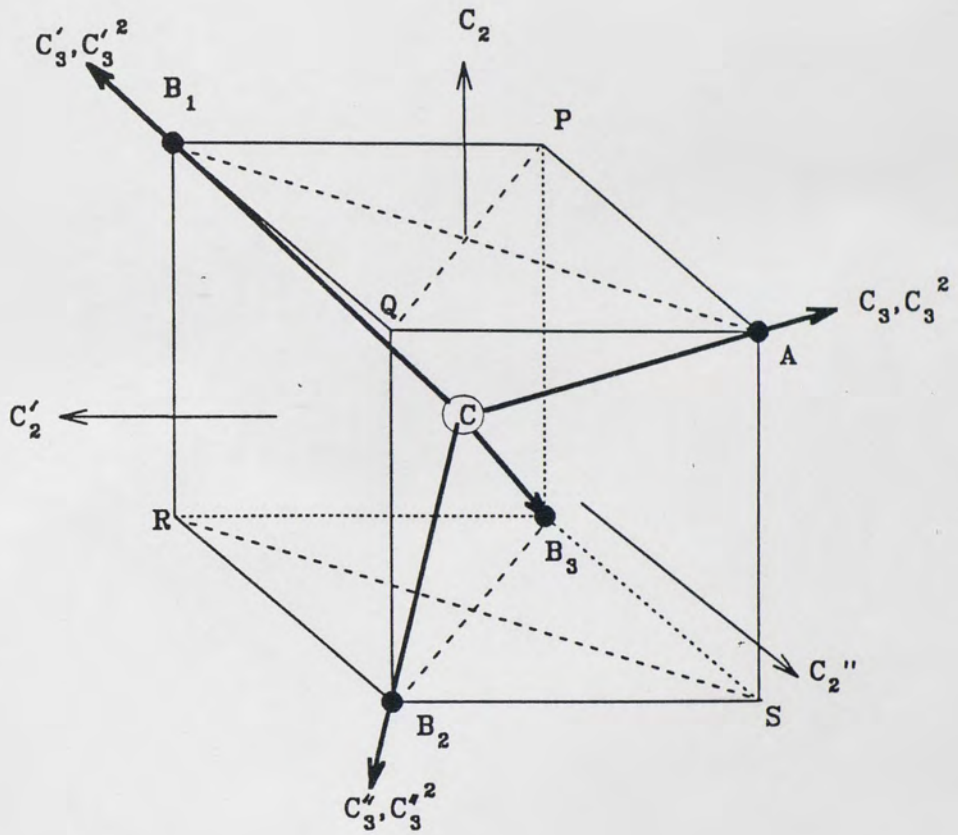

Figure 17. Cr^{4+} ion in an ideal tetrahedral symmetry. The Cr^{4+} ion is located at the center, C, of a cube. There are four ligands located at the vertices A, B_1, B_2 and B_3. The bold arrows show the three-fold rotation axes. The two-fold rotation axes are represented by the thin arrows. Only two of the mirror planes, perpendicular to the face $APQB_1$ and passing through the face diagonals, are shown in this figure.

only the local symmetry of the site occupied by that ion (point group symmetry). This is because such properties are influenced by the surrounding ions only in the immediate neighborhood of the concerned ion. For example, when Cr^{4+} ion is substituted for the Si^{4+} ion in Y_2SiO_5 the spectroscopic properties of the Cr^{4+} ion is determined only by the local tetrahedral crystal fields due to the four nearest neighbor O^{2-} ions; the effects of the more distant neighbors are almost negligible although they might even belong to the same molecular unit. Therefore, in this case the Cr^{4+} ion may be considered as being inside an effectively independent tetrahedral unit formed by four O^{2-} ions and it is the configuration and the resulting symmetry of this tetrahedral unit that determines the spectroscopic properties (such as energy level splitting and selection rules for radiative transitions) of the Cr^{4+} ion. At this stage the space group does not play any significant role.

Since the present work is concerned primarily with Cr^{4+} ions in tetrahedral sites, an introduction to a few configurations with the ideal and distorted tetrahedral symmetries are given below. In the ideal tetrahedral symmetry, the Cr^{4+} ion is situated at the center of a cube with four nearest neighbors (also called ligands) located at four corners of the cube as shown in **Fig. 17**. In all the hosts studied in this work ***the ligands are Oxygen ions***. The symmetry elements corresponding to this configuration which form the point group denoted by T_d are:

(1) four 3-fold proper rotation axes along the four cube diagonals connecting the ligands with the metal ion. They generate eight proper rotational symmetry operations (four C_3 and four C_3^2 rotations);

(2) three 2-fold proper rotation axes C_2 each perpendicular to the opposite faces of the cube and passing through the face-centers;

(3) six mirror planes perpendicular to the cube faces and passing through the face-diagonals;

(4) six 4-fold rotations (parallel to the C_2 axes) each followed by a reflection through a mirror plane perpendicular to the rotational axes and passing through the cube-center.

If one of the vertices A of the tetrahedron is now pulled away from the center of the tetrahedron C along the line AC (joining the center and the vertex) then the resulting distorted tetrahedron loses six of its proper 3-fold symmetry elements, all the improper rotational symmetry elements, all the 2-fold rotational symmetry elements and also three of the mirror planes. The only remaining symmetries are the 3-fold rotations C_3 and C_3^2 about the axis AC and three vertical mirror planes σ_v, σ'_v and σ''_v, containing the axis AC and the diagonal B_1C, B_2C and B_3C respectively. Together with the identity element, these two rotational symmetry elements and the three mirror planes form a lower symmetry point group called C_{3V}. The group multiplication table for this symmetry is given in Table 4.1(a).

TABLE 4.1(a)

GROUP MULTIPLICATION TABLE FOR POINT GROUP C_{3V}

C_{3v}	E	C_3	C_3^2	σ_v	$\sigma_{v'}$	$\sigma_{v''}$
E	E	C_3	C_3^2	σ_v	$\sigma_{v'}$	$\sigma_{v''}$
C_3	C_3	C_3^2	E	$\sigma_{v'}$	$\sigma_{v''}$	σ_v
C_3^2	C_3^2	E	C_3	$\sigma_{v''}$	σ_v	$\sigma_{v'}$
σ_v	σ_v	$\sigma_{v''}$	$\sigma_{v'}$	E	C_3^2	C_3
$\sigma_{v'}$	$\sigma_{v'}$	σ_v	$\sigma_{v''}$	C_3	E	C_3^2
$\sigma_{v''}$	$\sigma_{v''}$	σ_v	$\sigma_{v'}$	C_3^2	C_3	E

If further the length of one of the diagonals B_iC ($i = 1, 2, 3$) is changed, say $B_2C \neq B_1C$, B_3C, AC then all the 3-fold symmetries are broken and only one mirror

plane symmetry, through ACB_2 remains. Together with the identity element E, this mirror plane constitutes one of the lowest point group symmetry in the tetrahedral family. This is called C_s and its group multiplication table is given in Table-4.1(b).

TABLE 4.1(b)

GROUP MULTIPLICATION TABLE FOR POINT GROUP C_s

C_s	E	σ
E	E	σ
σ	σ	E

Section 4.2: Matrix representation of symmetry operations

Each symmetry operation in a point group can be represented by a corresponding matrix which describes the changes brought about by that operation in the configuration space formed by the chosen set of basis functions. The set of representations of all the symmetry operations in a point group follows the same group multiplication table as the symmetry elements in the point group. Such representations depend on the choice of the basis functions, and with the proper choice of the basis set each of the matrices corresponding to the different symmetry operations can be expressed in the block-diagonal form. The block-diagonal sub-matrices, denoted by $\Gamma^{(\nu)}$ ($\nu = 1, 2, 3$), constitute the irreducible representations of the given symmetry operations[4.4]. The *trace* of each such diagonal block is called the *character* of the given operation in the corresponding irreducible representation and is denoted by $\chi_i^{(\nu)}$, where the index i refers to the set of all the symmetry operations C, C′ in the point group that are related by relations of the form $a^{-1}C\,a = C'$ for all the symmetry elements a in the point group. Such a set of operations in a point group are said to belong to the same *Class,* and have the same *character.* Since *trace* of the matrix

representations of a given symmetry operation is invariant under coordinate transformations, the *character* can uniquely characterize the set of all the reducible representations corresponding to that symmetry operation. Also, since any representation of C can be reduced to the block diagonal form and can be expressed as the direct sum of the irreducible representations $\Gamma^{(\nu)}$,

$$\Gamma(C) = \sum_{\nu}^{\oplus} m_{\nu} \Gamma^{(\nu)}(C), \tag{4.1}$$

the trace χ_i of any reducible representation of the operation C can be written as

$$\chi_i = \sum_{\nu} m_{\nu} \chi_i^{(\nu)}, \tag{4.2}$$

where m_{ν} is the number of times the irreducible representation $\Gamma^{(\nu)}$ appears in the final reduced form.

In most literature on spectroscopy special symbols, suggested by R. S. Mulliken [4.4,4.5], are used to designate the irreducible representations. In this notation A and B are used for one dimensional representations depending upon whether a representation is symmetric ($\chi(R) = +1$) or antisymmetric ($\chi(R) = -1$) with respect to the smallest rotation about the principal rotation axis. A subscript of 1 or 2 is used to specify whether the representation is symmetric or antisymmetric with respect to a C_2 axis perpendicular to the principal axis C_n (if such an axis exits) or with respect to a vertical mirror plane σ_v (σ_d). A ′(prime) and ″(double prime) are used to specify respectively the symmetric and antisymmetric nature of an one dimensional representation with respect to the mirror plane σ_h perpendicular to the principal rotation axis. If there is an inversion center in the point group, the symmetric and antisymmetric nature of the one dimensional representation with respect to the inversion center is shown by the subscript *g* and *u* respectively. For two dimensional representations the symbol E is used with subscripts or superscripts assigned to it the same way as

described above. The symbol T is used for three-dimensional representations. The character tables in Mulliken's notations are given below for the point groups T_d, C_{3v} and C_s.

TABLE 4.2(a)

CHARACTER TABLE FOR POINT GROUP T_d

Irreducible representation	Symmetry Elements and Character						
	E	$8C_3$	$3C_2$	$6S_4$	$6\sigma_d$		
A_1	1	1	1	1	1		$x^2 + y^2 + z^2$
A_2	1	1	1	-1	-1		
E	2	-1	2	0	0		
T_1	3	0	-1	1	-1	(R_x, R_y, R_z)	
T_2	3	0	-1	-1	1	(x, y, z)	(xy, xz, yz)

TABLE 4.2(b)

CHARACTER TABLE FOR POINT GROUP C_{3v}

Irreducible representation	Symmetry Elements and Character			
	E	$2C_3$	3σ	
A_1	1	1	1	$z, x^2 + y^2, z^2$
A_2	1	1	-1	R_z
E	2	-1	0	$(x, y), (R_x, R_y),$ $(xz, yz), (x^2-y^2, xy)$

TABLE 4.2(c)

CHARACTER TABLE FOR POINT GROUP C_s

Irreducible representation	Symmetry Elements and Character			
	E	σ_h		
A′	1	1	(x, y), R_z	x^2, y^2, z^2, xy
A″	1	-1	z, (R_x, R_y)	(xz, yz)

The functions on the right hand columns in the above tables 4.2(a) through 4.2(c) have the same character systems as the representation in the corresponding rows and therefore transform in the same manner as those representations.

Section 4.3: Energy levels of ions in crystal

The energy levels of a free ion can be obtained by solving the Schroedinger equation for the many electron system. Taking into consideration only the electrons in the outermost shells which are not closed the Hamiltonian for such a system can be expressed as:

$$\mathcal{H} = \Sigma[\, p_i^2/2m - Ze^2/4 + e(r_i)\, l_i .s_i \,] + \Sigma\, e^2/4\pi\varepsilon_o r_{ij} \qquad (4.3)$$

where the summations i, j are over the outer electrons (outside the closed shell). For Cr^{4+} the electron configuration is $1s^2\, 2s^2\, 2p^6\, 3s^2\, 3p^6\, 3d^2$ so that all the shells except the 3d are closed. Therefore, for the purpose of energy level calculations it can be regarded essentially as a two-electron system ($3d^2$). The optical transitions in this ion involve only the two outer 3d electrons while the rest form a stable core and do not actively participate in such processes[4.6, 4.7].

To avoid computational complications the electron-electron interaction term is usually replaced by a sum of spherically-averaged potential energy terms in the central-field approximation[4.7]. The Hamiltonian is then written as:

$$\mathcal{H} = \sum[\, p_i^2/2m - Ze^2/4\pi\varepsilon_o r_i + e(r_i)\, l_i .s_i\,] + \sum \mathcal{U}_i\,(r_i)\,. \qquad (4.4)$$

The free ion states are characterized by the quantum numbers L, S, J and M_J which are the total orbital angular, spin, total angular and total magnetic angular momentum quantum numbers respectively. Again, for Cr^{4+} the possible values of L are 0, 1, 2, 3 and 4 (corresponding notations for the orbital states are S, P, D, F and G respectively) while S = 0 or 1(corresponding spin states have multiplicity of 1 or 3 and hence are referred to as singlet or triplet states). For given values of L and S the total angular momentum quantum numbers are given by the angular momenta addition rules for the vector sum of $\vec{L}+\vec{S}$.

When the ion is placed in a crystalline site, it will experience additional electrostatic forces due to the surrounding ions of the host. This requires additional interaction terms to be included in the Hamiltonian for the system so that the total Hamiltonian becomes:

$$H_{total} = \mathcal{H} + \mathcal{H}_c(\, r_i\,, \mathbf{R}_k\,), \qquad (4.5)$$

where the last term is the interaction energy of the electrons in the ion and the neighboring ions (also referred to as ligands). It is a function of the positions of the electrons in the central ion ($\mathbf{r}_i$) and the ligands ($\mathbf{R}_k$). The ligands are taken as point charges for the simplicity of calculations. The crystal field splits the free-ion energy levels into a number of crystal field components. The manner in which such splitting occur depends upon the site symmetry and the strength of the crystal field. Usually only the influence of the nearest neighbors are taken into account in determining this term. For example, for the Cr^{4+} ion substituted for the Si^{4+} in the $(SiO_4)^{4-}$ tetrahedron in

Mg_2SiO_4 it is sufficient to consider the crystal field at the Cr^{4+} site due to only the O^{2-} ions which are at the vertices of the $(CrO_4)^{4-}$ tetrahedron.

For weak crystal fields the free ion eigenstates $|\gamma\ LSJM_J>$ are valid and the effect of the crystal field can be calculated as a perturbation using these as the basis functions. However, if the crystal field is not insignificant in comparison to the inter-electronic repulsion, for a more general calculation for the energy levels it is necessary to form the basis functions of symmetry adapted linear combinations of the atomic d-orbitals.

Tanabe and Sugano **[4.8]** in 1954 presented the first general formalism for the calculation of the energy levels of ions in different symmetry environments in terms of the crystal field parameters. For the d^2 electron configuration in tetrahedral symmetry, the first few energy levels are given in terms of the Racah-parameters A, B, C and the crystal field parameter Dq as **[4.4]**:

$$U(^3A_2) = -12\ Dq \tag{4.6a}$$

$$U(^1E) = -12Dq + 8B + 2C - 6B^2/(10Dq) \tag{4.6b}$$

$$U(^1A_1) = -12Dq + 16B + 4C - 108B^2/(10Dq) \tag{4.6c}$$

$$U(^3T_2) = -2Dq \tag{4.6d}$$

$$U(^3T_1(^3F)) = 3Dq + 7.5B - 1/2\ [\ 225B^2 + 100(Dq)^2 - 180DqB\ ]^{1/2} \tag{4.6e}$$

$$U(^3T_1(^3P)) = 3Dq + 7.5B + 1/2\ [\ 225B^2 + 100(Dq)^2 - 180DqB\ ]^{1/2} \tag{4.6f}$$

$$U(^1T_2) = -2Dq + 8B + 2C - 12B^2/(10Dq) \tag{4.6g}$$

$$U(^1T_1) = -2Dq + 12B + 2C \tag{4.6h}$$

The graphical representation of the above energy levels as funtions of crystal field parameters in the tetrahedral symmetry are given in **Fig.16**.

For the purpose of characterization of any given crystal in tetrahedral symmetry it is necessary to compare the observed polarized absorption spectra with those calculated from the Tanabe-Sugano formulae. Any observed dichorism in the absorption spectra would indicate that the symmetry of the system is actually lower than ideal tetrahedral. It is possible, by studying the crystallographic parameters and using group theoretical techniques, to determine the actual symmetry of the system and identify all the polarization dependent bands both in the absorption and the emission spectra.

Section 4.4: Selection Rules

In the spectroscopy of ions in crystals there are three important selection rules for radiative transitions. They are:

(i) Parity selection rule: Let $\Psi_i(\mathbf{r})$ and $\Psi_f(\mathbf{r})$ be the initial and the final states and let V(r) be the interaction Hamiltonian responsible for a transition from between these two states. The matrix element for this process is $<\Psi_f(\mathbf{r})|V(r)|\Psi_i(\mathbf{r})>$. Under space inversion, the value of this matrix element must remain invariant, i.e.

$$< \Psi_f(-\mathbf{r}) \,|V(-r)|\Psi_i(-\mathbf{r}) > \; = \; < \Psi_f(\mathbf{r}) \,|V(r)|\Psi_i(\mathbf{r}) >. \qquad (4.7)$$

If $\Psi_f(\mathbf{r})$ and $\Psi_i(\mathbf{r})$ have the same parity and V(r) has odd parity the above relation becomes

$$-< \Psi_f(\mathbf{r}) \,|V(r)|\Psi_i(\mathbf{r}) > \; = \; < \Psi_f(\mathbf{r}) \,|V(r)|\Psi_i(\mathbf{r}) >, \qquad (4.8)$$

which gives

$$< \Psi_f(\mathbf{r}) \,|V(r)|\Psi_i(\mathbf{r}) > \; = \; 0. \qquad (4.9)$$

Thus, the transition probability, which is proportional to $|<\Psi_f(\mathbf{r})\,|V(r)|\,\Psi_i(\mathbf{r})>|^2$ vanishes. The electric dipole interaction Hamiltonian is proportional to $\mathbf{er}.\alpha$, where α

is the unit vector along the direction of polarization of the incident electromagnetic radiation (in case of absorption) or the polarization of the emitted radiation (emission). The parity of this interaction is odd. Therefore, *the electric dipole transition between states with same parity is forbidden.*

For the $(3d)^n$ configuration in transition metal ions the parity of the electronic wave functions is even and therefore the electric dipole radiative transition between the purely electronic states of these ions are forbidden. However, magnetic dipole transitions are allowed since they involve matrix elements such as $<\Psi_f(\mathbf{r})|\, yz\, |\Psi_i(\mathbf{r})>$ and the parity of yz is positive.

(ii) Spin selection rule: This states that the transition between states of different spin multiplicity is forbidden. For allowed transitions one must have $\Delta S = 0$, where S is the total spin quantum number. This is a very strong selection rule for free ions, but can be violated in condensed matter.

(iii) Symmetry selection rule: This states that radiative transition between two given states is allowed only if the direct product of the irreducible representations corresponding to the electromagnetic interaction Hamiltonian and the initial state (an upper level/excited state for emission or a lower level/ground state for an absorption) contains the irreducible representation corresponding to the final state. Thus if the initial and the final states belong to the irreducible representations Γ and Γ'' respectively and the interaction Hamiltonian H_{int} belong to the irreducible representation Γ' then the matrix element

$$< \Psi_f(\Gamma'')\, |H_{int}(\Gamma')|\Psi_i(\Gamma) > \; = \; 0, \qquad (4.10)$$

unless $\Gamma' \otimes \Gamma$ contains Γ''. This rule plays a very important role in the emission and absorption properties of ions in crystals.

One of the most desired properties of a laser crystal is a strong fluorescence intensity. This is possible only if the electric dipole transition probability is significantly higher compared to probabilities for the non-radiative decay from the excited state to the ground state. The question is how to increase the electric dipole transition rate? In crystalline materials, this has been made possible by (a) lowering the symmetry at the site of the active ion, and (b) vibration coupling of the electronic states[4.9]. The first is directly related to the crystal field splitting of energy levels in lower symmetry and the symmetry selection rules for the new crystal field components. This is discussed later in more detail in relation to the analysis of the absorption spectra in Chapter-5. The vibration coupling is very important not only from the point of view of selection rules (it makes electric dipole transitions between forbidden electronic states possible) but also for the tunability of solid state laser. A brief discussion on this subject is given below with particular emphasis on the basic points necessary to be considered for the evaluation of the potential laser performance properties of any given crystal.

Section 4.5: Vibrations in crystals

The active ions in a crystal lattice are subject to the vibrations of the lattice and a treatment of the dynamics of a such ions must include the effects of this vibrating lattice. The vibrational motion is best described in terms of the normal coordinates Q_k of the lattice[4.7]. For practical purposes, it is convenient to treat the vibrating environment around the active ion in terms of a single configuration coordinate Q which is defined as the distance between the active ion and its nearest neighbors as they pulsate around the active ion. The ion plus lattice states are then expressed in terms of the product of an electronic state $\Psi_a(\mathbf{r}_i, Q_o^{(a)})$ and a vibrational wave function $\chi_a(Q)$, where $Q_o^{(a)}$ is the average value of Q when the active ion is in the electronic state 'a'.

The energy of the resultant state is expressed in terms of the electronic energy plus the potential energy due to the electron-lattice coupling in the vibrating lattice. Under the harmonic oscillator potential approximation the energy of the ion is then given by

$$E^{(a)}(Q) = E_o^{(a)}(Q_o^{(a)}) + V^{(a)}(Q), \tag{4.11}$$

where

$$V^{(a)}(Q) = (1/2)\, M\omega^2 (Q_o^{(a)} - Q)^2. \tag{4.12}$$

Here M is the effective mass of the ion in the lattice and ω is the angular frequency of vibration. In general ω may be different in different electronic states. The potential energy diagram is then given by a parabola with a minimum at $(Q_o^{(a)}, E_o^{(a)})$, where $E_o^{(a)}$ is the electronic energy of the ion in the rigid lattice. The electro-vibronic states for this system can be written under Born-Oppenheimer approximation[4.10] as $\Psi_a(\mathbf{r}_i, Q_o^{(a)})\, \chi_a(Q)$.

A quantum mechanical treatment of the problem in the harmonic oscillator approximation gives the vibrational potential energy in the state 'a' in terms of the number of phonons $<n_u>$,

$$V^{(a)}(Q_o^{(a)}) = \frac{1}{2}\hbar\omega\,[< n_u > + \frac{1}{2}] \tag{4.13}$$

The average value of n_u at temperature T is given by

$$< n_u >= [\exp(\frac{u\hbar\omega}{KT}) - 1]^{-1}. \tag{4.14}$$

In that case the electro-vibronic states in a certain electronic state are represented by horizontal lines in the parabolic configuration coordinate diagram for that state **[Fig.18]**. At this point it is important to note that for electronic states corresponding to different electron configuration in the active ion the equilibrium value of Q is, in general, different because of the different possible electron-lattice coupling.

Therefore, an excited state 'b' may have a parabola diagram whose minimum is at $(Q_o^{(b)}, E_o^{(b)})$ with $Q_o^{(a)} \neq Q_o^{(b)}$ as shown in **Fig.18**. The vibrational energy levels in this state may be represented by parallel lines in this parabola, the position of each line above the zero point energy being given by

$$V^{(b)}(Q_o^{(b)}) = \frac{1}{2}\hbar\omega'[< m > + \frac{1}{2}]. \qquad (4.15)$$

Here we have used ω' instead of ω to emphasize the point that the vibrational frequency may be different for different electronic states.

The difference in the electron-lattice coupling in two electronic states 'a' and 'b' is reflected in the difference between the values of $Q_o^{(b)}$ and $Q_o^{(a)}$ and is characterized by the Huang-Rhys parameter defined as

$$S = \frac{1}{2\hbar\omega} M\,\omega^2 (Q_0^{(b)} - Q_0^{(a)})^2 \qquad (4.16)$$

$$= \frac{1}{\hbar\omega}(E_{ab} - E_{zp}) \qquad (4.17)$$

where, E_{ab} = energy of the peak of the absorption band due to the transition from state 'a' to 'b', and

E_{zp} = energy difference between the zero phonon levels in the above two states.

Section 4.6: Shape of absorption and emission bands

Absorption of energy excites the ion from the zero point vibrational level in the ground state 'a' to a vibrational level in the higher electronic state 'b'. Because of the availability of large number of electro-vibronic levels in the state 'b' the absorption, in general, is expected to be a broad band.

The transition probability between the electro-vibronic levels (a, u) and (b, v) is proportional to $|<\Psi_a(Q_o^{(a)})\,\chi_a(u,Q)\,|\,\mu\,|\Psi_b(Q_o^{(b)})\,\chi_b(v,Q)>|^2$. According to Frank-Condon principle, the change in the electronic motion takes place much faster than any

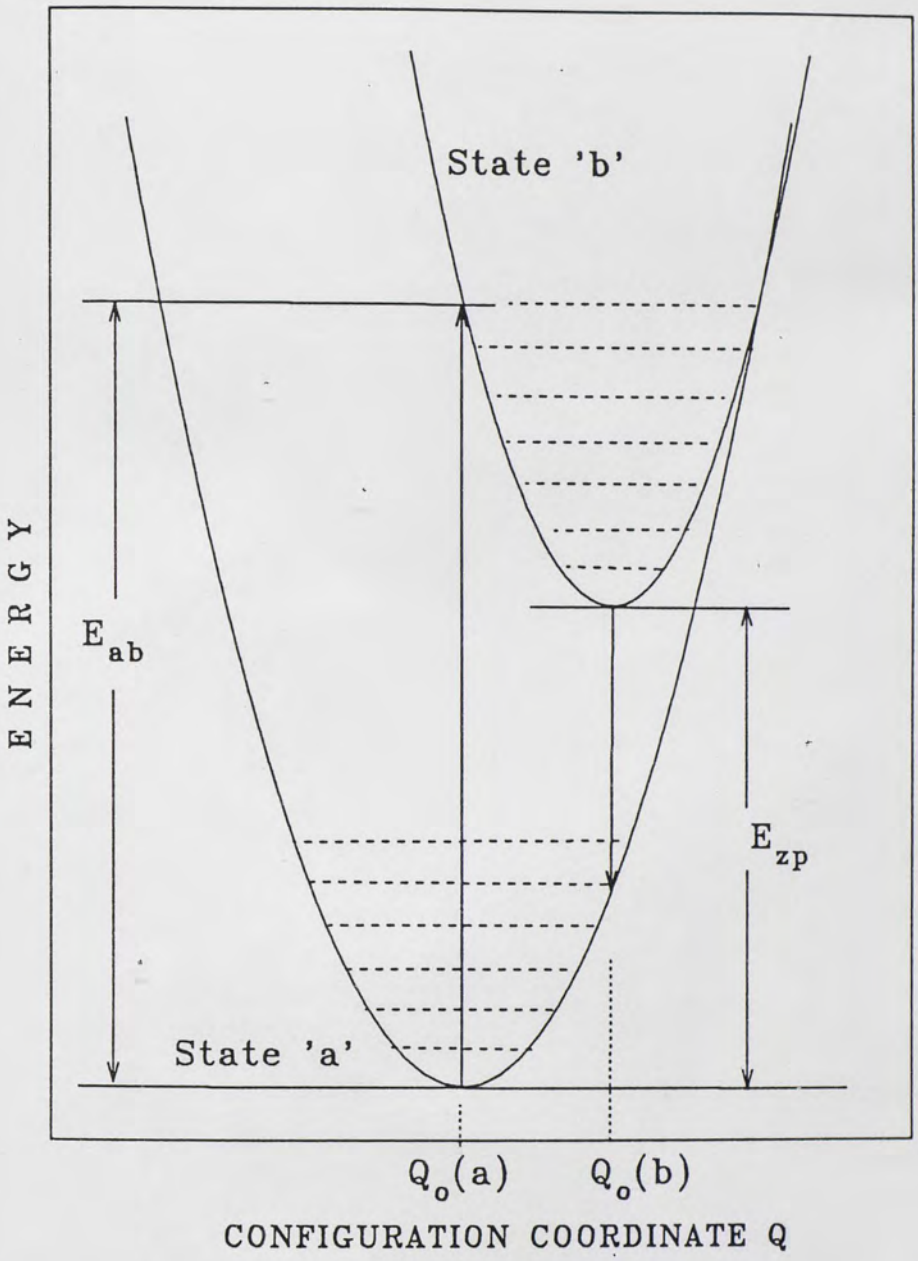

Figure 18. Schematic configurational coordinate diagram for electronic states 'a' and 'b'. The peak of the absorption energy is represented by the vertical line joining the bottom of the ground state parabola to the point of intersection with the excited state parabola. The peak of the emission energy is represented by the vertical line joining the bottom of the excited state parabola to the point of intersection with the ground state parabola. The dashed horizontal lines represent the vibrational energy levels.

change in ionic motion. Therefore the transition from 'a' to 'b' will initially take place most favorably between the states $\Psi_a(\mathbf{r}_i, Q_o^{(a)})\,\chi_a(0,Q_o^{(a)})$ and $\Psi_b(\mathbf{r}_i, Q_o^{(a)})\,\chi_b(v,Q_o^{(a)})$ where m is the vibrational level in the state 'b' which corresponds to a potential energy above the zero point level of that state given by,

$$V^{(b)}(Q) = (1/2)\, M\omega'^2\, (Q_o^{(b)} - Q_o^{(a)})^2. \tag{4.18}$$

In general the transition probability from (a,u) to (b,v), under Frank-Condon principle, will be

$$\begin{aligned} W_{au,bv} &= |\langle \Psi_a(Q_o^{(a)}) \,|\, \mu \,|\Psi_b(Q_o^{(a)})\rangle|^2 \; |\langle \chi_a(u,Q) \,|\, \chi_b(v,Q)\rangle|^2 \\ &= P_{ab}\, |\langle \chi_a(u,Q) \,|\, \chi_b(v,Q)\rangle|^2. \end{aligned} \tag{4.19}$$

where P_{ab} is the purely electronic transition probability $|\langle \Psi_a(Q_o^{(a)}) \,|\mu|\, \Psi_b(Q_o^{(a)})\rangle|^2$

Keil [4.11] used the above principle to show that the shape of the absorption band is given by

$$I_{ab}(E) = I_o\, Avg_u \sum_v |\langle \chi_a(u) \,|\, \chi_b(v)\rangle|^2\, \delta(E_{bv} - E_{au} - E) \tag{4.20}$$

where Avg_u means the average over initial vibrational levels u; the summation is over the final vibrational levels v. At T = 0 ^oK, this can be expressed as:

$$I_{ab}(E) = I_o \sum_{v=0}^{\infty} \frac{S^v e^{-S}}{v!}\, \delta(E_{b,v} - E_{a,o} - E) \tag{4.21a}$$

which can be written as

$$I_{ab}(E) = I_o \sum_{v=0}^{\infty} \frac{S^v e^{-S}}{v!}\, \delta(p\hbar\omega + E_{zp} - E), \tag{4.21b}$$

where E_{zp} is the energy difference between the zero point energy levels of the states 'a' and 'b'.

At T > 0 ^oK,

$$I_{ab}(E) = I_o \sum_{p=-\infty}^{\infty} \left(\frac{n+1}{n}\right)^{p/2} e^{-S(1+2n)}\, I_p[2S\sqrt{n(n+1)}]\; \delta(p\hbar\omega + E_{zp} - E) \tag{4.22}$$

where I_p is the modified Bessel function of the order p, S is the Huang-Rhys parameter and n is given by

$$n = [\exp(\frac{\hbar\omega}{KT}) - 1]^{-1}. \quad (4.23)$$

Eqs.(4.21) and (4.22) give the absorption spectra as a series of sharp lines equally spaced by $\hbar\omega$. In reality, however, each of these lines have of finite width due to homogeneous (and also possibly inhomogeneous) broadening. Also, there may be multiple frequency modes in the lattice. As a result the observed spectrum appears as a broad band. Depending on the resolution of the spectrometer and the system under study, at low temperatures the phonon band structures may or may not be resolved. In general, the observed band appears approximately as the envelope of the series of sharp lines defined in Eqs.4.21 and 4.22.

Intensity of the full band is I_0 and is independent of the value of S. The transition between the zero-point vibrational levels has the intensity $I_0 \exp(-S)$. For S=0, which means that the ground state and the excited state has the same electron-phonon coupling, all the intensity is contained in the zero-phonon line only [4.7]. For higher values of S, the excited state parabola is displaced along the Q-axis of the configuration co-ordinate diagram. In this case the vibrational wave functions in the ground state and the excited state is not identical and the vibrational wave function overlap integral is not subject to a strict orthogonality condition. As a result, the vibrational side-band structure corresponding to the transitions to the different vibrational levels of the excited state now appears together with the zero-phonon line. Since the total intensity of the absorption band is constant for given ground and excited states, the intensity of the zero phonon line is lower when it is accompanied by the phonon-sideband as compared to the intensity it would have in the absence of the sideband.

The maximum intensity of absorption (for S>0) occurs at an energy $(S-\frac{1}{2})\hbar\omega$ above the zero phonon line[4.7]. This corresponds to the transition to the vibrational level in the excited state whose position is defined by the intersection of the excited state configuration parabola and the vertical line drawn from the minimum of the ground state parabola in the configuration co-ordinate diagram.

Once excited to the upper vibrational levels of the excited state 'b', the ion relaxes rapidly to the lowest vibrational levels in the same state. It then decays radiatively or non-radiatively to the ground state. Since now the ion's initial state is 'b' corresponding to a configurational equilibrium position $Q_o^{(b)}$, according to the Frank-Condon principle the electronic transition to the ground state takes place at this same value of Q. That is, the most favorable path for the downward radiative transition is along the vertical line joining the minimum of the excited state parabola and the ground state parabola in the configuration co-ordinate diagram **(Fig.18)**. The shape of the emission band is a mirror image of the absorption band about the zero-phonon line if the excited state and the ground state parabolas have identical shape. This is the case when the effective force constants for the vibration is the same in both the states. In general, however, asymmetry between the two bands is observed in most of the cases. This is because the local environment around the active ion changes in different excited states resulting in different values of effective force constant of oscillation in these states.

Section 4.7: Non-radiative decay

In almost all solid state luminescent materials it has been observed that at sufficiently high temperatures the fluorescence intensity decreases with increasing temperature. This is usually accompanied by a shortening of the fluorescence life time

of the excited state. Such quenching of fluorescence intensity and lifetime is due to the decay of the ions in the excited states by various competing non-radiative decay channels. These non-radiative processes may be intra-ionic or inter-ionic.

The intra-ionic non-radiative decay is primarily a thermally activated process that induces the excited ion to decay to the ground state by emitting phonons. This type of multiphonon non-radiative processes can be explained very elegantly in terms of the configuration co-ordinate diagrams. One of the earliest and most commonly used models for non-radiative decay is the standard Mott-model [4.12, 4.13]. According to this model the non-radiative decay rate from the excited state to the ground state at the cross-over point of the ground state and the excited state configuration curves and can be expressed as

$$W_{nr} = A \exp(-\Delta_{10} / kT) \qquad (4.24)$$

where Δ_{10} is the energy difference between the minimum of the excited state configuration curve and the cross-over point of this curve with the configuration curve for the ground state **(Fig.19)** and k is the Boltzmann constant. T is the temperature. 'A' is a temperature independent constant and is defined as the reciprocal of the non-radiative lifetime for the actual conversion from the excited state to the ground state. The physics underlying Eq. (4.24) can be explained as follows:

At very low temperatures most of the excited ions are in the lowest vibrational levels of the excited state, i.e. near the minimum of the corresponding configuration co-ordinate curve. Within this state the ions are distributed amongst the available vibrational energy levels according to a Boltzmann distribution. Therefore, if the total number of excited ions is n_2 then the number of ions whose energy is Δ_{10} above the zero-point energy of this state is given by

$$n_2(\Delta_{10}) = n_2 \exp(-\Delta_{10} /kT). \qquad (4.25)$$

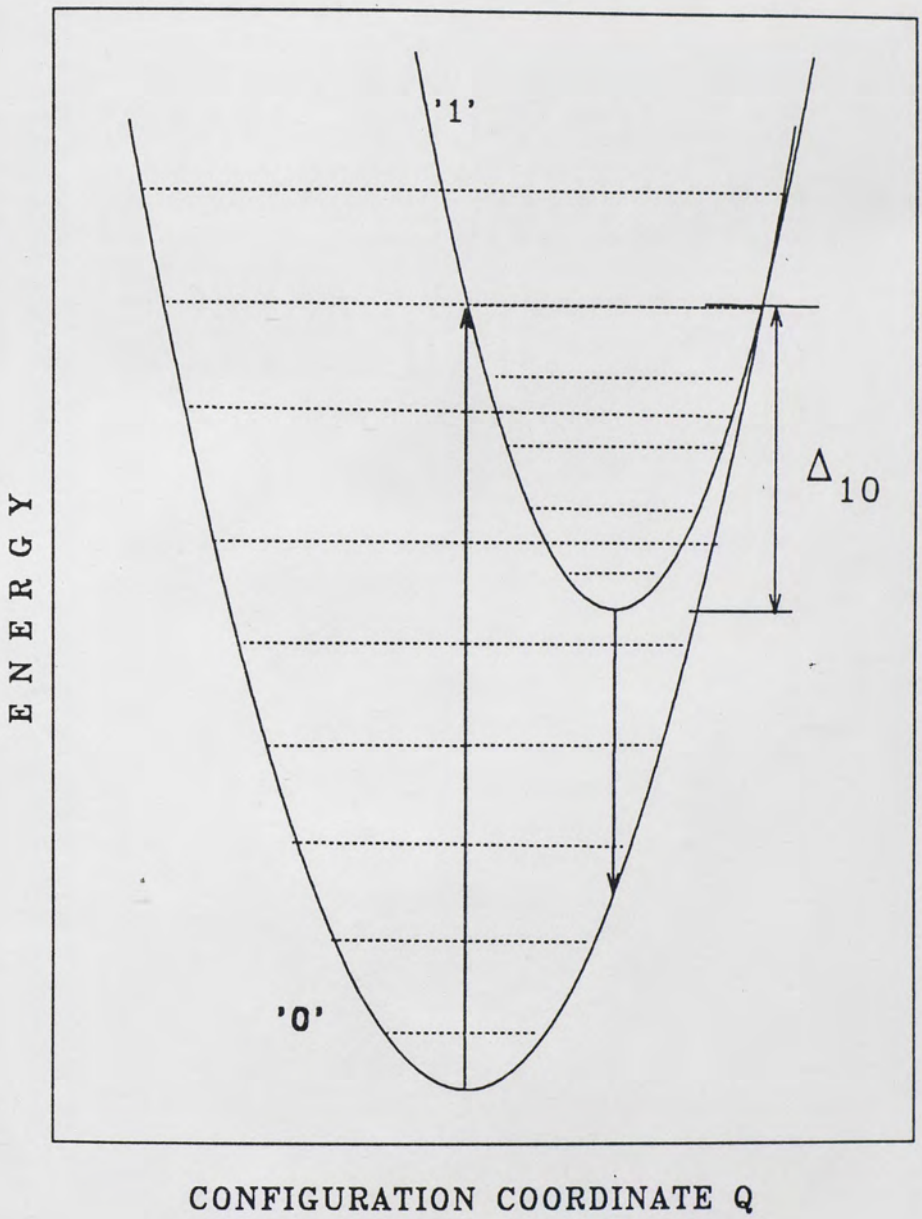

Figure 19. Schematic configurational coordinate diagram for Mott-model of the non radiative decay from the electronic state b to the ground state a. The dashed horizontal lines represent the vibrational energy levels in the two electronic states.

Now, at the cross-over point C, the excited state and the ground state are degenerate and are strongly mixed. As a result, an ion having the energy corresponding to the point C in the configuration coordinate diagram will have a finite probability of being in the vibrational level of the ground state which is in the neighborhood of the point C. Once an ion, which is initially in the excited state '1', goes over to the ground state '0' by such configuration mixing, the probability of it decaying to the lower vibrational levels of the ground state by multi-phonon emission becomes significantly higher than the probability of it going back to the state '1'. The primary reason for this is the extremely high vibrational level of excitation in the ground state '0' that it finds itself in following the cross-over from the state '1' by the configuration mixing process. Thus, as the temperature is increased, more and more of the excited ions find themselves near the cross-over point with a resulting proportional increase in the number of ions decaying to the ground state by multiphonon-emission. The total decay rate can be now expressed as

$$1/\tau = 1/\tau_r + (1/\tau_{nr}) \exp(-\Delta_{10} / kT) \qquad (4.26)$$

where τ_r is the temperature independent radiative lifetime and τ_{nr} is the temperature independent non-radiative internal conversion lifetime.

The above model applies very well to the temperature quenching of the broad band emissions of transition metal ions in crystals. Such broad band emissions result of the transitions from an excited state having a large offset relative to the ground state in the configuration co-ordinate diagram **[4.14 - 4.18]**.

The temperature quenching of the sharp-line emissions are in general difficult to interpret in terms of Mott's single activation energy model. That is because the sharp-line emissions result from the transition between two states with a very small offset of the excited state potential energy parabola relative to the ground state parabola; in that case the configuration coordinate curves do not cross or, if at all, cross at energies too

high above the zero phonon electronic level of the excited state to account for the observed temperature quenching of the fluorescence intensity and lifetime. For such cases, the temperature dependent non-radiative decay rates are interpreted in terms of multiphonon emissions to the sea of lattice modes. This approach is related to the model described in **section 4.6** in the discussion for the shapes of emission and absorption bands and was first developed by Kiel [4.19]. According to this model the multiphonon emission rate is given by

$$W^{(p)} = A_K \varepsilon^p (1+<m>)^p \qquad (4.27)$$

where $p\hbar\omega_o = E_{zp}$; Here $\hbar\omega_o$ is the lattice-phonon energy, p is the number of phonons required to bridge the electronic energy gap (E_{zp}) between the initial state and the final state, and $<m> = [\exp(\hbar\omega_o / kT) - 1]^{-1}$. ε is a coupling constant and A_K is a temperature independent rate constant. This model has been used to interpret the temperature dependent quenching of the fluorescence of many rare-earth ions in crystals[4.20].

In 1975 Struck and Fonger [4.21] presented a unified model of the temperature quenching of both narrow-line and broad-band emissions based upon the single configuration co-ordinate model for the energy levels of the ions in crystalline hosts using a quantum-mechanical approach to the problem. For large offset, this model gives approximately Mott's single-activation-energy rate for upward transitions but faster rates poorly described by a single activation energy for downward transitions. For small offset, the model approaches Kiel's formula for multi-phonon emission rate for downward transitions.

Struck and Fonger's model uses basically the quantum mechanical single configuration co-ordinate (QMSCC) transition rates developed initially by Williams and Hebb [4.17] following Condon's quantum mechanical treatment of the FC-

principle[4.22]. According to this model the non-radiative rate for the transition from an upper state (b,v) to a lower state (a,u) is given by

$$N_{bv,au} = N_{ba} (1-n_b)\, n_b^{\,v} \langle \chi_a(u) | \chi_b(v) \rangle^2 \qquad (4.28)$$

where $n_b = \exp(-\hbar\omega_b/kT)$ is the Boltzmann-factor between adjacent vibrational levels in the upper state 'b' . $\chi_a(u)$ and $\chi_b(v)$ are the vibrational wave functions corresponding to the states (a,u) and (b,v) respectively. The overlap integrals $\langle \chi_a(u) | \chi_b(v) \rangle$ are easily generated by the recursion formulas given by Manneback [4.20 - 4.23] .

The total non-radiative rate from 'b' to 'a' is given by the sum over all the upper state vibrational levels v which are resonant with some vibrational level of the lower state 'a'. The temperature dependence of the non-radiative rate comes through the thermal-FC weights $(1-n_b)\, n_b^{\,v} \langle c_a(u) | c_b(v) \rangle^2$.

Section 4.8: Inter-ionic non-radiative process

Fluorescence from a given set of ions (donors–D) in a solid medium may be quenched if the population of these ions in the excited states is partially lost by the non-radiative transfer of energy from the excited D-ions to other type of centers (acceptors–A). The centers 'A' may be totally non-radiating traps or killer centers, or ions of a different kind which emits radiation at wavelengths different from the fluorescence wavelengths of the D-ions. The quenching due to the energy transfer processes may or may not be temperature dependent, depending mainly upon whether the process is a non-resonant or a resonant one. In the non-resonant process the transfer is made possible by the emission or absorption of one or more phonons to make up for the energy difference between the donor and the acceptor excited levels which participate in the transfer process. Such phonon-assisted transfer rates usually depend on the temperature by the relations of the form

$$W_{nr} = W_{DA} \exp(-\Delta_{DA} / kT), \qquad (4.29)$$

where Δ_{DA} is the energy difference between the electronic states of the donor and the acceptor centers participating in the transfer process. W_{DA} is a temperature independent rate constant.

The ion-ion energy transfer may be mediated by electric or magnetic multipolar interactions or exchange interactions. The microscopic energy transfer process in inorganic materials was first considered theoretically by Forster and Dexter[4.24, 4.25]. Among the multipolar interactions, the electric dipole-dipole interactions between donor and the acceptor ion is often found to be the strongest mechanism for the energy transfer.

The probability for a donor-acceptor energy transfer can be written, by Fermi's Golden rule, as

$$W_{DA} = \frac{2\pi}{\hbar} |\langle D,A^*|\mathcal{H}'|D^*,A\rangle|^2 \int g_D(E) g_A(E) dE \qquad (4.30)$$

where $|D^*,A\rangle$ is the initial state when the donor ion is in the excited state D* and the acceptor ion is in the ground state A. $|D,A^*\rangle$ represents the final state after the energy transfer which leaves the donor in the ground state D and the acceptor in the excited state A*. The overlap integral of the line shape functions $g_D(E)$ for the $D^* \rightarrow D$ downward transition and $g_A(E)$ for the $A \rightarrow A^*$ upward transition implies that the energy transfer can take place most favorably when the energy released on de-excitation of the donor ion is high enough to excite the acceptor ion. As mentioned above, this condition may be relaxed in phonon-assisted energy transfers where one (or more) phonon(s) make up for any energy imbalance between the $D^* \rightarrow D$ and the $A \rightarrow A^*$ processes. $\mathcal{H}'_{es}$ is the electrostatic interaction between the electrons on the donor and the acceptor ions and can be expressed as

$$\mathcal{H}'_{es} = \frac{1}{4\pi\varepsilon_0 \kappa} \sum_{i,j} \frac{1}{\left|\vec{R} + \vec{r}_{Aj} - \vec{r}_{Di}\right|} \qquad (4.31)$$

where $\vec{r}_{Aj}$ and $\vec{r}_{Di}$ are the position vectors of the electrons on the acceptor ion and the donor ion relative to the respective nuclei. $\vec{R}$ is the inter-nuclei distance between the donor and the acceptor. The quantity inside the summation can be expanded as a sum of multipoles giving

$$\mathcal{H}'_{es} = \frac{1}{4\pi\varepsilon_0\kappa} \sum_{i,j} \sum_{k_1,k_2} \sum_{q_1,q_2} \frac{G(k_1,k_2,q_1,q_2)}{R^{k_1+k_2+1}} [C^{(k_1+k_2)}_{q_1+q_2}(\theta,\phi)]^* \mu^{(k_1)}_{q_1}(\vec{r}_D)\, \mu^{(k_2)}_{q_2}(\vec{r}_A) \tag{4.32}$$

where,

$$C^{(k)}_q(\theta,\phi) = \sqrt{\frac{4\pi}{2k+1}}\, Y^{(k)}_q(\theta,\phi) \tag{4.33}$$

$$\mu^{(k)}_q(\vec{r}_D) = \sum_i e r^{(k)}_{Di}\, C^{(k)}_q(\theta_{Di},\phi_{Di}) \tag{4.34}$$

and

$$G(k_1,k_2,q_1,q_2) = (-1)^{-k_1} \sqrt{\frac{(2k_1+2k_2+1)}{(2k_1)!(2k_2)!}} \begin{pmatrix} k_1 & k_2 & k_1+k_2 \\ q_1 & q_2 & -q_1-q_2 \end{pmatrix}. \tag{4.35}$$

$Y^{(k)}_q(\theta,\phi)$ is a spherical harmonic function. $\mu^{(k)}_q(\vec{r}_D)$ is the electric-multipole operator of the order (k) corresponding to the donor electrons. A similar expression for the acceptor ion can be written in terms of its co-ordinates relative to the acceptor nucleus.

The result obtained for $|\langle D,A^*|\mathcal{H}'_{es}|D^*,A\rangle|^2$ using the above expression for $\mathcal{H}'_{es}$ when averaged over θ,ϕ, neglecting the cross-terms, gives a simple form

$$|\langle D,A^*|\mathcal{H}'_{es}|D^*,A\rangle|^2$$

$$= \left(\frac{1}{4\pi\varepsilon_0\kappa}\right)^2 \sum_{k_1,k_2} R^{-2(1+k_1+k_2)} \times \frac{(2k_1+2k_2)!}{(2k_1+1)!(2k_2+1)!} \left|\mu^{(k_1)}_D\right|^2 \left|\mu^{(k_2)}_A\right|^2 \tag{4.36}$$

where

$$\left|\mu_D^{(k_1)}\right|^2 = \sum_{q_1} |\langle D| \mu_{q_1}^{(k_1)}(\vec{r}_D)|D^*\rangle|^2, \tag{4.37}$$

$$\left|\mu_A^{(k_2)}\right|^2 = \sum_{q_2} |\langle A| \mu_{q_2}^{(k_2)}(\vec{r}_A)|A^*\rangle|^2. \tag{4.38}$$

The summation over q_1 is from $-k_1$ to $+k_1$ while summation over q_2 is from $-k_2$ to $+k_2$.

For $k_1=1$, $k_2=1$ the interaction is electric dipole-dipole. The transition probability for the energy transfer from D to A by this interaction is

$$W_{DA}^{dd} = \frac{4\pi}{3\hbar}[4\pi\varepsilon_o\kappa]^{-2}\frac{1}{R^6}\left|\mu_D^{(1)}\right|^2\left|\mu_A^{(1)}\right|^2 \int g_D(E)g_A(E)dE. \tag{4.39}$$

For $k_1=1$, $k_2=2$ the interaction is electric dipole-quadrapole. The transition probability for the energy transfer from D to A by this interaction is

$$W_{DA}^{dq} = \frac{4\pi}{3\hbar}[4\pi\varepsilon_o\kappa]^{-2}\frac{1}{R^8}\left|\mu_D^{(1)}\right|^2\left|\mu_A^{(2)}\right|^2 \int g_D(E)g_A(E)dE. \tag{4.40}$$

At this point one should note that the ratio of the dipole-quadrupole non-radiative transition probability to the dipole-dipole non-radiative transition probability between neighboring ions is of the order of 0.01. This is significant compared to the ratio of an allowed electric quadrupole to electric dipole radiative transition probabilities, which is of the order of 10^{-7}. Therefore, in solid materials, where electric quadrupole radiative transitions are negligible, the dipole-quadrupole or even quadrupole-quadrupole non-radiative energy transfer processes can not be ignored.

Section 4.9: Effect of non-radiative energy transfer on lifetime of the donor

Study of the fluorescence lifetime of luminescent ions in solid state materials provide valuable information on the dynamics of the system as a whole. Presence of non-radiative energy transfer processes in the system often manifests through an initial rapid decay of the donor-fluorescence. In general, this results in a non-exponential temporal profile of the fluorescence intensity measured as a function of time.

In order to be able to analyze the experimental decay curves quantitatively it is necessary to incorporate the microscopic-rate formulae derived above into a statistical formalism valid for the bulk material, containing millions of closely packed ions. This problem was first treated by Forster[4.26]. The starting equation for such a treatment is the set of rate equations

$$\frac{d}{dt}\rho_j(t) = -\frac{1}{\tau_{int}}\rho_j(t) - \rho_j(t)\sum_{i=1}^{N_A} W_{DA}(\vec{R}_{ji}) \qquad (4.41)$$

where $\rho_j(t)$ is the probability that the donor ion j is excited at time t, $W_{DA}(\vec{R}_{ji})$ is the microscopic transition probability of energy transfer from the j-th donor ion to the i-th acceptor ion, $\vec{R}_{ji}$ being the vector joining the two ions. τ_{int} is the intrinsic decay rate of the excited state of the donor ion in the absence of the acceptor ions and is given by

$$\frac{1}{\tau_{int}} = \frac{1}{\tau_r} + W_{nr}^{(int)} \qquad (4.42)$$

where τ_r is the radiative lifetime and $W_{nr}^{(int)}$ is the intrinsic non-radiative decay rate of the donor ion.

The number of excited donor ions is given by the product of the total number of donor ions in a given volume and the configurational average $\overline{\rho}(t)$ of $\rho_j(t)$ over all arrangements of donor and acceptors [4.7, 4.27, 4.28 (p.321)]. An exact solution for $\overline{\rho}(t)$ is given by

$$\overline{\rho}(t) = \exp(-t/\tau_{int}) \prod_{l} [1 - C_A + C_A \exp(-W_{DA}(R_{0l})t)] \qquad (4.43)$$

where C_A is the probability that a site is occupied by an acceptor and l (1,2,3,....) designates all the different possible acceptor sites whose positions are measured with reference to any given excited donor in the crystal. Using the continuum approximation [4.29], the above expression may be obtained in a general form

$$\overline{\rho}(t) = \exp(-t/\tau_{int}) \left[\frac{1}{V} \int \exp\{-W_{DA}(R)t\} 4\pi R^2 \, dR \right]^{N_A}, \qquad (4.44)$$

where N_A is the number of acceptors in the volume, V, and $W_{DA}(R)$ is the rate of energy transfer from a donor to an acceptor at a distance, R. For electric multipolar interactions it becomes

$$\overline{\rho}(t) = \exp\{-t/\tau_{int} - \frac{n_A}{n_o} \Gamma(1-\frac{3}{n})(t/\tau_{int})^{3/n}\}, \qquad (4.45)$$

(n = 6, 8 and 10 corresponds to dipole-dipole, dipole- quadrapole and quadrapole-quadrapole interactions respectively) [4.28(p.323)]. n_A is the concentration of acceptor ions, $\Gamma(x)$ is a gamma-function and n_o is a critical concentration.

In the case of the exchange interaction the corresponding expression is

$$\overline{\rho}(t) = \exp\{-t/\tau_{int} - \gamma^{-3}(\frac{n_A}{n_o}) g(e^{\gamma} t/\tau_{int})\}, \qquad (4.46)$$

$$g(x) = 6x \sum_{m=0}^{\infty} \frac{(-x)^m}{(m+1)^4 m!}, \qquad (4.47)$$

and γ is a parameter related to the radial extent of the D and A wave functions.

Because of the random distribution of the acceptors some excited donors will find acceptors in the immediate neighborhood while others will have acceptors only as distant neighbors. The donors with acceptors in the nearest neighborhood will decay rapidly by the non-radiative energy transfer process. The donors which are away from

acceptors have very low probability of transferring their energy to the distant acceptors by non-radiative energy transfer and usually decay at the intrinsic rate as if there were no acceptors. So, at later times, one observes the decay of these ions and the fluorescence intensity decreases according to an exponential function of time at a rate corresponding to the case when there are no acceptors in the system. However, if there is donor-donor energy transfer in addition to donor-acceptor energy transfer, the donor excitation energy may migrate rapidly among the donors. As a result, the excitation has a higher chance of arriving at a donor site having acceptors in close proximity and transferring the excitation energy to one of them. The effect of such a rapid donor-donor migration is to average out the local environment of all the donor sites in the medium, thereby resulting in the same effective number of nearest neighbor acceptor sites for each donor. All the excited donors then have, on the average, an equal chance of losing the energy by energy transfer to an acceptor following the initial excitation. For a small migration rate among the donors the population decreases at the initial times following the excitation ($t << \tau_{int}$) at a rate determined by the acceptor concentration and the D-A energy transfer probability and the temporal change of the fluorescence intensity is non-exponential. At later times ($t >> \tau_{int}$) the decay becomes nearly exponential but the asymptotic decay rate is smaller than τ_{int} and is determined by not only the acceptor concentration and donor-acceptor energy transfer rate but also the donor concentration and the donor-donor energy transfer rate.

A general expression for the fluorescence intensity as a function of time, when both donor-donor and donor-acceptor energy transfer processes are present, can be obtained by solving the diffusion equation for the excitation density $\rho(\vec{R},t)$ and integrating the solution over $\vec{R}$. The diffusion equation in this case can be written as:

$$\frac{\partial}{\partial t}\rho(\vec{R},t) = [-\frac{1}{\tau_{int}} + D\nabla^2 - \sum_{i=1}^{N_A} W_{DA}(\vec{R} - \vec{R}_i)]\rho(\vec{R},t) \qquad (4.48)$$

and the fluorescence intensity

$$\phi(t) = \int \rho(\vec{R},t)\, d^3\vec{R}. \tag{4.49}$$

Yakota and Tanimoto [4.30] obtained an approximate solution for the dipole-dipole interaction process between the donor and the acceptor which is given by

$$\phi(t) = \exp[-t/\tau_{int} - \frac{n_A}{n_o}\Gamma(1/2)\,(t/\tau_{int})^2\,(\frac{1+10.87y+15.5y^2}{1+8.743y})^{3/4}], \tag{4.50}$$

where

$$y = D\tau_{int}R_o^{-2}\ \ (t/\tau_{int}). \tag{4.51}$$

D is a diffusion constant which characterizes the migration among donor ions. It depends on the donor-donor microscopic energy transfer rate and on the donor concentration. The parameter R_o is defined as the separation between a donor and an acceptor for which the non-radiative energy transfer rate from the donor ion to the acceptor ion by a given electric multipole process would be the same as the intrinsic decay rate of the donor ion in absence of the acceptors. Therefore, if we define

$$W_{DA}(R) = \frac{\alpha_{DA}^{(n)}}{R^n} \tag{4.52}$$

then according to the above definition,

$$\frac{1}{\tau_{int}} = \frac{\alpha_{DA}^{(n)}}{R_o^{\,n}}. \tag{4.53}$$

As before, n=6 corresponds to the dipole-dipole process. The critical concentration n_o is defined as $n_o = (\frac{4}{3}\pi R_o^3)^{-1}$.

The initial part of the decay is non-exponential and follows the functional form of the Eq.(4.45) if the donor-acceptor transfer is via multipolar interaction process. At longer times, however, the decay becomes exponential and the asymptotic value is given by

$$\frac{1}{\tau} = \frac{1}{\tau_{int}} + W_{DA}^{(diff)} . \tag{4.54}$$

$W_{DA}^{(diff)}$ depends on the donor and acceptor concentrations and the donor-donor and the donor-acceptor interaction strengths. In particular, if both the donor-donor and donor-acceptor energy transfer processes are mediated through dipole-dipole interactions, the asymptotic decay rate can be written as [4.27]

$$\frac{1}{\tau} = \frac{1}{\tau_{int}} + 21 n_A n_D (\alpha_{DD}^{(6)})^{3/4} (\alpha_{DA}^{(6)})^{1/4} . \tag{4.55}$$

$\alpha_{DA}^{(6)}$ is defined in the general Eq. (4.52), with a similar expression for $\alpha_{DD}^{(6)}$. n_D is the donor concentration. The diffusion model, however, is valid in general only if the donor-donor transfer mechanism is much weaker than the donor-acceptor transfer mechanism [4.7(p.456), 4.27, 4.31]. If, however, the donor-donor energy transfer mechanism is stronger than the donor-acceptor energy transfer mechanism, the resulting rapid migration of the excitation energy between the donor ions may be treated as a statistical random walk process [4.28, 4.32]. In that case the fluorescence intensity as a function of time can be expressed as

$$\phi(t) = \overline{\rho}(t) e^{-t/\tau_o} + \tau_o^{-1} \int_0^t \phi(t - t') \overline{\rho}(t') e^{-t'/\tau_o} dt' , \tag{4.56}$$

where τ_o is the mean length of time in which the excitation energy resides on a donor before hopping over to another. Eq. (4.56) represents the so-called hopping model. $\overline{\rho}(t)$ is given by either Eq. (4.45) or (4.46) and therefore this model can be used to test experimental results involving all cases donor-acceptor energy transfer mechanisms (electric multipole or exchange). As in the diffusion model the initial part of the decay is non-exponential but at longer times it becomes exponential, the asymptotic decay rate being

$$\frac{1}{\tau} = \frac{1}{\tau_{int}} + W_{DA}^{(hopping)}, \qquad (4.57)$$

where $W_{DA}^{(hopping)}$ is a constant that depend on the donor and acceptor concentration as well as the donor-donor and the donor-acceptor interaction strengths. For the diffusion model an approximate analytical formula for the fluorescence decay is available only for the dipole-dipole donor to acceptor energy transfer process in presence of donor-donor migration (Eq. 4.50).

CHAPTER 5

ANALYSES OF SPECTROSCOPIC DATA AND THEORETICAL MODELING OF FLUORESCENCE DYNAMICS

Brief descriptions of the experimental results on the spectroscopy of each of the crystals investigated in this work are already given in Chapter-3. In this chapter the theoretical analyses are presented for the experimental data. Since the basic aim of this work is to develop a systematic approach to the problem of crystal field engineering of efficient Cr^{4+} doped laser crystals the analyses of the observed data are conducted from that perspective only. In other words, more emphasis is given to the interpretation of the spectroscopic properties of those crystals which provided fairly complete observable properties of the Cr^{4+} ion in the tetrahedral site, including polarized absorption spectra, fluorescence spectra, fluorescence lifetime, the temperature dependence of fluorescence lifetime and intensities and laser action in the near infrared.

Among the newly developed Cr^{4+} doped crystals Cr^{4+}:Y_2SiO_5 provided the most complete set of spectroscopic information. It includes polarization dependent absorption, pump wavelength dependent fluorescence and temperature dependent lifetimes. It was also the only purely Cr^{4+} doped crystal whose fluorescence intensity was strong enough to show any laser action in the near infrared. This crystal, together with Cr-doped forsterite, forms a mutually complimentary set for studying the optical behavior of the Cr^{4+} ion in tetrahedral site.

The polarized absorption spectra of Cr^{4+}:Y_2SiO_5 at room temperature and 77 ^{o}K are shown in Figs.2(a) and 2(b) respectively. Fig.3 shows the luminescence spectra

at different temperatures and under different excitations. These spectra show the typical characteristics of a simple multiphonon coupled d^2 ion in a tetrahedral site.

The absorption spectra of Cr^{4+}:Y_2SiO_5 is characterized by a strong polarization dependence of the absorption bands in the visible. We have conducted the analysis of the absorption spectrum on the basis of the Tanabe-Sugano formalism[5.1]. The observed spectra are consistent with a slightly distorted tetrahedral symmetry. However the basic features of the absorption spectrum can still be quite adequately explained in terms of the ideal symmetry group T_d **[Fig. 16]**.For an ion with d^2 electron configuration in symmetry T_d the first few energy levels, expressed in terms of the Racah parameters B, C and the crystal field splitting parameter Dq, are given by[5.2] :

$$U(^3A_2) = -12\,Dq \tag{5.1a}$$

$$U(^1E) = -12Dq + 8B + 2C - 6B^2/(10Dq) \tag{5.1b}$$

$$U(^1A_1) = -12Dq + 16B + 4C - 108B^2/(10Dq) \tag{5.1c}$$

$$U(^3T_2) = -2\,Dq \tag{5.1d}$$

$$U(^3T_1(^3F)) = 3Dq + 7.5B - 1/2\,[\,225B^2 + (10Dq)^2 - 180DqB\,]^{1/2} \tag{5.1e}$$

$$U(^3T_1(^3P)) = 3Dq + 7.5B + 1/2\,[\,225B^2 + (10Dq)^2 - 180DqB\,]^{1/2} \tag{5.1g}$$

$$U(^1T_1) = -2Dq + 12B + 2C \tag{5.1h}$$

In the above notation $U(^3A_2)$, $U(^1E)$, $U(^3T_2)$ etc. are the energies corresponding to the states $^3A_2$, ^1E, $^3T_2$ etc. respectively. The values of the parameters B, C and Dq are to be determined from experiment.

The sharp line at 1146 nm in low temperature luminescence spectrum is attributed to the spin-forbidden transition from the ^1E level to the ground state $^3A_2$. Therefore,

$$U(^1E) - U(^3A_2) = 8B + 2C - 6B^2/(10Dq) = 8726\ cm^{-1}. \tag{5.2}$$

The broad-band luminescence, on the other hand, is attributed to the $^3T_2$ - $^3A_2$ transition. On the basis of single configuration co-ordinate model the predicted position of the zero-phonon line for this transition is at 1158 nm and so

$$U(^3T_2) - U(^3A_2) = 10Dq = 8631 \text{ cm}^{-1}. \quad (5.3)$$

Also attributing the sharp line at 678 nm in the 77 ^oK absorption spectrum to the $^3A_2$ - $^1A_1$ transition, we have

$$U(^1A_1) - U(^3A_2) = 16B + 4C - 108B^2/(10Dq) = 14{,}749 \text{ cm}^{-1}. \quad (5.4)$$

Solving for B, C and Dq using Eqs. (2), (3) and (4) we obtain,

$$Dq = 831.1 \text{ cm}^{-1}, \; B = 468.44 \text{ cm}^{-1}, \; C = 2500 \text{ cm}^{-1}.$$

The absorption peak at 489 nm is attributed to the $^3A_2$ (ground state) – $^3T_1[^3P]$ transition. Using the corresponding transition energy value of 20449.9 cm^{-1} we obtain,

$$1/2 \, [\, 225B^2 + 100Dq^2 - 180DqB \,]^{1/2} = 3990.1 \text{ cm}^{-1} \quad (5.5)$$

which in turn predicts the $^3T_1(^3F)$ level 12469.7 cm^{-1} above the $^3A_2$ ground state and a corresponding absorption at 801.9 nm. This is in the same wavelength region where the strong broad band near infrared absorption was actually observed. Also the prediction of this calculation for the $^3A_2$ (ground state) – $^1T_1(^3P)$ transition is a sharp line absorption at 519.4 nm. This is also experimentally observed at 77 ^oK. We note that the strongly polarization dependent absorption band around 600 nm is not accounted for in the above calculations based upon an ideal tetrahedral symmetry. To account for this discrepancy it is necessary to consider the possibility of a symmetry lower than T_d. The observed dichroism indicates a C_{3V} symmetry group for the Cr^{4+} site. The lower symmetry results from the distortion in the $(CrO_4)^{4-}$ tetrahedron in Cr^{4+}:Y_2SiO_5. In the symmetry C_{3V}, the $^3T_1$ (^3F) level will split into two components, namely $^3E[^3T_1(^3F)]$ and $^3A_2[^3T_1(^3F)]$ as shown in **Fig.20** [5.3]. In that case we can attribute the 801.9 nm

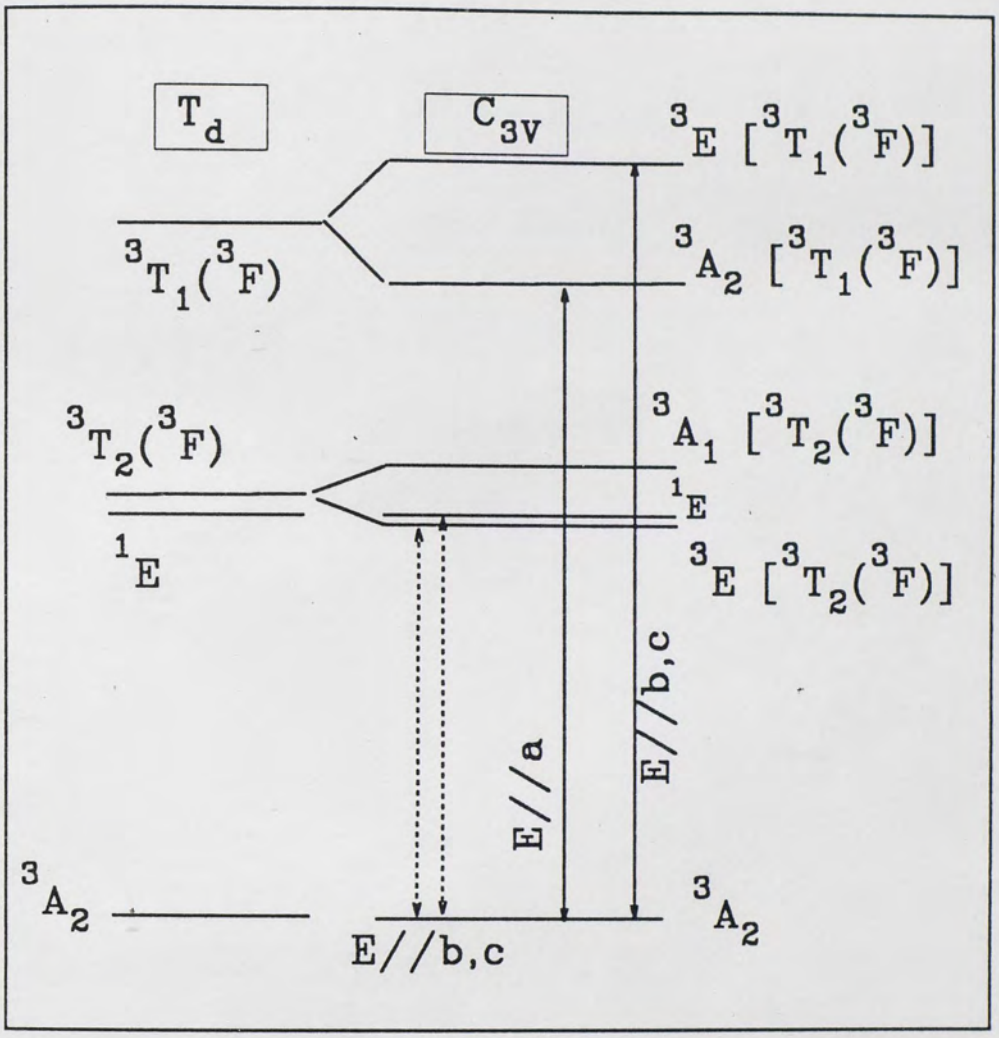

Figure 20. Schematic diagram of the energy level splitting and the polarization selection rules for the electric dipole radiative transitions of the Cr^{4+} ion in the symmetry C_{3V}.

TABLE 5.1

ENERGY LEVELS OF Cr^{4+} IN Y_2SiO_5
WITH REFERENCE TO THE $^3A_2$ GROUND STATE

	ENERGY LEVELS	
Cr^{4+} states	**Calculated (cm^{-1})**	**Experimental (cm^{-1})**
^1E	----------	8726* (1146 nm)
$^3T_2$	8631* (1158.6 nm)	8631* (1158.6 nm)
$^3A_2$ [$^3T_1(^3F)$]	12,470 (801.9 nm)	12,468 , 13,369, 13,947
$^1A_1$	----------	14,749 (678 nm)
^3E [$^3T_1(^3F)$]	----------	16,611 (602 nm)
$^3A_2$ [$^3T_1(^3P)$]	----------	20,449.9 (489 nm)
^3E [$^3T_1(^3P)$]	24,594 (406.6 nm)	24,691 (405 nm)
$^1T_2$	17,094 (585 nm)	17,301 (578 nm)
$^1T_1$	19,252.9 (519.4 nm)	19,841 (504 nm)

*Obtained from the zero phonon lines in the low temperature luminescence spectrum.

peak to the transition from the ground state to the $^3A_2[^3T_1(^3F)]$ state and the 602 nm peak to the transition from the ground state to the $^3E\,[^3T_1(^3F)\,]$ state. Such an assignment is also consistent with the polarization selection rules for the C_{3V}. The energy gap between these two split components of $^3T_1(^3F)$ in that case is 4140.9 cm^{-1}. Assuming a similar splitting of the $^3T_1(^3P\,)$ level one can predict a second absorption band near 406.6 nm. It is interesting to note that a relatively weak absorption peak is indeed observed near that wavelength **[Fig. 2(b)]** . The energy levels of Cr^{4+} in Y_2SiO_5 are summarized in Table-5.1.

The crystal field parameters determined in this work correspond to a fairly strong crystal field environment for the Cr^{4+} site, with 10Dq/B = 18.42. As we will see, such values for the crystal field parameters are also consistent with the fluorescence dynamics of the Cr^{4+} ion in the tetrahedral site presented in this paper.

The room temperature fluorescence spectrum due to 1064 nm pumping is a broad band with a peak near 1225 nm. At very low temperatures this broad band is accompanied by an intense sharp line at 1146 nm [Fig.3(a)]. This line can be distinguished at temperatures up to 77 ^oK. With further increase of the temperature, the width of the broad band increases in spectral range but its intensity decreases considerably. The shape of the broad band resembles that predicted by the single configuration coordinate (SCC) model[5.4,5.5,5.6]. This band is attributed to the $^3E(\,^3T_2\,) - \,^3A_2$ transition of Cr^{4+}.

According to the single configuration coordinate model for multiphonon coupled transitions[5.4, 5.5, 5.6] the shape of the luminescence band is determined by the envelope of a series of sharp lines shifted from the zero phonon line by $m\hbar\omega$, where m is an integer and ω is the lattice vibration frequency. The intensity of the m^{th} line is $\exp(-S)S^m/m!$ where S is the Huang-Rhys parameter. Huang-Rhys parameter defines the difference in the excited state and ground state electron-phonon couplings. A value

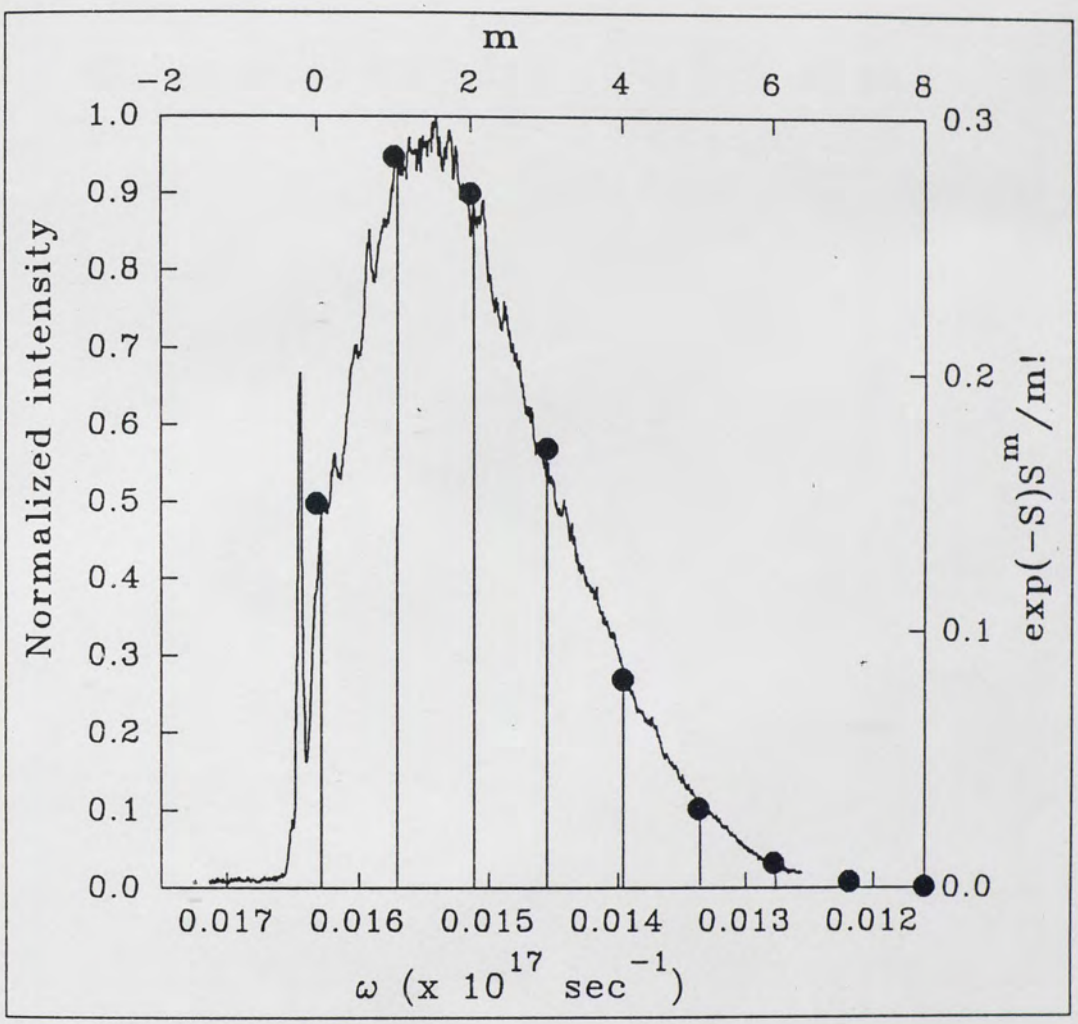

Figure 21. Comparison of the theoretical band shape based on the single configurational coordinate model and the experimental fluorescence spectrum excited by 1064 nm at 10 ^{o}K. The vertical lines with black circles at the top represent the magnitudes of [exp(-S) S^{m}]/m! (right hand vertical axis) for different values of m (top horizontal axis).

of S=1.9 fits the broad band as shown in **Fig.21**. This also gives a value of 309.45 cm^{-1} for $\hbar\omega$. This SCC fit predicts the $^3E(^3T_2) - {}^3A_2$ zero phonon line at 8631 cm^{-1} (1158 nm). The sharp line at 1146 nm is then attributed to the $^1E - {}^3A_2$ zero phonon transition.

Precision measurements showed that the decay of the fluorescence resulting from the excitation by 1064 nm radiation was nearly exponential with a small curvature at the initial times and was found to fit best with the functional form

$$I(t) = \exp(-t/\tau - \gamma\sqrt{t}), \tag{5.6}$$

where $I(t)$ is the fluorescence intensity normalized to unity at $t = 0$ **[Fig.22]**. According to the Forster-Dexter model[5.7 - 5.11] for energy transfer between ions the presence of the factor $\exp(-\gamma\sqrt{t})$ in Eq. (5.6) indicates that there is a dipole-dipole donor-acceptor energy transfer mechanism in the system, γ being the micro parameter representing the dipole-dipole donor-acceptor energy transfer process. In this chapter, the term lifetime will always refer to the calculated value of τ obtained by fitting the decay curves with Eq. (5.6).

In a temporal decay of the fluorescence that follows Eq.(5.6) τ is the intrinsic lifetime of the active ion (donor) defined by

$$\frac{1}{\tau} = \frac{1}{\tau_r} + W_{nr}^{(intra)}, \tag{5.7}$$

where τ_r is the radiative lifetime of the excited state and $W_{nr}^{(intra)}$ is the intra-ionic non–radiative decay rate of the excited state in the absence any donor-donor energy transfer. The non-radiative decay rate $W_{nr}^{(intra)}$ is determined by the ion-lattice interaction and depends on temperature only. Since at extremely low temperatures $W_{nr}^{(intra)}$ tends to zero the low temperature value of τ can be taken as the radiative lifetime τ_r of the excited state under study. However, as will be shown later, for Cr^{4+} in Y_2SiO_5 the calculated value of τ (from Eq.5.6) must be interpreted so as to include also

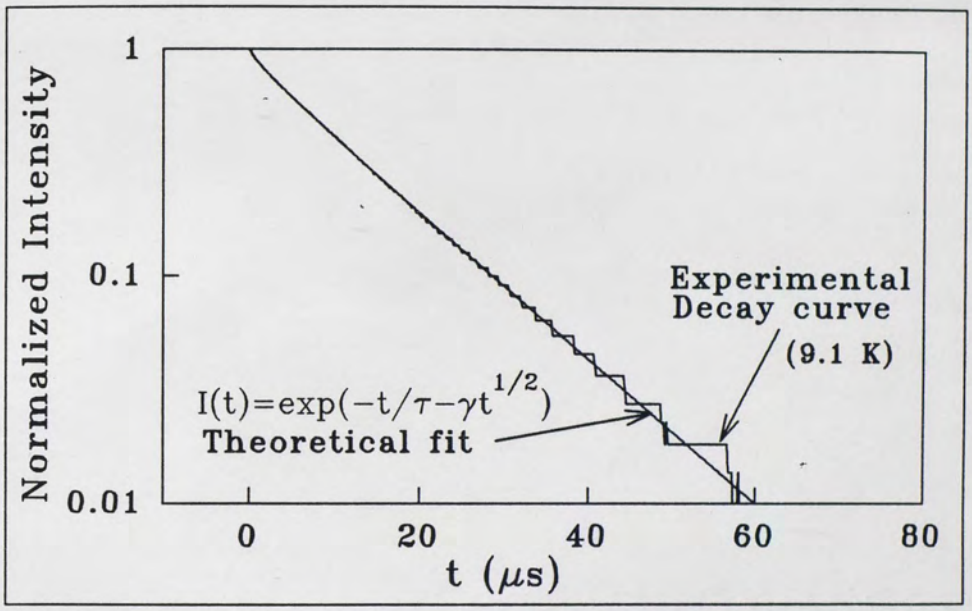

Figure 22. Fluorescence decay of Cr^{4+}:Y_2SiO_5 at 1200 nm measured at 9.1 ^oK. The smooth line is the theoretical fit using Forster-Dexter dipole-dipole energy transfer model. The excitation wavelength was 1064 nm from a Q-switched Nd:YAG (10 ns pulse duration at 10 Hz repetition rate).

a donor-donor energy transfer rate and therefore should actually be written as[5.12, 5.13]

$$\frac{1}{\tau} = \frac{1}{\tau_r} + W_{nr}^{(intra)} + \overline{W} \qquad (5.8)$$

where $\overline{W}$ gives the non-radiative decay rate due to ion-ion energy transfer processes in presence of rapid donor-donor migration of the excitation energy (hopping model). In that case the calculated value of τ at very low temperature can no longer be taken as the radiative lifetime but instead it gives the value of $(\frac{1}{\tau_r} + \overline{W}_o)^{-1}$, where $\overline{W}_o$ is the effective temperature independent non-radiative decay rate due to donor-acceptor energy transfer in presence of rapid donor-donor migration.

The lifetime of the fluorescence excited by 1064 nm pumping varies with temperature from about 14.1 μs at 10 ^oK to 593 ns at 300 ^oK. This variation is shown in Fig.23 and Fig.24(b) and indicates strong non-radiative processes .

We observed that the lifetime τ of the fluorescence measured at the 1146 nm line was always the same as the fluorescence in the broad band. This indicated a strong mixing of the ^1E and the $^3E(^3T_2)$ states. The crystal field parameters obtained from the analysis of the absorption and the emission spectra would correspond to a position very close to the cross-over point of the ^1E and $^3T_2$ levels in the Tanabe-Sugano diagram[5.1, 5.2] for the Cr^{4+} ion in a tetrahedral site **[Fig.16]**. In that case, a strong mixing of these two states is to be expected with resulting thermalization of their populations.

Donegan *et.al.*[5.6] have shown that the SCC model with single breathing mode for the lattice vibration with frequency ω can also account for the temperature dependence of lifetime of the NIR fluorescence of systems such as the Ni^{2+}:$LiGa_5O_8$. This means that the phonons which determine the shape of the emission

band are also responsible for the primary mode of non-radiative decay in such systems. According to this model, the non-radiative decay rate can be expressed as [5.4, 5.5, 5.6]

$$f_{nr}(T) = f_{nr}(0)p!S^{-p}\, e^{-2nS}\left(\frac{n+1}{n}\right)^{p/2} I_p[2S\sqrt{n(n+1)}] \qquad (5.9)$$

where I_p is the modified Bessel function of order p; n is the Bose-Einstein occupancy factor for the phonons of frequency ω and is given by

$$n = [\exp(\hbar\omega/kT) - 1]^{-1}. \qquad (5.10)$$

p is the number of phonons required to bridge the energy gap between the initial and the final energy states involved in the transition. The total decay rate is given by

$$f_{total}(T) = f_r + f_{nr}(T). \qquad (5.11)$$

f_r is the radiative decay rate and is assumed to be temperature independent. It is to be noted that Eq. (5.11) is same as Eq. (5.7) and therefore at this point of the analysis no donor – donor migration is assumed in the system. f_r and $f_{total}(T)$ are taken as the reciprocals of the lifetimes τ_o and τ measured respectively at a very low temperature and at T °K. The value of the only remaining undetermined parameter $f_{nr}(0)$ is chosen for the best fit to the data.

A calculation for non-radiative decay on the basis of the SCC model using Eq.(5.9) was conducted for Cr^{4+}:Y_2SiO_5. The values for S and $\hbar\omega$ were obtained from the shape of the broad band luminescence at 10 °K ($\hbar\omega$ =309.45 cm^{-1} and S=1.9). Also, by definition, $\Delta E = p\hbar\omega$. Since the estimated band gap (the difference between the zero phonon electronic energies) between the $^3E(^3T_2)$ and the $^3A_2$ states is 8631 cm^{-1} in Cr^{4+}:Y_2SiO_5 the predicted value of was 28. However, these calculations predicted the onset of strong non-radiative processes at around 200 °K which is very different from the experimentally observed critical temperature of about 77 °K **[Fig. 23]**. This model, in which the non-radiative process is pictured in terms of the loss

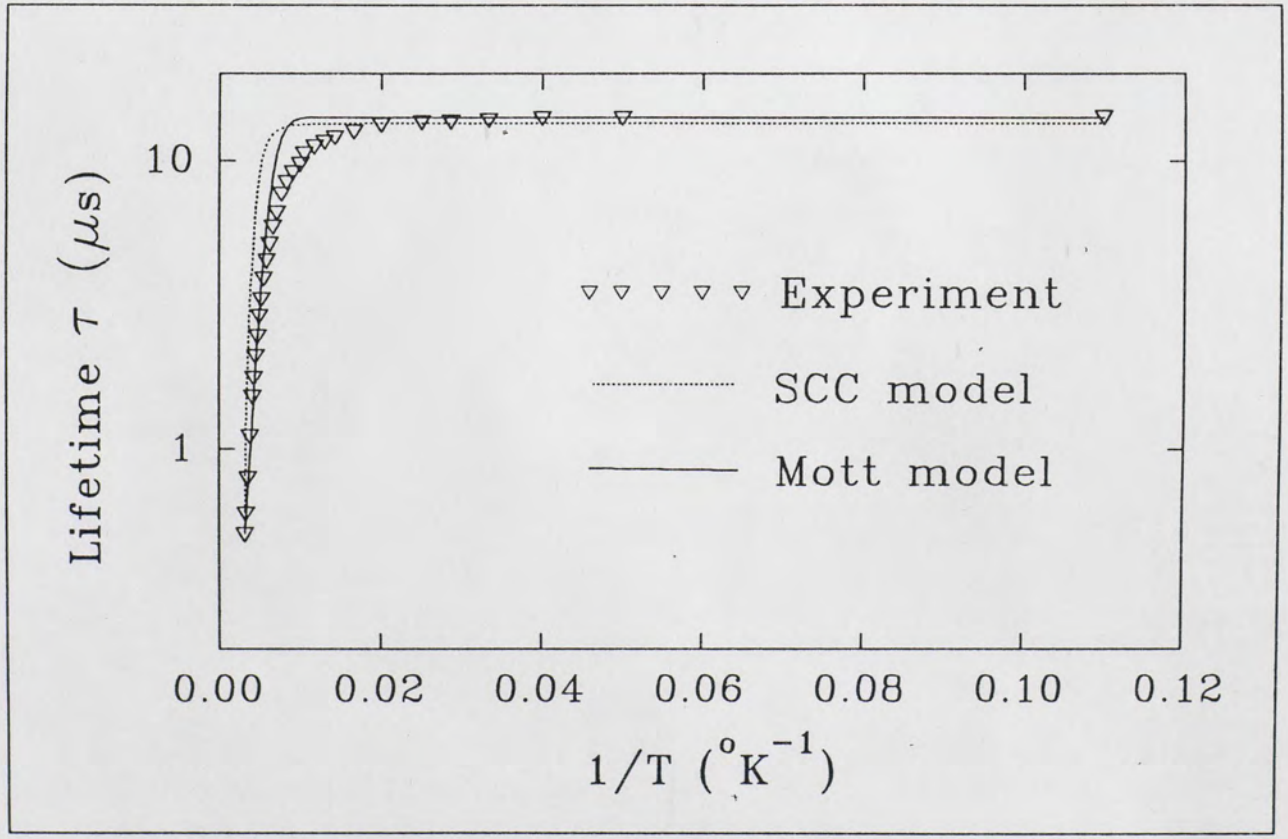

Figure 23. Temperature dependence of lifetime τ of the fluorescence excited by 1064 nm radiation. Theoretical fits are shown for the single configuration coordinate model (dashed line) and Mott's single activation energy model (solid line).

of excitation energy to the sea of lattice phonons[5.5], is therefore not able to account for the strong quenching of the lifetime of Cr^{4+}:Y_2SiO_5 at fairly low temperatures.

To understand the non-radiative decay mechanisms alternative calculations were conducted on the basis of Mott's single activation energy[5.14, 5.15, 5.16] model. Although the agreement with experimental data is fairly good in the high temperature regime, significant differences were observed between the experimental lifetime and that predicted by Mott's single activation energy model in the temperature range below 100 °K [**Fig.23**].

In **Fig.24(a)** we plot $\log[(\tau_0/\tau)-1]$ versus **1/T**. From this figure it is seen that there are two distinct temperature regimes where the dominating non-radiative processes are different. The explanation for this observation is as follows:

Absorption due to the transition from the ground state $^3A_2$ to the state ^1E was not observed. Its absence in absorption is attributed to a very small radiative transition probability between these two states. However, when pumped with intense laser radiation, the transition from ^1E to $^3A_2$ appeared as a sharp line in the emission spectrum at low temperature. This indicated that the energy parabola in the single configuration coordinate diagram corresponding to the ^1E state has a very little offset relative to the ground state ($^3A_2$) parabola. As a result, whatever absorption takes place from the ground state to the ^1E level must also be confined mostly within this sharp line. On the other hand, assuming symmetry of the absorption and the emission spectrum about the zero phonon line, the observed broad-band luminescence spectrum predicts that the absorption from $^3A_2$ to the $^3E(^3T_2)$ should extend down to about 1000 nm. In the configuration co-ordinate diagram the energy parabola for the $^3E(^3T_2)$ state would then correspond to a large offset relative to the ground state parabola as shown schematically in **Fig. 25**. When pumping with 1064 nm laser radiation we excite the Cr^{4+} ions primarily in the higher vibronic levels of the $^3E(^3T_2)$

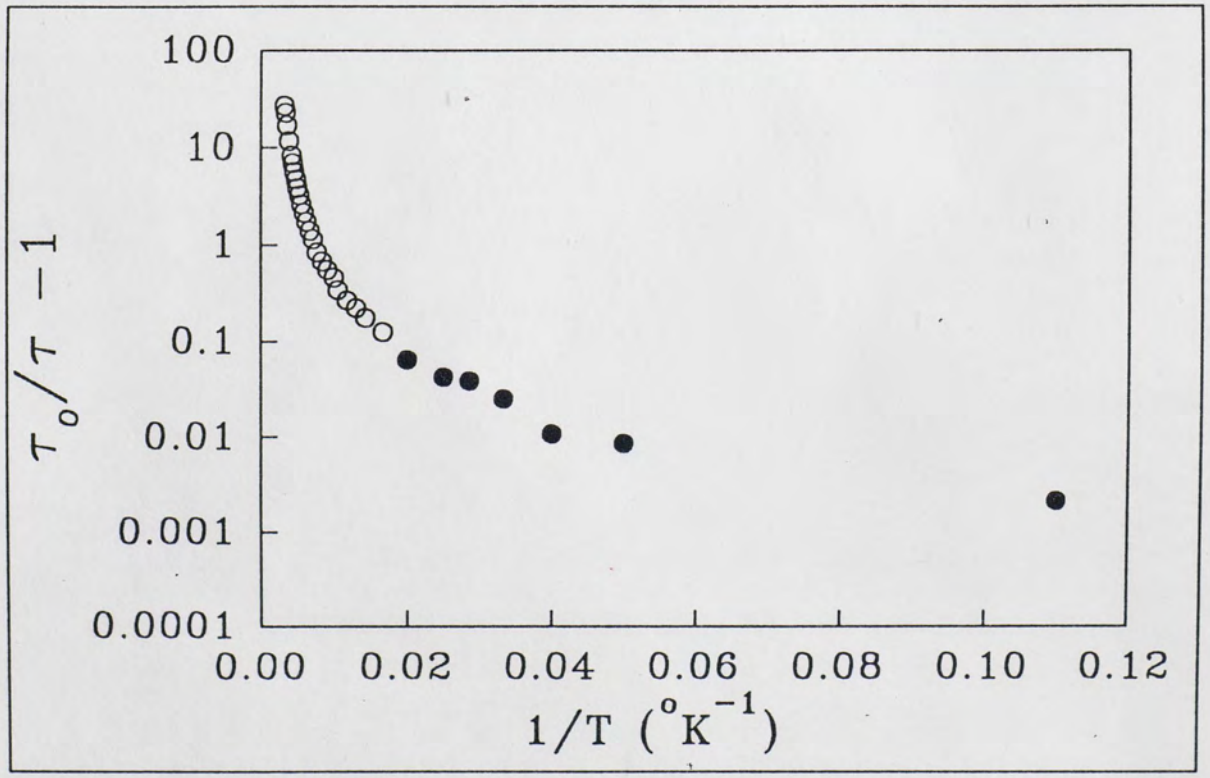

Figure 24(a). $[(\tau_o / \tau) - 1]$ as a function of [1/ T] for the fluorescence decay of Cr^{4+}:Y_2SiO_5 at 1200 nm; (excitation wavelength was 1064 nm).

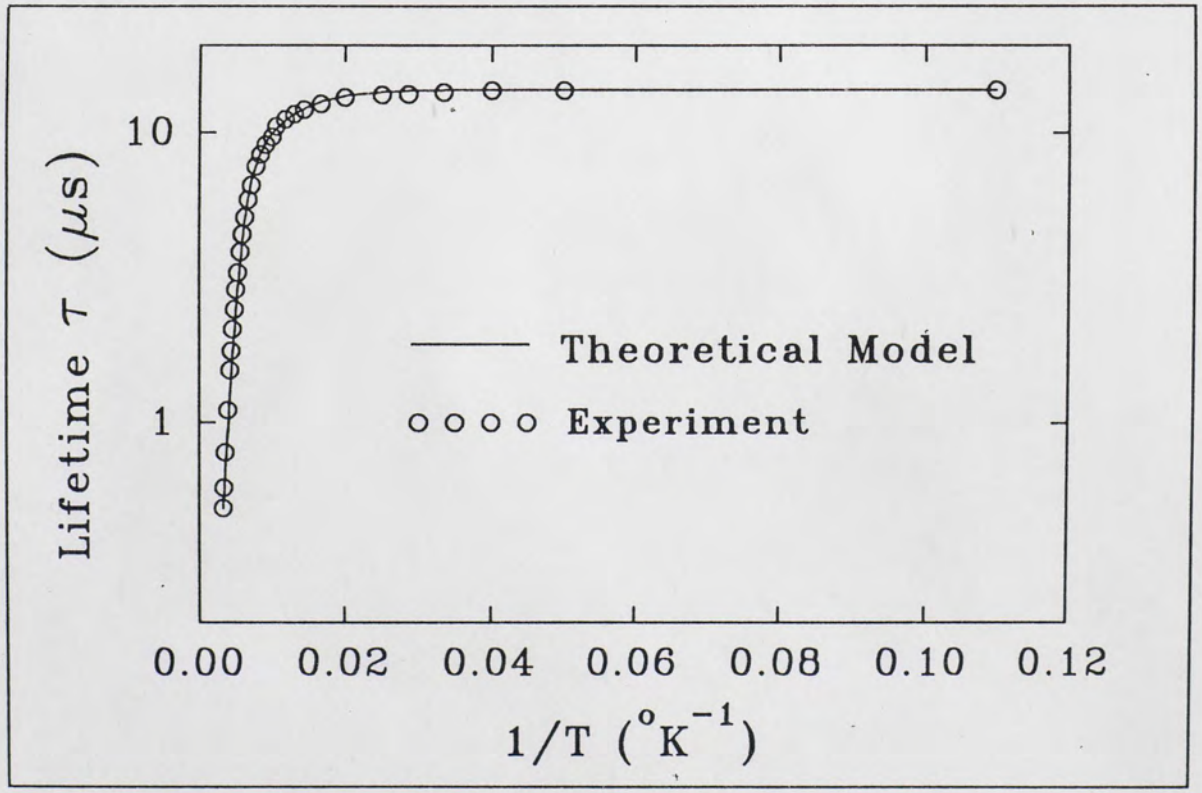

Figure 24(b). Temperature dependence of fluorescence lifetime τ (hollow circles) of $Cr^{4+}:Y_2SiO_5$ compared with the theoretical prediction based upon the model developed in this paper (solid line). The fluorescence was excited by 1064 nm radiation.

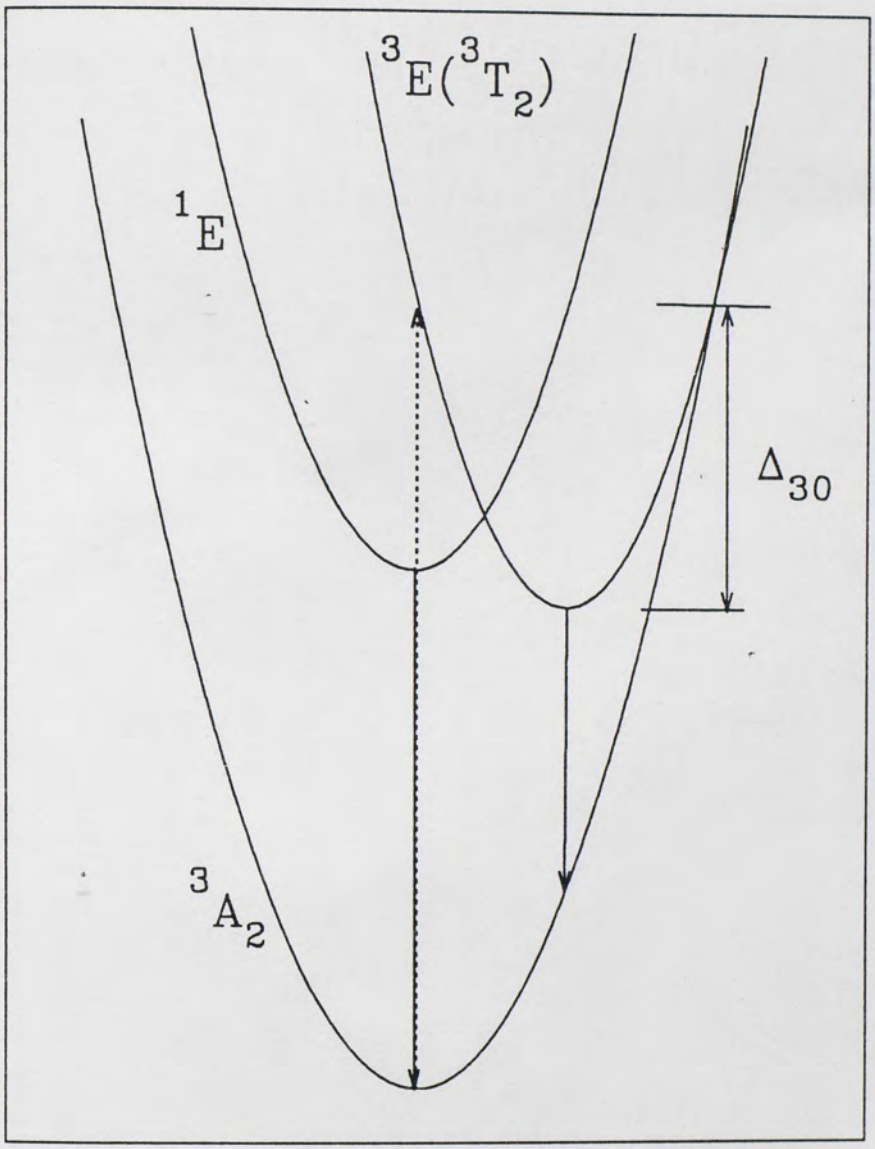

Figure 25. Schematic diagram of the single configuration coordinate energy parabolas of the Cr^{4+} ion in tetrahedral (C_{3V}) site in Y_2SiO_5. The dashed arrow represents the absorption from the ground state to the $^3E(^3T_2)$ state and the solid arrows represent the downward radiative transitions from the ^1E and $^3E(^3T_2)$ states.

states. As these excited ions relax rapidly to the minimum of the energy parabola of the $^3E(^3T_2)$ states, they pass through the cross over point of the $^3E(^3T_2)$ and ^1E parabolas [**Fig.25**]. As a result, some of the excited ions relax non-radiatively to the ^1E state while the rest relax to the lowest vibronic levels of the $^3E(^3T_2)$ state. Because of the close proximity of the electronic energy levels corresponding to the ^1E and the $^3E(^3T_2)$ states there is strong mixing of these two states resulting in thermalization of their populations even at fairly low temperatures[5.17]. This thermalized combination of $^3E(^3T_2)$ and ^1E states therefore decay with a single life time given by[5.18]:

$$1/\tau = P_1 / \tau_1 + P_3 / \tau_3 \qquad (5.12)$$

$$P_1 = 2\exp(-\Delta/kT) / Z \qquad (5.13)$$

$$P_3 = 6 / Z \qquad (5.14)$$

$$Z = 2 + 6\exp(-\Delta/kT). \qquad (5.15)$$

P_1 and P_3 are the singlet (^1E) and triplet ($^3E(^3T_2)$) Boltzmann populations respectively and τ_1, τ_3 are their respective lifetimes. Δ is the energy gap between the zero phonon electronic energy levels of the $^3E(^3T_2)$ and the ^1E states.

Now, the initial populations in the ^1E states can decay by radiative transition to the ground state, or transfer their energy to neighboring Cr^{4+} ions. The ion-ion transfer may proceed in two possible ways: (i) ^1E to ^1E migration by resonant transfer and (ii) ^1E to $^3E(^3T_2)$ phonon assisted transfer to a nearest neighbor followed by $^3E(^3T_2)$ to $^3E(^3T_2)$ migration. The first process is temperature independent while the second depends on temperature. Referring to the Fig.25(a) we note that the ^1E to $^3E(^3T_2)$ transfer most favorably takes place between the lowest electro-vibronic levels in the two states which are resonant with each other (designated as **u** and **v** in **Fig.26(a)**). Therefore, if the ion is initially in the ^1E state the corresponding transfer rate will be proportional to $\exp[-\Delta_{13}/kT]$, where Δ_{13} is the energy of the electro-vibronic energy level u of the ^1E state relative to the zero phonon electronic energy of that state. On the

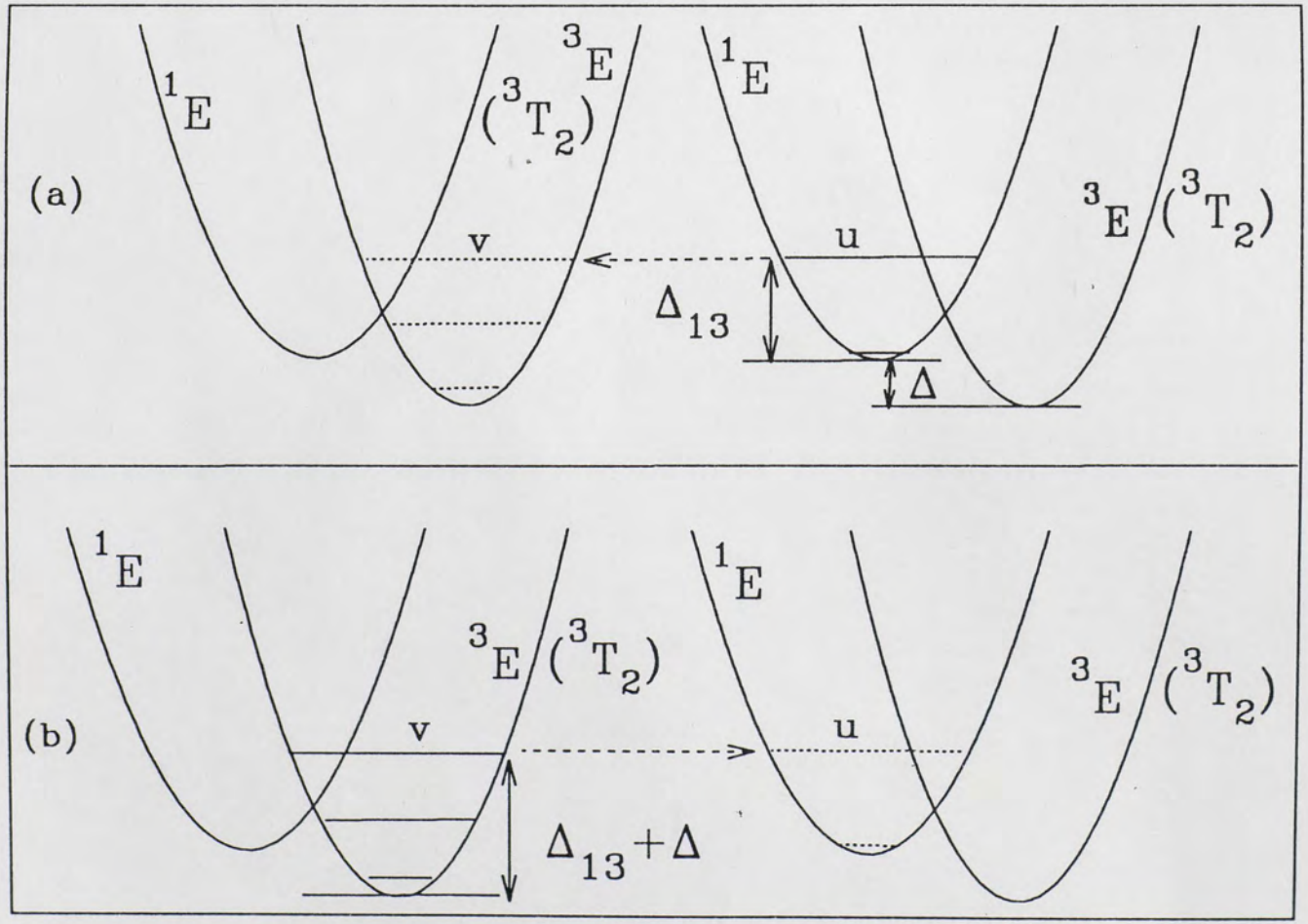

Figure 26. Energy transfer describing inter-ionic energy transfer from (a) ^1E to $^3E(^3T_2)$, and (b) $^3E(^3T_2)$ to ^1E states of Cr^{4+} ions.

other hand, if the ion is initially in the $^3E(^3T_2)$ state the ion-ion transfer may proceed by (i) $^3E(T_2)$ to $^3E(^3T_2)$ resonant transfer and migration, or (ii) $^3E(^3T_2)$ to ^1E phonon assisted energy transfer to a nearest neighbor followed by ^1E to ^1E migration. The $^3E(^3T_2)$ to ^1E transfer rate is proportional to $\exp[-(\Delta_{13}+\Delta)/kT]$ (**Fig. 26(b)**). In a significant fraction of the above ion-ion energy transfer events leading to rapid migration, the excitation energy will eventually be lost to traps (or killer centers)[5.19] which quench the fluorescence intensity and lifetime of the excited Cr^{4+} ions. One can express the resulting singlet and the triplet lifetimes as

$$1/\tau_1 = 1/\tau_{1R} + A + C_{13}\exp[-\Delta_{13}/kT] \quad (5.16)$$

$$1/\tau_3 = 1/\tau_{3R} + B + C_{31}\exp[-(\Delta_{13}+\Delta)/kT] + C_{30}\exp[-\Delta_{30}/kT] \quad (5.17)$$

where A and B are the rate of loss of the singlet and triplet excitations to killer centers via resonant ion-ion migration from ^1E to ^1E and $^3E(^3T_2)$ to $^3E(^3T_2)$ states respectively. The third terms on the right hand side of Eqs. (5.16) and (5.17) represent the rates of loss of singlet and triplet excitations to killer centers via ion-ion migrations initiated by non-resonant energy transfers from the singlet state to the triplet state and *vice versa*. τ_{1R} and τ_{3R} are the radiative lifetimes of the ^1E and the $^3E(^3T_2)$ states respectively. The last term in Eq. (5.17) represents the non-radiative decay of the $^3E(^3T_2)$ state to the ground state, Δ_{30} being the Mott-activation energy for the process. Thus we can express the resultant lifetime of the excited system as

$$1/\tau = P_1[1/\tau_{1R} + A + C_{13}\exp(-\Delta_{13}/kT)] + P_3[1/\tau_{3R} + B + C_{31}\exp(-(\Delta_{13}+\Delta)/kT) + C_{30}\exp(-\Delta_{30}/kT)] \quad (5.18)$$

and substituting from Eq. (5.13), (5.14) and (5.15)

$$1/\tau = [6(1/\tau_{3R} + B) + 2(1/\tau_{1R} + A)\exp(-\Delta/kT) + (2C_{13} + 6C_{31})\exp(-(\Delta_{13}+\Delta)/kT) + 6C_{30}\exp(-\Delta_{30}/kT)]/Z. \quad (5.19)$$

If Δ is very small then Eq. (5.19) can be written in a simplified form:

$$1/\tau = 1/\tau_0 + C^*\exp(-\Delta_{13}/kT) + D^* \exp(-\Delta_{30}/kT) \quad (5.20)$$

where

$$1/\tau_0 = \{6(1/\tau_{3R} + B) + 2(1/\tau_{1R} + A)\} / 8 \quad (5.21)$$

$$C^* = (2C_{13} + 6C_{31})/ 8 \quad (5.22)$$

$$D^* = (6/8)C_{30} \quad (5.23)$$

The radiative transition from ^1E to $^3A_2$ is spin-forbidden and the corresponding radiative lifetime τ_{1R} for such transitions are usually of the order of a few tens of milliseconds. The spin allowed multiphonon transition from the $^3E(^3T_2)$ to the $^3A_2$ ground state is expected to have lifetime τ_{3R} of the order of tens of microseconds but could be much longer if the transition is symmetry forbidden. In general $1/\tau_{3R} >> 1/\tau_{1R}$. 'A' and 'B', on the other hand, are expected to be fast processes and will dominate the decay rate at the low temperatures. This would also explain the observed short lifetimes of the Cr^{4+} near infrared luminescence even at the lowest temperature tested, 9.1 °K. As the temperature is increased (below 100 °K) the contribution from the migration initiated by the phonon–assisted transfer processes between ^1E and $^3E(^3T_2)$ becomes significant while the Mott-non-radiative transfer from the $^3E(^3T_2)$ to the $^3A_2$ ground state is still very small. As a result the intensity of the sharp line decreases until at about 77 °K it is no longer observed. The lifetimes of the excited states decrease slowly with increasing temperature . [**Fig.24(a)**: filled circles]. As the temperature is increased further the depopulation of the $^3E(^3T_2)$ state occurs also by non-radiative decay to the ground state across the cross-over point of the energy parabolas of the $^3E(^3T_2)$ and $^3A_2$ states (drawn schematically in the single configuration coordinate formalism in **Fig. 25**). This process corresponds to the standard Mott-model with a larger activation energy and dominates the non-radiative decay at the higher temperatures [**Fig.24(a)**: open circles]. A theoretical fit to the

temperature dependent lifetimes using Eq.(5.19) is shown in Fig.24(b). For very small value of Δ the fitting basically involves the optimization of only two parameters, namely C* and D*, the values for Δ_{13} and Δ_{30} being available approximately from the slopes of the curve in Fig.24(a) at very low and high temperatures respectively. The parameters for the fit shown in the present work are:

$$\Delta_{13} = 78.4 \text{ cm}^{-1} \text{ and } \Delta_{30} = 784 \text{ cm}^{-1}$$

$$(A + 1/\tau_{1R}) = 0.1788 \ \mu s^{-1} \text{ and } (B + 1/\tau_{3R}) = 0.07095 \ \mu s^{-1},$$

$$\tau_{nr(13)} = 5.0 \ \mu s \text{ and } \tau_{nr(30)} = 11.75 \text{ ns},$$

where $\tau_{nr(13)} = 8/(2C_{13} + 6C_{31})$ and $\tau_{nr(30)} = 1/C_{30}$.

At very low temperature the life time is dominated by the rate $(B + 1/\tau_{3R})$.

With 532 nm pumping the observed emission spectrum at low temperature extends beyond the 1146 nm sharp line to shorter wavelengths. The sharp line at 1146 nm in this case can be resolved only under high resolution settings of the detection system **[Fig.27(a)]**. It is to be noted that with the resolution of the system that showed the strong sharp line at 1146 nm for 1064 nm pumping [Fig.3(a)] we could not resolve this line when pumping with 532 nm radiation[5.20] as shown in Fig.3(b). The decay of the fluorescence above 1146 nm was found to be non-exponential and can be expressed as the sum of two exponential functions with different decay rates. **Fig.28** shows the temperature dependence of both the initial and slower components of the decay measured at 1200 nm. The longer component has been identified as the one that also results when the crystal is excited by 1064 nm radiation. We also measured the life time at wavelengths shorter than 1146 nm at 10 ^{o}K. **Fig. 27(b)** shows the decay profiles at 10 ^{o}K measured at 1010 nm and 1200 nm respectively; the excitation wavelength was 532 nm. The fluorescence at wavelengths less than 1146 nm was found to decay following a single exponential function with a lifetime of about 3.5 μs at 10 ^{o}K. This is the same lifetime as the shorter initial component observed in the decay at 1200 nm. As

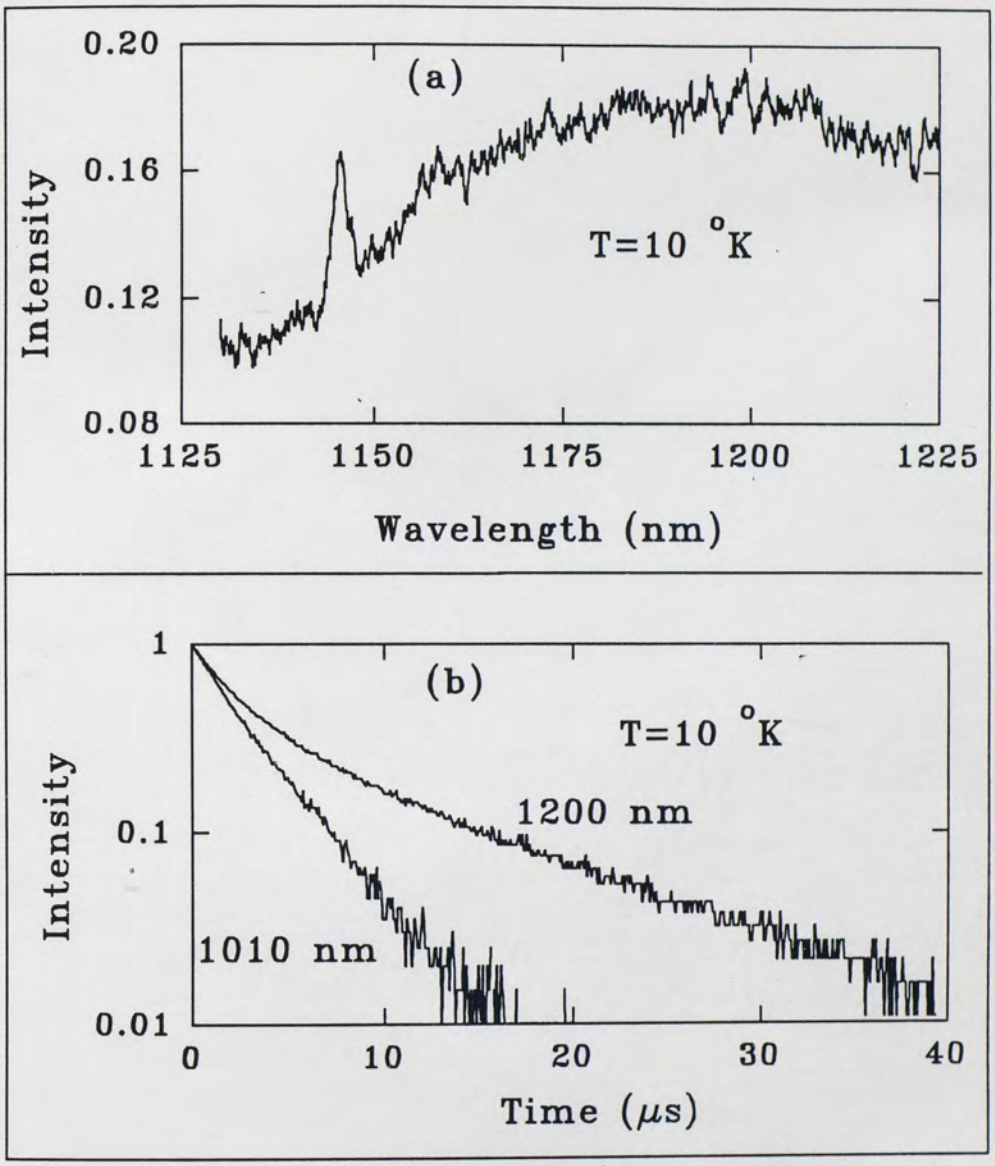

Figure 27. Fluorescence properties of Cr^{4+}:Y_2SiO_5 due to excitation at 532 nm: (a) high resolution fluorescence spectrum at 10 °K shows the sharp line at 1146 nm, (b) fluorescence decays at 1200 nm and 1010 nm.

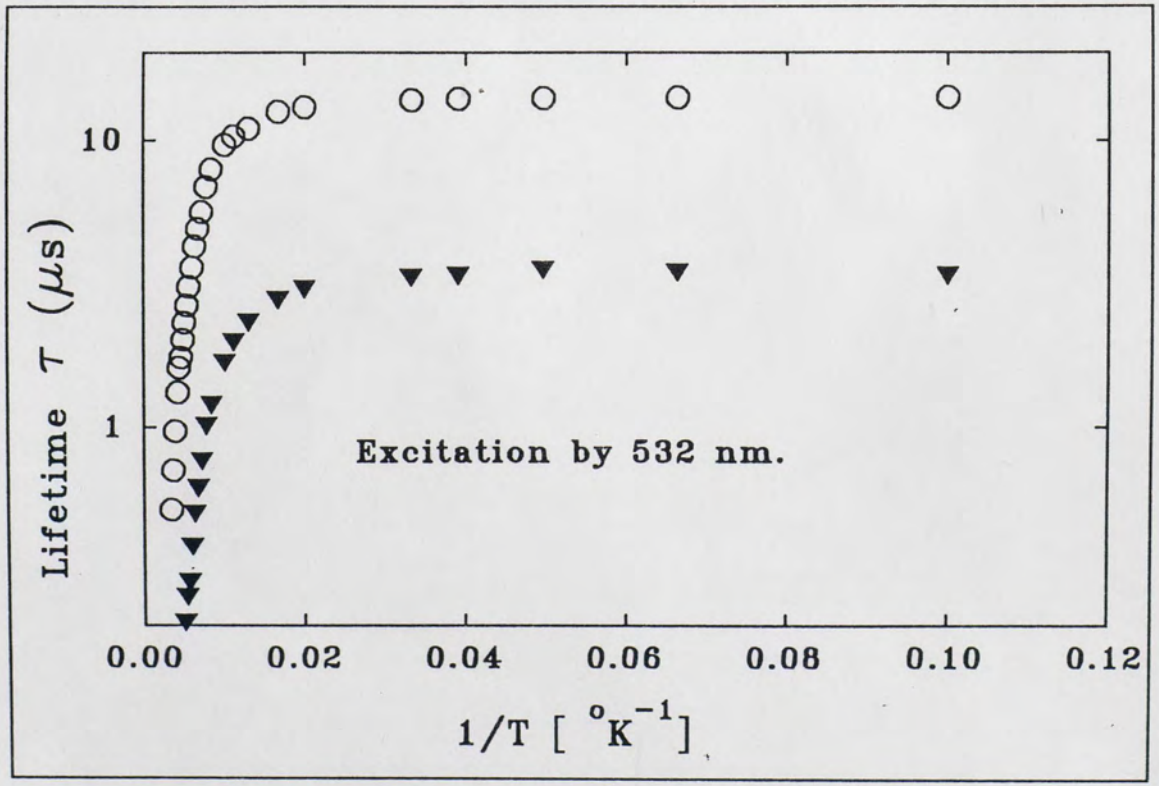

Figure 28. Temperature dependence of lifetime of the initial (solid triangles) and the slower component (hollow circles) of the fluorescence measured at 1200 nm due to excitation by 532 nm radiation.

a result, it indicates the presence of a second type of emission with a shorter lifetime starting from higher energies but overlapping with the emission due to the transition from the mixed $^3E(^3T_2)$, ^1E states to the ground state $^3A_2$. The origin of this second emission is not yet exactly determined but we suspect that it results from a transition between two excited states similar to the red emission from Ni^{2+} in MgF_2 [5.21].

The application of the model described above to Cr:Forsterite also clears up many of the uncertainties and inconsistencies observed in earlier work (temperature dependence of lifetime[5.22]; crystal field splitting[5.23, 5.24] of $^3T_1$ and $^3T_2$; crystal field parameters[5.25]) on Cr^{4+} in that crystal.

Detailed analysis of the absorption spectrum of Cr^{4+}:Mg_2SiO_4 have been conducted by Verdun *et. al.* [5.3] and Moncorge *et. al.*[5.22] on the basis of a distorted tetrahedral site for the Cr^{4+} site. The spectrum is characterized by a strong polarization dependence in three different directions. Moncorge calculated the energy level for a T_d symmetry using crystals field parameters $Dq = 916\ cm^{-1}$, $B = 460\ cm^{-1}$ and $C = 2790\ cm^{-1}$. This corresponds to a strong crystal field with $10Dq/B = 19.9$ and puts the system in the neighborhood of the ^1E, $^3T_2$ crossover point in the Tanabe-Sugano diagram[5.1]. Verdun [5.3], on the other hand, performed his calculation for a C_s local symmetry with $10Dq/B = 16.11\ cm^{-1}$. The bands at 570, 650 and 740 nm were assigned to the transitions from the ground state to the crystal field components (CFC) of the $^3T_1(^3F)$ state and the bands in the infrared were assigned to the transitions to the CFC of the $^3T_2(^3F)$ state. This implies an energy gap of the order of $4000\ cm^{-1}$ between the highest and the lowest crystal field components for the $^3T_1$ state, which incidentally is of the same order as the gap between the crystal field components of the $^3T_1$ state in Cr^{4+}:Y_2SiO_5. Table 5.2 shows the electronic energy levels of the Cr^{4+} ion in Cr:Forsterite as given in Refs. [5.3], [5.22] and [5.25]. Refs. [5.3] and [5.22] agree with each other while Ref. [5.25] significantly differs in the energy level assignments. The

TABLE 5.2

ENERGY LEVELS AND CRYSTAL FIELD PARAMETERS
OF Cr^{4+} IN Cr:FORSTERITE

	Energy Levels *w.r.t.* $^3A_2$ ground state in cm^{-1} *		
Energy States	Ref. 5.25	Ref. 5.22	Ref. 5.3
$^3T_1(^3P)$	26800 (373 nm)	20921 (477 nm)	24064 (415 nm)
$^3T_1(^3F)$	15150 (660 nm)	13459 (743 nm)	15358 (651 nm)
$^3T_2(^3F)$	9150 (1092 nm)	9160 (1092 nm)	9990 (1001 nm)
^1E	16245 (615.5 nm)	9126 (1095 nm)	10255 (975 nm)
$^1A_1$	Not given	15255 (655.5 nm)	17628 (567.3 nm)
$^1T_2$	28700 (348 nm)	18163 (550.57 nm)	20143 (496 nm)
$^1T_1$	Not given	16580 (493.5 nm)	23094 (433 nm)
Crystal field parameters			
10Dq/B	9.43	19.91	16.11
B	970 cm^{-1}	460 cm^{-1}	620 cm^{-1}
Dq	915 cm^{-1}	916 cm^{-1}	999 cm^{-1}
C	3980 cm^{-1}	2790 cm^{-1}	2728 cm^{-1}

* The wavelengths of the corresponding transitions are shown in parentheses (in nm).

difference arises because of a much weaker crystal field strength assumed for the calculation in Ref. [5.25]. We note the absence of the expected sharp line structure due to the $^3A_2 - {}^1E$ transition at the predicted value of 615.5 nm in Ref. [5.25]. Moncorge, onthe other hand, predicted the ^1E level 9126 cm^{-1} above the $^3A_2$ level. This would result in an absorption band at 1095 nm which is close to the observed sharp and strong line at 1092 nm. This sharp line appears in the absorption[5.22], emission [Figs.5(e), 5(f)] as well as the excitation spectra and has been tentatively attributed to the zero phonon transition between the $^3A_2$ and $^3T_2$ levels of the Cr^{4+}. Moncorge has also shown that this sharp line can actually be resolved into three components. The temperature dependence of the relative intensities of the components of this triplet was reported to be non-Boltzmann by Moncorge *et. al.*[5.22]. It was pointed out that this fact ruled out the possibility of these three fine structure components being due to the spin-orbit splitting of the $^3T_2$ level alone. However, since a strong crystal field environment as suggested by Moncorge and Verdun would put the ^1E level extremely close to the $^3T_2$ level the observed emission spectrum in that case will be the sum of the transitions to the ground state from both these levels. At least one of the components in the 1192 nm sharp line triplet could then be interpreted as being due to the transition from the ^1E level and another as the zero phonon line of the $^3T_2$ - $^3A_2$ transition. Moncorge, however, ruled out this possibility on the basis of their failure to prove a thermalization process between the ^1E and $^3T_2$ levels[5.22]. In that work an attempt was made to fit the thermal variation of the infrared fluorescence lifetime with expressions of the type

$$1/\tau = [1/\tau_1 + 1/\tau_2 \exp(\Delta/kT)] / [1 + \exp(\Delta/kT)] \qquad (5.24)$$

where τ_1 and τ_2 are the radiative life times of the ^1E and $^3T_2$ levels respectively and Δ is the difference between the electronic energies of these two states. However, reportedly no meaningful fitting with any physical significance was obtained. We have verified that indeed Eq.(5.24) by itself does not describe the temperature variation of

lifetime of the NIR fluorescence of Cr:Forsterite. However, the fact that Eq.(5.24) does not fit the experimental data by itself can not rule out the possibility of the contribution to the total fluorescence from both ^1E and $^3T_2$ levels at the same time. We note that an expression of the form given by Eq.(5.24) does not take into account the non-radiative decay of the population from the excited states directly to the ground state nor does it take into consideration other processes of energy transfer which may depopulate the excited states. A complete expression for the temperature dependent lifetime of the coupled excited states ^1E and $^3T_2$ must be derived by considering all the significant processes involved in the dynamics of the system. Eq.(5.19), which we have already discussed in regards to the decay of the near infrared fluorescence of $Cr^{4+}:Y_2SiO_5$, was derived precisely by such an approach. As in $Cr^{4+}:Y_2SiO_5$, the emitting states are ^1E and the crystal field components of the $^3T_2$ state. However, in this case the $^3E(^3T_2)$ level of the C_{3V} symmetry splits into two components $^3A'[^3E(^3T_2)]$ and $^3A''[^3E(^3T_2)]$ when the Cr^{4+} site symmetry is lowered further to C_s. The splitting of these crystal field components in the C_s symmetry, derived from the $^3E(^3T_2)$ level in the C_{3V} symmetry, are predicted to be relatively small[5.3]. Assuming sufficiently small splitting of this level we can consider the two levels $^3A'[^3E(^3T_2)]$ and $^3A''[^3E(^3T_2)]$ as a single 6-fold degenerate band for the purpose of describing the fluorescence mechanism and describe it simply as $^3E(^3T_2)$. A theoretical fit to the temperature variation of the near infrared fluorescence lifetime of $Cr:Mg_2SiO_4$ at 1200 nm using the simplified form of the Eq.(5.19), which is the Eq.(5.20), is shown in **Figure-29(b)**. As in the case of $Cr^{4+}:Y_2SiO_5$ this is essentially a two parameter fitting procedure, the approximate values of the parameters Δ_{13} and Δ_{30} being available from the slopes of the $[(\tau_0/\tau) - 1]$ -Vs- **[1/T]** curve at the low and the high temperature regimes respectively (**Fig.29(a)**). We note that the Eq.(5.20) corresponds to a very small value of Δ (nearly equal to zero). The parameters corresponding to the fit shown in Fig.29(b) are

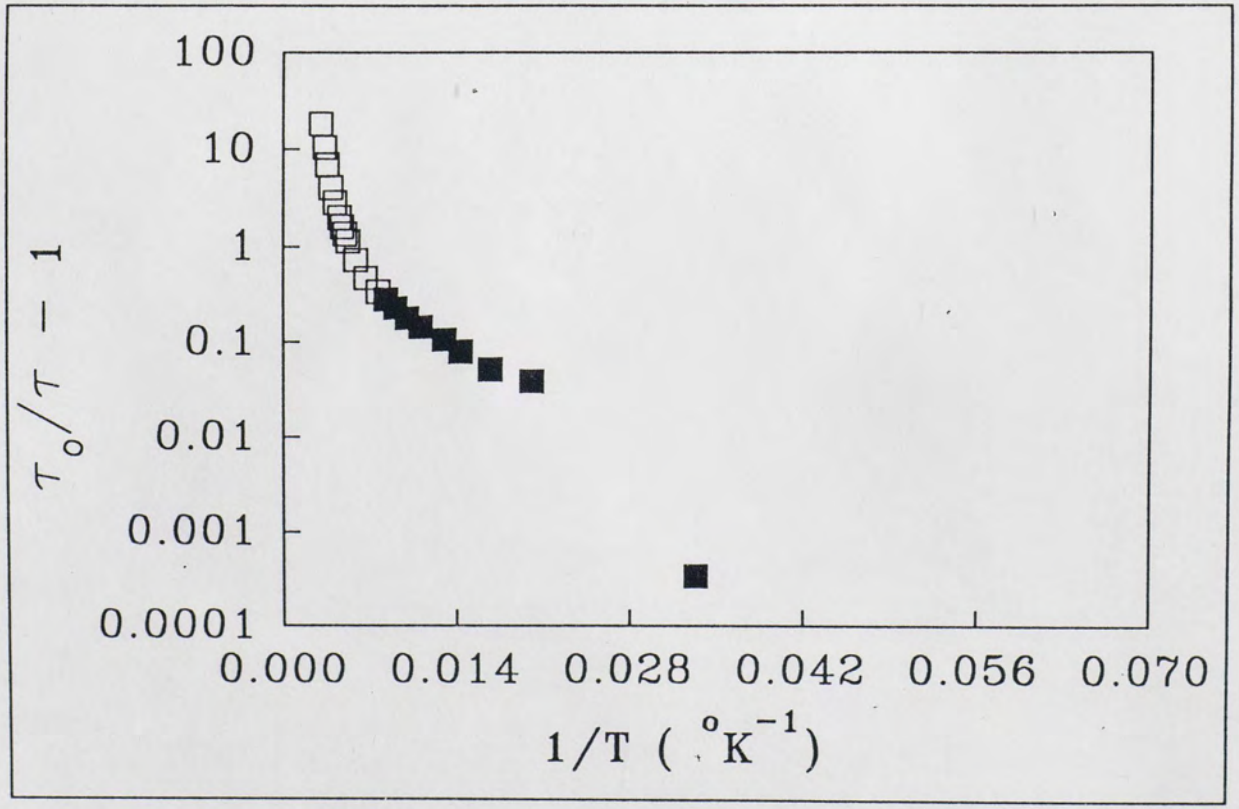

Figure 29(a). $[(\tau_o / \tau) - 1]$ as a function of [1/ T] for the fluorescence decay of Cr:Mg_2SiO_4 at 1200 nm; (excitation wavelength was 1064 nm).

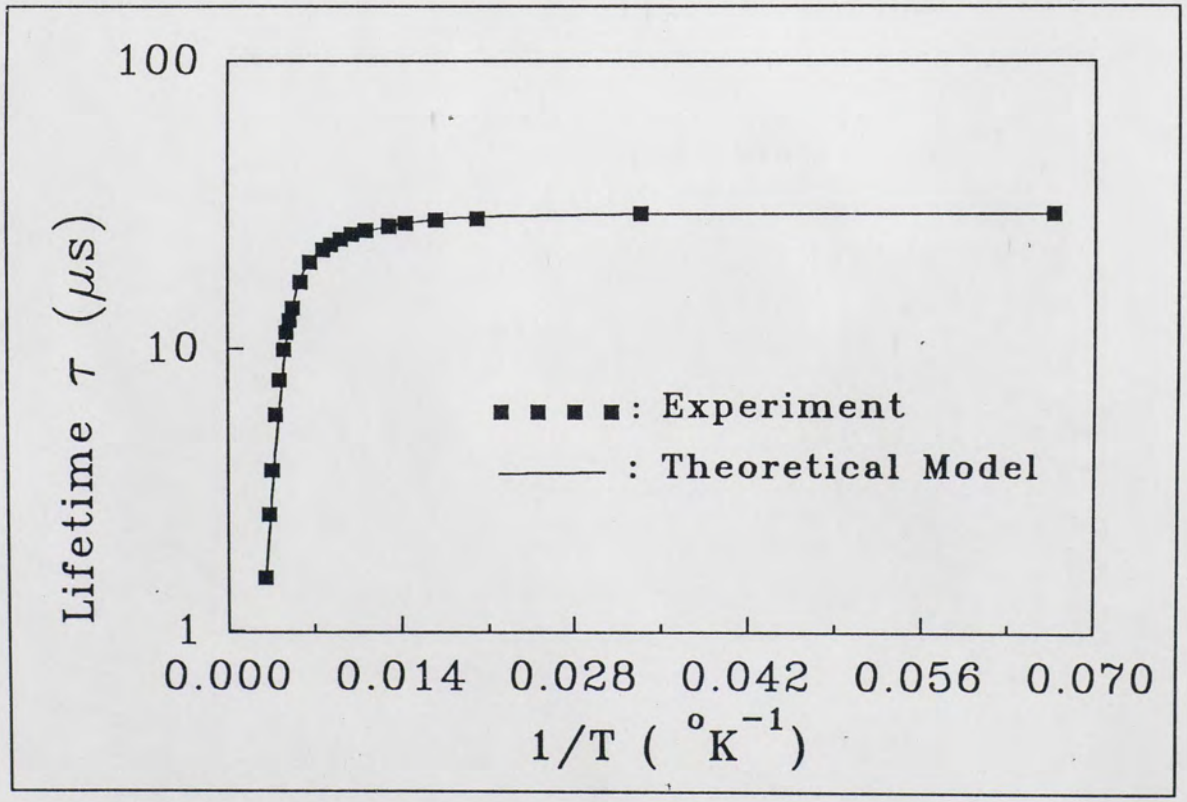

Figure 29(b). Temperature dependence of fluorescence lifetime τ (filled squares) of Cr^{4+}:Mg_2SiO_4 compared with the theoretical prediction based upon the model developed in the present work (solid line). The fluorescence was excited by 1064 nm radiation.

$1/\tau_0 = \{6(1/\tau_{3R} + B) + 2(1/\tau_{1R} + A)\} / 8 = 0.0337\ \mu s^{-1}$,

$C^* = (2C_{13} + 6C_{31})/8 = 0.0525\ \mu s^{-1}$,

$D^* = (6/8)C_{30} = 68.25\ \mu s^{-1}$,

$\tau_{nr(13)} = 1/C^* = 19.04\ \mu s$,

$\tau_{nr(30)} = 1/C_{30} = 10.99\ ns$,

$\Delta_{13} = 142.06\ cm^{-1}$,

$\Delta_{30} = 1079.19\ cm^{-1}$.

The excellent fit obtained with this equation tends to confirm the hypothesis that the $^1E - {}^3A_2$ and $^3E(^3T_2) - {}^3A_2$ zero phonon lines are very close together, being the components of the triplet observed by Moncorge[5.22] at around 1092 nm. This would also explain the non-Boltzmann character of the components of this triplet as reported by Moncorge in reference [5.22].

The effect of the Cr^{3+} ions on the spectroscopic properties of Cr^{4+} in forsterite has been the subject of considerable uncertainties. In order to get a little more insight into this problem chromium doped forsterite grown under pure nitrogen and partly oxygen atmosphere were studied. It was found that inclusion of chromium in the tetravalent state is facilitated by an oxidizing growth atmosphere. **Figs. 4 and 5.** in Chapter 3 show the room temperature luminescence spectra of Cr:Forsterite samples grown under different atmosphere when pumped by 532 nm radiation. It is seen that for certain orientations in the sample grown under an oxidizing atmosphere (sample#1) the 1200 nm band, attributed to the Cr^{4+}, is significantly more intense than the 900 nm band which is attributed to the Cr^{3+}. In the sample grown under a pure nitrogen atmosphere (sample#2) the Cr^{4+} luminescence band is weaker than the Cr^{3+} band in all polarization. This is due to higher concentration of Cr^{4+} ions compared to Cr^{3+} ions in the sample grown in oxygen atmosphere as compared to the sample grown in a pure nitrogen atmosphere. This also affects the fluorescence decay as can be seen in **Fig.30.**

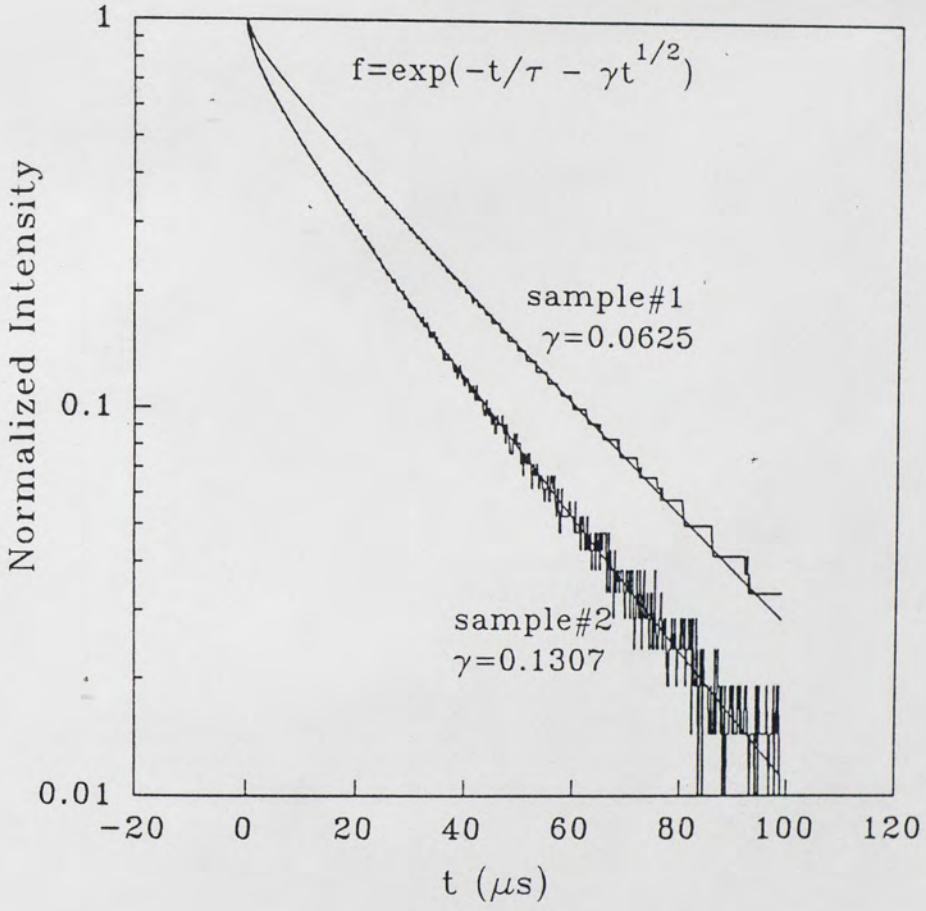

Figure 30. Temporal profile of the fluorescence decay of Cr:Mg_2SiO_4 samples grown under different atmospheres measured at 15 ^{o}K. The Pump wavelength was 1064 nm and fluorescence was measured at 1200 nm. The smooth lines are the theoretical fit using Forster-Dexter formula for dipole-dipole donor-acceptor energy transfer.

The fluorescence decay at 1200 nm in both the samples follow functional forms indicative of dipole-dipole energy transfer mechanism (Forster- Dexter). The values of γ for the fluorescence decay at 1200 nm at 10 ^{o}K for the samples #1 and #2 were 0.0625 and 0.1307 respectively. Assuming same donor-acceptor dipole-dipole interaction in both the samples the above values suggest a higher concentration of acceptor centers in the sample #2. It is to be noted that this sample also had a relatively higher concentration of Cr^{3+}. However, there is no direct evidence that the Cr^{3+} ions are the acceptors in this case since no initial rise was observed in the temporal profile of the fluorescence decay of the Cr^{3+}. It is suspected that defects created in the crystal in the doping process may be the non luminescent traps to which the Cr^{4+} excitation energy is eventually lost. This hypothesis is also supported by the observation that the concentration of the acceptor centers appears to be higher in the sample which also had a higher Cr^{3+} concentration. The charge imbalance between the Cr^{3+} ions and the Mg^{2+} ions which they substitute results in the formation of defects in the crystal.

The polarized absorption spectrum of Cr^{4+}:Ca_2SiO_7 indicates that the Cr^{4+} site symmetry is C_{3V}. Allik *et. al.*[5.26] reported that the fluorescence spectrum of this crystal ranges approximately from 1000 nm to 1800 nm peaking near 1250 nm. In the present work it was observed that this broad spectrum actually consists of two bands. The fluorescence band with peak at 1400 nm was unstable and was annealed by prolonged irradiation with intense laser radiation at 1064 nm (**Fig. 7**). The temporal profiles of the fluorescence decay measured in the two bands at 1428 nm and 1200 nm are shown in **Fig.8(a)**. The decay at 1200 nm follows a functional form that indicates a dipole-quadrapole energy transfer mechanism according to the Forster-Dexter model **[Fig.8(b)]**. In this case also the nature of the acceptor center is unknown and needs further investigation.

The other crystals studied in this work did not show any special features leading to further insight into the mechanisms involved in the optical properties of the Cr^{4+} substituted into tetrahedral site in crystalline hosts. From the perspective of crystal field engineering of Cr^{4+} doped crystals for laser action these crystals appear to be of no particular interest at this moment. Preliminary spectroscopic data on these crystals are presented in Chapter 3.

CHAPTER 6

LASER PERFORMANCE OF $Cr^{4+}:Y_2SiO_5$

In this chapter the laser properties of $Cr^{4+}:Y_2SiO_5$ are presented. Two interesting characteristics were observed in this new laser: (1) the free running output spectrum depends on the pump wavelength, and (2) the output energy indicates some form of saturation at higher absorbed energies.

The laser experiment with $Cr^{4+}:Y_2SiO_5$ is sketched in **Fig.31**. It is a conventional longitudinal laser pumped laser cavity with a flat high reflector (R=99.9 % @ 1180-1300 nm) and a curved output coupler (radius of curvature 30 cm; R=98 % @ 1180-1300 nm) placed 20 cm apart. The crystal used for the experiment was a parallelepiped with dimensions 5.4 x 6.65 x 12.5 mm^3 and was mounted on the cold finger of a liquid nitrogen dewar (Kadel Engineering) with fused silica windows. The crystallographic axes of the crystal used in this experiment were however not properly oriented as in the sample used to measure the polarized absorption spectra (**Fig.2**). Therefore the absorption spectrum of the laser crystal showed contribution from all orientations (**Fig. 32**). The end faces of the crystal (normal to the longest side) as well as the fused silica windows of the liquid nitrogen dewar used in this experiment were anti-reflection coated between 1200 and 1300 nm. The pump beam from a pulsed Q-switched laser (Nd:YAG or Cr:LiSAF) was focused before the high reflecting mirror and longitudinally pumped the crystal. The intensity of the pump beam was varied by the combination of polarizers P1 and P2; the orientation of the polarizer P2 was kept fixed throughout the experiment. The laser pulse from the $Cr^{4+}:Y_2SiO_5$ crystal was

detected by a fast Germanium photodiode placed behind the outcoupler and appropriate filters to block out the residual pump beam.

The laser performance characteristics of the $Cr^{4+}:Y_2SiO_5$ crystal at 77 ^oK are summarized in Table 6.1. However lasing at temperatures up to 257 ^oK was demonstrated.

Fig. 33 is a plot of the single pulse output energy from the $Cr^{4+}:Y_2SiO_5$ laser versus the absorbed energy for different pump wavelengths. With 1064 nm pumping (pulse duration 15 ns, beam diameter ~ 400 μm) the slope efficiency of the $Cr^{4+}:Y_2SiO_5$ laser decreased drastically as the absorbed energy was increased above 1.0 mJ, showing a strong saturation behavior in the laser output. Similar saturation behavior is observed for 532 nm pumping (pulse duration 15 ns, beam diameter ~ 400 μm) when the absorbed energy is higher than 3.0 mJ. When pumped with 840 nm (pulse duration 35 ns, beam diameter ~ 400 μm), on the other hand, the slope efficiency changes discontinuously to a smaller value at about 2.5 mJ of absorbed energy and the crystal continues to lase at this efficiency up to absorbed energy of about 7.5 mJ. The cause of this saturation behavior is yet to be determined.

The free running spectra due to 1064 nm pumping is distinct from that due to 532 nm pumping. The broad-band pumping at 840 nm produces roughly the same output free running laser spectrum (**Fig. 34**) as that due to 532 nm pumping. The pump wavelength dependence of the $Cr^{4+}:Y_2SiO_5$ laser indicates the existence of two types of emission in the NIR resulting from different excitations. This is consistent with the observation of the pump wavelength dependence of the fluorescence characteristics described in Chapter 4.

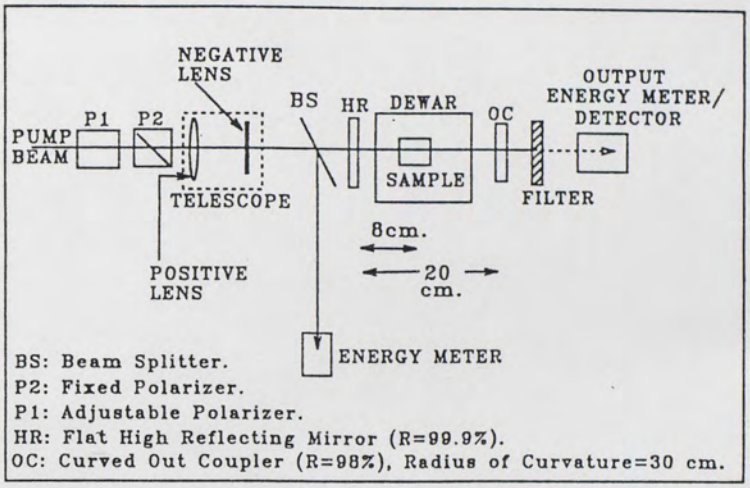

Figure 31. Schematic diagram of the experimental arrangement for the laser experiment.

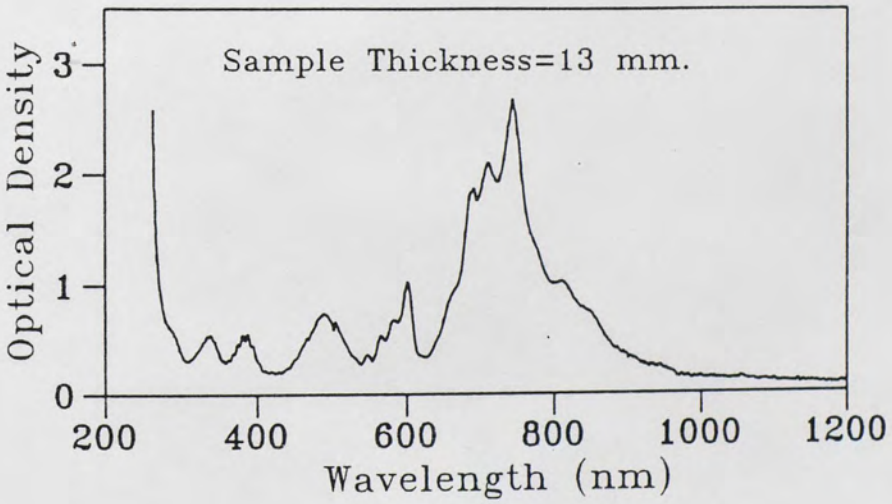

Figure 32. Absorption spectrum of Cr^{4+}:Y_2SiO_5 crystal used for the laser experiment at 77 °K.

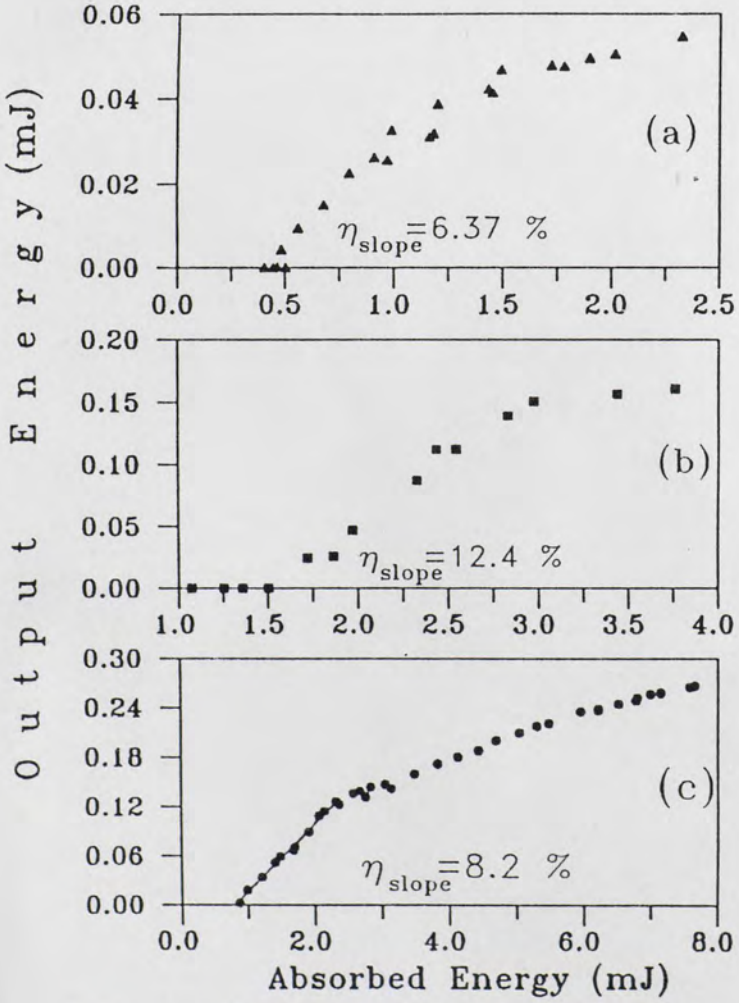

Figure 33. Output-Input curve of Cr:Y_2SiO_5 laser at 77 ^{o}K due to pumping with (a) 1064 nm, (b) 532 nm from a pulsed Nd:YAG laser and (c) broad band @ 840 nm from a pulsed Cr:LiSAF laser.

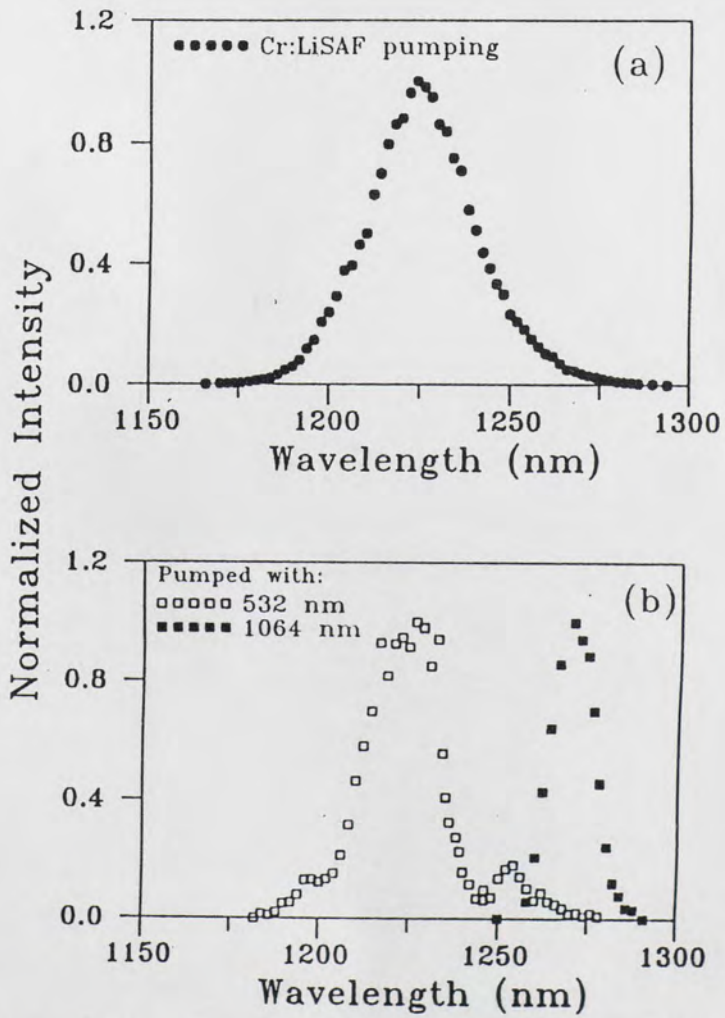

Figure 34. Free running Cr:Y_2SiO_5 laser spectrum due to (a) Cr:LiSAF (@ 840 nm) and (b) Nd:YAG (532 nm and 1064 nm) pumping.

TABLE 6.1

LASER PERFORMANCE CHARACTERISTICS OF THE FREE RUNNING $Cr^{4+}:Y_2SiO_5$ LASER AT 77 ^{o}K

Pump Wavelength (nm)	1064	532	840
Threshold Energy (mJ)	0.32	1.5	0.93
Maximum Slope Efficiency (%)	6.3	12.4	8.2
Peak Laser Wavelength (nm)	1270	1225	1225
Spectral Band-width (nm)	10	23	30

CHAPTER 7

DISCUSSION AND CONCLUSION

Cr^{4+} has been successfully doped in tetrahedral sites in different hosts. It was observed that in the hosts which have both a tetrahedral site for Cr^{4+} and an octahedral site for Cr^{3+} the growth in an oxydizing atmosphere facilitates the inclusion of chromium in the tetravalent state. Laser action in the near infrared was demonstrated for the first time in a purely Cr^{4+} doped crystal, Cr^{4+}:Y_2SiO_5. The present work helped in achieving a better understanding of the mechanisms involved in the near infrared fluorescence of the Cr^{4+} ions in tetrahedral sites. The results of this work provides a new guide for a systematic approach to the problem of crystal field engineering of more efficient Cr^{4+} doped laser crystals.

Chromium in its tetravalent state can efficiently substitute for Si^{4+} in the distorted tetrahedral site in both Y_2SiO_5 and Forsterite in a highly oxidizing growth environment. In both Cr^{4+}:Y_2SiO_5 and Cr:Forsterite the Cr^{4+} site is characterized by strong crystal field parameters which results in the ^3E ($^3T_2$), ^1E mixing. This in turn results in the thermalization of the populations in these two states. In Cr^{4+}:Y_2SiO_5, the sharp line structure in the emission spectrum in the near infrared observed at low temperatures has been attributed to the $^1E - {}^3A_2$ transition. The broad emission band, also in the near infrared, on the other hand, is attributed to the ^3E ($^3T_2$) $- {}^3A_2$ transition. The ^3E ($^3T_2$) states have a stronger electron-phonon coupling than the ^1E and the $^3A_2$ ground state. At higher temperatures non-radiative decays from the ^3E ($^3T_2$) excited states occur primarily by a *fast bottom crossover* [7.1, 7.2, 7.3]

mechanism from the ^3E ($^3T_2$) state to the ground state $^3A_2$ and this is the predominant non-radiative process for depopulating the excited states at these temperatures.

In Forsterite, because of the relatively small electron-phonon coupling of the ^3E ($^3T_2$) state the low temperature luminescence spectrum resulting from the transition from this state to the ground state shows sharp zero phonon line as well as structured phonon side bands. The results of the present work showed that ^3E ($^3T_2$) – $^3A_2$ zero phonon line in Cr:Forsterite is accompanied by the sharp line emission due to the spin-forbidden transition from the ^1E to the $^3A_2$ ground state. However, since the gap between the electronic energies of the ^3E ($^3T_2$) and the ^1E state in this crystal is very very small the two zero phonon lines almost overlap. The *thermal barrier* between the ^1E and the ^3E ($^3T_2$) states is higher in Cr:Forsterite than in Cr^{4+}:Y_2SiO_5 and as a result the sharp structures due to the ^1E – $^3A_2$ transition continue to be observed at a higher temperature in Cr:Forsterite than in Cr^{4+}:Y_2SiO_5.

In both Cr:Forsterite and Cr^{4+}:Y_2SiO_5 there is a clearly observable but small decrease of lifetime even at very low temperatures as the temperature is increased from 10 ^oK to 100 ^oK. It has been shown in this work that this is due to the depopulation of the excited states by the transfer of energy to traps (or 'killer centers') following rapid migration initiated by phonon assisted ion-ion energy transfer processes between the ^1E and the ^3E ($^3T_2$) states of neighboring ions. The assumption of a strong donor-donor energy migration (hopping model) is consistent with the observed short lifetimes (~14 μs for Cr^{4+}:Y_2SiO_5) even at the lowest measured temperature (9.1 ^oK). From the low temperature absorption spectra of Cr^{4+}:Y_2SiO_5 we have seen that the radiative couplings between the ground state and the first excited states are very small. Such small couplings are consistent with the symmetry selection rule that forbids radiative electric-dipole transition between the $^3T_2$ and the $^3A_2$ states in ideal tetrahedral symmetry and the spin selection rule that forbids the ^1E – $^3A_2$ transition. In either case,

at very low temperatures when the thermal de-excitation processes are very small, one would expect a fairly long fluorescence lifetime (at least a few hundred microseconds) instead of the observed value of ~14 μs. This short lifetime is attributed to the presence of rapid donor-donor migration processes. Similar arguments also hold for Cr:Forsterite. It has been seen that such an assumption also results in a consistent interpretation of the temperature dependence of fluorescence lifetime in both Cr^{4+}:Y_2SiO_5 and Cr:Forsterite.

The symmetry of the Cr^{4+} site in Cr^{4+}:Y_2SiO_5 is C_{3V} which is higher than the symmetry of the Cr^{4+} site in Cr:Forsterite which was found to be C_S by Verdun *et. al.*[7.4]. In other words, the $[CrO_4]^{4-}$ tetrahedron is less distorted in Cr^{4+}:Y_2SiO_5 as compared to the tetrahedron in Cr:Forsterite. This would explain the lower fluorescence strength observed for Cr^{4+} ions in Cr^{4+}:Y_2SiO_5 in the NIR as a result of the fact that the transition between $^3T_2$ and $^3A_2$ is symmetry forbidden for electric-dipole transition in ideal tetrahedral symmetry[7.4]. When the site symmetry is lowered this selection rule is over-ruled and the transition is partially allowed, the transition probability increasing as the degree of distortion increases. In this context, it is also interesting to consider the possible role played by the site symmetry and charge compensation in the near infrared luminescence of the Cr^{4+} ion. It is well known that in Cr:Forsterite there are two types of inequivalent Mg^{2+} sites in which Cr^{3+} ions can be located. Cr^{3+} has a considerable size and mass mismatch with Mg^{2+}. As a result when Cr^{3+} substitutes for Mg^{2+} it can put considerable strain on the silicate tetrahedron resulting in distortion. Also Cr^{3+} substituting for Mg^{2+} causes a charge imbalance which is not compensated for by any additional charge compensating dopant. The lattice accommodates such charge imbalance by forming defects in the structure leading to lattice distortion. Since Cr^{4+} fluorescence in Cr:Mg_2SiO_4 is much stronger than in other silicate crystals ($Ca_2Al_2SiO_7$, $Ca_2Ga_2SiO_7$, Y_2SiO_5), none of which has the Cr^{3+}

and charge compensation *'problem'*, it seems that the role played by the so called impure nature of Cr:Mg_2SiO_4 may in fact be a positive one as far as the electric dipole transition rates of the Cr^{4+} ion is concerned. This needs further investigation. In this context it is interesting to note the behavior of the low temperature near infrared spectrum of Cr:Forsterite under different experimental conditions. Time resolved measurements showed that the relative intensity of the sharp line at 1200 nm increases at later times **[Fig. 5(e)]**. This indicates the presence of more than one type of emission within the 1200 nm band. The exact nature of this emission is not known. Also, in the sample grown under pure nitrogen atmosphere when it is pumped by 1064 nm radiation following prolonged exposure to 532 nm laser radiation it shows a spectrum where the sharp line at 1200 nm is almost as intense as the zero phonon line at 1092 nm **[Fig. 4(b)]**. However, under prolonged 1064 nm radiation this effect disappears. This raises the possibility of color center formation by 532 nm radiation which can be annealed by the local heat generated by the 1064 nm radiation[7.5]. These observations need further investigations.

It is also important to be able to introduce impurity elements in the Y^{3+} site in Cr^{4+}:Y_2SiO_5 and test its effect on the Cr^{4+} fluorescence properties. Similar efforts are necessary also in Cr^{4+}:$Ca_2Al_2SiO_7$ and Cr^{4+}:$Ca_2Ga_2SiO_7$. This should provide valuable information for the development of improved Cr^{4+} laser materials.

REFERENCES

Chapter 1

1.1 T.H.Maiman, Nature, 187, (1960), 493.

1.2 J.C.Walling, O.G.Peterson, H.P.Jenssen, R.C.Morris and E.W.O'Dell; IEEE J. Quantum Electronics, **16**, (1980) pp.1302-1315.

1.3 L.L.Chase, S.A.Payne, L.K.Smith, W.L.Kway, H.W.Newkirk, B.H.T.Chai, and M.Long; OSA Proc. on Tunable Solid State Lasers conference**5**,(1989), pp.71-76.

1.4 B.H.T.Chai, M.Stalder and M.Bass; (submitted to Opt. Lett.).

1.5 B.Henderson, NLO, Issue No.4, Autumn 1991 (SERC, U.K.).

1.6 B.Henderson and G.F.Imbusch; *Optical Spectroscopy of Inorganic Solids*, Clarendon, Oxford, 1989.

1.7 V.Petricevic, S.K.Gayen and R.R.Alfano; Appl. Phys. Lett. **53** (26), 1988, pp. 2590-2592.

1.8 G.M.Zverev and A.V.Shestakov; OSA Proc. on Tunable Solid State Lasers conference **5**, (1989), pp. 66-70.

Chapter 2

2.1 S.E.Stokowski, M.H.Randles and R.C.Morris; IEEE J. Quantum Electronics, **24**, (1988), 934.

2.2 V.Petricevic, S.K.Gayen, R.R.Alfano, K. Yamagishi, H. Anzai, Y.Yamaguchi; Appl. Phys. Lett. **53** (13), 1988, pp. 1040-1042.

2.3 J.A.Caird, M.D.Shinn, T.A.Kirchoff, L.K.Smith, R.E.Wilder; Appl. Optics **25**, (1986), 4294.

2.4 J.A.Caird, W.F.Krupke, M.D.Shinn, L.K.Smith, R.E.Wilder; Technical Digest, conference on lasers and electro-optics,1984, Washinton D.C. p.232.

2.5 M.I.Demchuk, E.V.Zharikov, A.M.Zabaznov, I.A.Manichev, V.P.Mikhailov, A.M.Prokhorov, A.P.Shkadarevich, A.F.Chernyakovskii, I.A.Scherbakov, K.V.Yumashev; Sov. J. Quant. Electr. **17**, (1987), 266.

2.6 Reference No. 11 in Ref. 2.8.

2.7 V.Petricevic, S.K.Gayen and R.R.Alfano; Appl. Optics. **27**(20), 1988, pp. 4162-4163.

2.8 V.Petricevic, S.K.Gayen and R.R.Alfano; Appl. Phys. Lett. **53**(26), 1988, pp. 2590-2592.

2.9 H.R.Verdun, L.M.Thomas, D.M.Andrauskas, T.McCollum and A.Pinto; OSA Proc. on Tunable Solid State Lasers conference **5**, (1989), pp. 85-92.

2.10 R.Moncorge, D.J.Simkin, G.Cormier and J.A.Capobianco; OSA Proc. on Tunable Solid State Lasers conference **5**, (1989), pp. 93-97.

2.11 R.Moncorge, G.Cormier, D.J.Simkin and J.A.Capobianco; IEEE J. Quantum Electronics, **27**, No.1 (1991), 114.

2.12 S.Sugano, Y.Tanabe and H.Kamimura; *Multiplets of Transition Metal Ions in Crystals*, Academic Press, New York, 1970.

2.13 W.Jia, L.Lu, B.M.Tissue and W.M.Yen; J. Crystal Growth,**109**, (1991), pp.329-333.

2.14 V.G.Baryshevski, M.V.Korzhik, M.G.Livshitz, A.A.Tarasov, A.E.Kimaev, I.I.Mishkel, M.L.Meilman, B.J.Minkov and A.P.Shkadarevich; OSA Proc. on Advanced Solid State Lasers conference **10**, (1991), pp. 26-34.

2.15 A.Sugimoto, Y.Segawa, Y.Yamaguchi, Y.Nobe, K.Yamagishi, P.H.Kim and S.Namba; Japanese J. Appl. Phys. **28**(10), 1989, pp.L1833-L1835.

2.16 Y.Segawa and A.Sugimoto; OSA Proc. on Advanced Solid State Lasers conference **10**, (1991), pp. 49-51.

2.17 V.Petricevic, S.K.Gayen and R.R.Alfano; OSA Proc. on Tunable Solid State Lasers conference **5**, (1989), pp. 77-84.

2.18 V.Petricevic, A.Seas and R.R.Alfano; OSA Proc. on Advanced Solid State Lasers conference **10**, (1991), pp. 41-43.

2.19 A.Seas, V.Petricevic and R.R.Alfano; OSA Proc. on Advanced Solid State Lasers conference **10**, (1991), pp. 69-71.

2.20 T.J.Carrig, A.Sennaroglu and C.R.Pollock; Advanced Solid State Lasers Technical Digest, Santa Fe,1992, Paper No. MB4-1, pp. 21-22.

2.21 G.M.Zverev and A.V.Shestakov;
OSA Proc. on Tunable Solid State Lasers conference **5**, (1989), pp. 66-70.

2.22 W.Jia, B.M.Tissue, L.Lu, K.R.Hoffman and W.M.Yen;
OSA Proc. on Advanced Solid State Lasers conference **10**, (1991), pp. 87-91.

2.23 T.H.Allik, B.H.T.Chai and L.D.Merkle;
OSA Proc. on Advanced Solid State Lasers conference **10**, (1991), pp. 84-86.

2.24 M.H.Garrett, V.H.Chan, H.P.Jenssen, M.H.Whitmore, A.Sacra, D.J.Singel and D.J.Simkin. OSA Proc. on Advanced Solid State Lasers conference, **10**, (1991), pp. 49-51.

Chapter 3

3.1 S. H. Hirnak, M.Sc. Thesis (1992), Univ. of Central Florida.

3.2 Y. Shimony, Project Report(1991), Crystal Growth Lab., Center for Electro Optics and Lasers, University of central Florida.

3.4 T.H.Allik, B.H.T.Chai and L.D.Merkle;
OSA Proc. on Advanced Solid State Lasers conference **10**, (1991), pp. 84-86.

3.5 M.Kimata and N.Li;
N. Jb. Miner. Abh., **144**(3), 1982, pp.254-267.

3.6 A.A.Kaminskii, E.L.Belokoneva, B.V.Mill, S.E.Sarkisov and K.Kurbanov;
Phys. Status Solidi **A 97**, (1986) pp. 279-290.

3.7 H.R.Verdun, L.M.Thomas, D.M.Andrauskas, T.McCollum and A.Pinto;
OSA Proc. on Tunable Solid State Lasers conference **5**, (1989), pp. 85-92.

3.8 W.Jia, B.M.Tissue, L.Lu, K.R.Hoffman and W.M.Yen;
OSA Proc. on Advanced Solid State Lasers conference **10**, (1991), pp. 87-91.

Chapter 4

4.1 S.Sugano, Y.Tanabe and H.Kamimura;
Multiplets of Transition Metal Ions in Crystals, Academic Press, New York, 1970.

4.2 J. Breguet, A.F.Umsykov, W.A.R.Luthy, I.A.Scherbakov, H.P.Weber; IEEE J. Quantum Electronics, **27**, No.2 (1991).

4.3 T.Herbert, W.P.Risk, R.M.Macfarlane, W.Lenth; OSA Proc. on Advanced Solid State Lasers conference **10**, (1991), pp. 379-384.

4.4 A.B.P.Lever; *Inorganic Electronic Spectroscopy*, Elsevier, Amsterdam, 1968.

4.5 L.H.Hall; *Group theory and symmetry in chemistry*, McGraw-Hill, New York, 1969.

4.6 J.S.Griffith; *The theory of transition metal ions*, Cambridge University Press, Cambridge, 1964.

4.7 B.Henderson and G.F.Imbusch; *Optical Spectroscopy of Inorganic Solids*, Clarendon, Oxford, 1989.

4.8 Y.Tanabe and S.Sugano; J. Phys. Soc. Japan **9**, (1954) 753.

4.9 B.Henderson, NLO, Issue No.4, Autumn 1991 (SERC, U.K.).

4.10 M.Born and J.R.Oppenheimer; Ann. Phys. **84**, (1927) p.457.

4.11 T.H.Keil, Phys. Rev. **140**, (1965), A601.

4.12 N.F.Mott; Proc. Roy. Soc. **A 167**, (1938), 384.

4.13 N.F.Mott and R.W.Gurney; *Electronic Processes in Ionic Crystals*, Dover Publications, 1964.

4.14 A. von Hippel, Z. Phys. **101**, (1936), 680.

4.15 F. Seitz, J. Chem. Phys. **6**, (1938), 150.

4.16 F.E.Williams, Phys. Rev. **80**, (1950), 306.; J.Chem. Phys. **19**, (1951),457; and Phys. Rev. **82** (1951), 281.

4.17 F.E.Williams and M.H.Hebb, Phys. Rev. **84**, (1951),1181.

4.18 M.Stalder, M.Bass and B.H.T.Chai (to be published).

4.19 A.Kiel; *Proc. Third Int. Conf. Quant. Elect*, Paris, 1963, Columbia Univ. Press, N.Y., 1964 (P.Grivet and N.Bloembergen, ed.).

4.20 H.W.Moos, J.Luminescence **1,2**, (1970), pp. 106-121.

4.21 C.W.Struck and W.H.Fonger, J.Luminescence **10** (1970), pp. 1-30.

4.22 E.W.Condon, Phys. Rev. **32**, (1928), 858.

4.23 C.Manneback, Physica **17**, (1951), 1001.

4.24 T.Forster, Ann. Phys. (Leipzig) **2**, (1948), 55.

4.25 D.L.Dexter, J.Chem. Phys. **21**, (1953), 836.

4.26 T.Forster, Z.Naturforsch **4A**, (1949), 321.

4.27 D.L.Huber, Phys. Rev. **B20**, (1979), 2307.

4.28 R.K.Watts in *Optical properties of ions in solids*,
(B. DiBartolo ed.),Plenum Press, New York, 1975.

4.29 M.Inokuti and H.Hirayama, J.Chem. Phys. **43**, (1965), 1978.

4.30 M.Yokota and O.Tanimoto, J.Phys. Soc. Japan, **22**, (1967), 779.

4.31 A.I.Burshtein, J.Luminescence **34**, (1985), 167.

4.32 A.I.Burshtein, Soviet Physics JETP **31**, (1972), 882.

Chapter 5

5.1 S.Sugano, Y.Tanabe and H.Kamimura;
Multiplets of Transition Metal Ions in Crystals, Academic Press, New York, 1970.

5.2 A.B.P.Lever; *Inorganic Electronic Spectroscopy*, Elsevier, Amsterdam, 1968.

5.3 H.R.Verdun, L.M.Thomas, D.M.Andrauskas, T.McCollum and A.Pinto;
OSA Proc. on Tunable Solid State Lasers conference **5**, (1989), pp. 85-92.

5.4 B.Henderson and G.F.Imbusch;
Optical Spectroscopy of Inorganic Solids, Clarendon, Oxford, 1989.

5.5 T.H.Keil, Phys. Rev. **140A**, (1965), 601.

5.6 J.F.Donegan, F.J.Bergin, T.J.Glynn, G.F.Imbusch and J.P.Remeika;
J. Luminescence, **35**, (1986), pp.57-63.

5.7 T.Forster, Ann. Phys. (Leipzig) **2**, (1948), 55.

5.8 D.L.Dexter, J.Chem. Phys. **21**, (1953), 836.

5.9 T.Forster, Z.Naturforsch **4A**, (1949), 321.

5.10 D.L.Huber, Phys. Rev. **B20**, (1979), 2307.

5.11 R.K.Watts in *Optical properties of ions in solids*, p.321,
(B. DiBartolo ed.), Plenum Press, New York, 1975.

5.12 P.Lacovara; OSA Proc. on Advanced Solid State Lasers conference,
13, (1992), pp.296-299.

5.13 Yu.K.Voron'ko, T.G.Mamedov, V.V.Osiko, M.I.Timoshechkin, I.A.Shcherbakov;
Soviet Phys. JETP, **38**, (1974), 565.

5.14 N.F.Mott and R.W.Gurney;
Electronic Processes in Ionic Crystals, Dover Publications, 1964.

5.15 N.F.Mott; Proc. Roy. Soc. **A 167**, (1938), 384.

5.16 H.W.Moos, J.Luminescence **1,2**, (1970), pp. 106-121.

5.17 C.J.Donnelly, T.J.Glynn, G.P.Morgan and G.F.Imbusch;
J.Luminescence, **48 & 49**, (1991), pp.283-287.

5.18 S.M.Jacobsen, H.U.Gudel and C.A.Daul; J. Am. Chem. Soc. **110**, (1988), 7610.

5.19 G. Blasse in *Radiationless Processes*, p.291,
(B. DiBartolo ed.), Plenum Press, New York, 1980.

5.20 C.Deka, M.Bass, B.H.T.Chai and X.X.Zhang;
OSA Proc. on Advanced Solid State Lasers conference,**13**, (1992), pp.48-51.

5.21 M.V.Iverson and W.A.Sibley; J.Luminescence, **20**, (1979), 311.

5.22 R.Moncorge, G.Cormier, D.J.Simkin and J.A.Capobianco;
IEEE J. Quantum Electronics, **27**, No.1 (1991), 114.

5.23 W.Jia, L.Lu, B.M.Tissue and W.M.Yen; J. Crystal Growth,**109**, (1991),
pp.329-333.

5.24 V.G.Baryshevski, M.V.Korzhik, M.G.Livshitz, A.A.Tarasov, A.E.Kimaev,
I.I.Mishkel, M.L.Meilman, B.J.Minkov and A.P.Shkadarevich;
OSA Proc. on Advanced Solid State Lasers conference **10**, (1991), pp. 26-34.

5.25 V.Petricevic, S.K.Gayen and R.R.Alfano;
OSA Proc. on Tunable Solid State Lasers conference **5**, (1989), pp. 77-84.

5..26 T.H.Allik, B.H.T.Chai and L.D.Merkle;
OSA Proc. on Advanced Solid State Lasers conference **10**, (1991), pp. 84-86.

Chapter 7

7.1 N.F.Mott; Proc. Roy. Soc. **A 167**, (1938), 384.

7.2 N.F.Mott and R.W.Gurney;
Electronic Processes in Ionic Crystals, Dover Publications, 1964.

7.3 C.W.Struck and W.H.Fonger, J.Luminescence **10** (1970), pp. 1-30.

7.4 H.R.Verdun, L.M.Thomas, D.M.Andrauskas, T.McCollum and A.Pinto;
OSA Proc. on Tunable Solid State Lasers conference **5**, (1989), pp. 85-92.

7.5 C.Deka, M.Bass, B.H.T.Chai and X.X.Zhang;
OSA Proc. on Advanced Solid State Lasers conference **13**, (1992), pp. 48-51.